Fall 2014

Large-eddy simulation of sub-, critical and super-critical Reynolds number flow past a circular cylinder

Seong Mo Yeon
University of Iowa

LARGE-EDDY SIMULATION OF SUB-, CRITICAL AND SUPER-CRITICAL REYNOLDS NUMBER FLOW PAST A CIRCULAR CYLINDER

by

Seong Mo Yeon

A thesis submitted in partial fulfillment
of the requirements for the Doctor of
Philosophy degree in Mechanical Engineering
in the Graduate College of
The University of Iowa

December 2014

Thesis Supervisors: Professor Frederick Stern
Adjunct Professor Jianming Yang

Graduate College
The University of Iowa
Iowa City, Iowa

CERTIFICATE OF APPROVAL

PH.D. THESIS

This is to certify that the Ph.D. thesis of

Seong Mo Yeon

has been approved by the Examining Committee
for the thesis requirement for the Doctor of Philosophy
degree in Mechanical Engineering at the December 2014 graduation.

Thesis Committee: _____
Frederick Stern, Thesis Supervisor

_____
Jianming Yang, Thesis Supervisor

_____
Pablo M. Carrica

_____
Albert Ratner

_____
Larry J. Weber

To my beloved wife and two children, Eunmi Kim, Suhan J. Yeon and oncoming baby

ACKNOWLEDGMENTS

I would like to express the deepest appreciation to my advisor, Professor Frederick Stern, who had supported me throughout my thesis with his patience and knowledge. I would also like to give my thanks to my co-advisor, Dr. Jianming Yang. This thesis would not have been possible without their guidance, support, and constructive discussions. I would also like to convey my sincere gratitude to my advisory committee members, Professors Albert Ratner, Pablo Carrica and Larry Weber.

I would like to express my appreciation to Professor Key-pyo Rhee in Seoul National University who guided me to study for Ph.D. I am grateful to my Korean colleagues in IIHR, especially, Dr. Hyunse Yoon, Dr.Sung-hwan Yoon, and Dong-Hwan Kim for the great time we shared together in Iowa.

I am indebted to my parents, my parents-in-law and my sister for their love, support, and encouragement. I would like to express my special love and gratitude to my wife, Eunmi, my two children, Jade (Suhan) and a baby on the way due on coming March, who accepted my absences from home-life, but also supported and motivated through the hard times.

This work is sponsored by the US Office of Naval Research through research grant N000141-01-00-1-7 under the administration of Dr. Ki-Han Kim. The numerical simulations were performed using DoD HPC resources.

ABSTRACT

Large-eddy simulations of turbulent flows past a circular cylinder have been performed at sub-, critical and super-critical Re using an orthogonal curvilinear grid solver, CFDship-Iowa version 6.2. An extensive verification and validation study has been carried out. Various aspects of the flow field have been investigated.

The aspect ratio of the computational domain has major effects on the results. In general, large aspect ratio produced best results for the sub-critical Re. Small dependency on both aspect ratio and grid resolution was observed for the critical Re. Small aspect ratio and conservative scheme produced best results for the super-critical Re.

Overall flow features and the drag crisis phenomenon have been correctly predicted. A lot of experimental and numerical studies of flow past a circular cylinder were collected and used for the validation of the present LES study. Integral and local variables were in fairly good agreement for the sub-critical Re. Sharp behavior including drag crisis was predicted for the critical Re. Although some discrepancy including early formation of turbulent separation was observed, local flow structures including separation bubble were observed for the super-critical Re.

The formation of secondary vortex near the cylinder wall and its evolution into separation bubble were observed. The spectral analysis showed that the separation bubble had the instabilities close to the shear layer frequency. The proximity of shear layer to the cylinder enhanced the mixing process of boundary layer and shear layer and led to the formation of separation bubble. A snapshot POD method was used to extract flow structures in the boundary layer, shear layer and wake. In the boundary layer, the secondary vortices and separation bubble were successfully extracted. Due to the weak TKE distribution, specific flow structures were hard to find in the shear layer. Large two-dimensional flow structures representing the Karman shedding vortices were extracted for the sub- and super-critical Re.

PUBLIC ABSTRACT

Large-eddy simulations of turbulent flows past a circular cylinder have been performed at sub-, critical and super-critical Re using an orthogonal curvilinear grid solver, CFDship-Iowa version 6.2. An extensive verification and validation study has been carried out. Various aspects of the flow field have been investigated.

The aspect ratio of the computational domain has major effects on the results. In general, large aspect ratio produced best results for the sub-critical Re. Small dependency on both aspect ratio and grid resolution was observed for the critical Re. Small aspect ratio and conservative scheme produced best results for the super-critical Re.

Overall flow features and the drag crisis phenomenon have been correctly predicted. A lot of experimental and numerical studies of flow past a circular cylinder were collected and used for the validation of the present LES study. Integral and local variables were in fairly good agreement for the sub-critical Re. Sharp behavior including significant drag reduction was predicted for the critical Re. Although some discrepancy including early formation of turbulent separation was observed, local flow structures including separation bubble were observed for the super-critical Re.

The formation of secondary vortex near the body and its evolution into separation bubble were observed. The proximity of shear layer to the cylinder enhanced the mixing process of boundary layer and shear layer and led to the formation of separation bubble. A snapshot POD method was used to extract flow structures in the boundary layer, shear layer and wake.

TABLE OF CONTENTS

LIST OF TABLES viii

LIST OF FIGURES x

CHAPTER 1 INTRODUCTION 1
1.1 Background and Motivation 1
1.2 Objectives and Approach 13
1.3 References 13

CHAPTER 2 COMPUTATIONAL METHODS 34
2.1 Mathematical Model 34
2.1.1 Navier-Stokes equations 34
2.1.2 LES Turbulence model 34
2.2 Numerical Methods 35
2.2.1 Navier-Stokes solver 35
2.2.2 Fractional step method 37
2.2.3 Spatial discretization 38
2.2.4 Direct Poisson equation solver 40
2.2.5 LES model implementation 42
2.3 Software Architecture and High Performance Computing 44
2.4 Computational Setup 45
2.5 Analysis Methods 46
2.5.1 Verification and validation 46
2.5.2 Quality assessment criteria for LES 48
2.5.3 Cross correlation coefficient and correlation length 48
2.5.4 Energy spectra, grid cutoff and Kolmogorov scale 49
2.5.5 Shear layer instability analysis 50
2.5.6 Turbulence intensity 51
2.5.7 TKE budget equation 52
2.5.8 Proper Orthogonal Decomposition analysis 53
2.6 References 54

CHAPTER 3 QUANTITATIVE VERIFICATION AND VALIDATION AND SENSITIVITY STUDIES 61
3.1 Statistical Convergence 61
3.2 Quantitative Verification and Validation 61
3.3 Effect of Aspect Ratio, Grid resolution and Convection Scheme 62
3.4 Conclusions 64
3.5 References 66

CHAPTER 4 VALIDATION 74
4.1 Assessment of LES Quality 74
4.2 Energy spectra and dissipation 77
4.3 Validation of LES 78
4.4 Conclusions 83
4.5 References 87

CHAPTER 5 ADDITIONAL DIAGNOSTICS 114
5.1 Basic flow features 114
5.2 Reynolds Stresses and TKE in Wake 114
5.3 Instantaneous flow features 115

5.4 Instabilities in Separation Bubbles 116
5.5 Flow Structure Analysis with POD Method 117
5.6 Conclusions 120
5.7 References 122

CHAPTER 6 CONCLUSIONS AND FUTURE RESEARCH 138

LIST OF TABLES

Table 1.1 Summary of experimental studies and validation variables 18

Table 1.2 Summary of numerical studies and validation variables 19

Table 1.3 Key point angles (Achenbach, 1968).....20

Table 1.4 Key point angles (Pfeil and Orth, 1990).....20

Table 1.5 Effective shear layer length Ls and recirculation length Lr.....20

Table 1.6 Key point angles for hybrid methods.....20

Table 1.7 Key point angles for LES.....21

Table 2.1 Test cases 57

Table 3.1 Summary of simulations performed for verification and validation for super-critical Re ($Re=7.57x10^5$) 67

Table 3.2 Sensitivity study for sub-critical Re ($Re=6.31x10^4$) and computed integral parameters with $\Lambda/D=3.3$ 68

Table 3.3 Sensitivity study for sub-critical Re ($Re=1.26x10^5$) and computed integral parameters with $\Lambda/D=2.9$ 69

Table 3.4 Sensitivity study for critical Re ($Re=2.52x10^5$) and computed integral parameters with $\Lambda/D=0.8$.....70

Table 3.5 Sensitivity study for super-critical Re ($Re=7.57x10^5$) and computed integral parameters with $\Lambda/D=1.3$ 71

Table 4.1 Summary of mean IQ and range of boundary layer, shear layer and wake.....88

Table 4.2 Convergence ratio to 120 cycles of TKE budgets for $Re=7.57x10^5$.....88

Table 4.3 Spatial average of TKE budgets for $Re=7.57x10^5$.....88

Table 4.4 Cell size in streamwise direction of the grid points and grid cutoff estimation of shear layer.....89

Table 4.5 Cell size in streamwise direction of the grid points and grid cutoff estimation of wake centerline 89

Table 4.6 Estimation of Kolmogorov scale of shear layer.....89

Table 4.7 Estimation of Kolmogorov scale of wake centerline.....90

Table 4.8 Summary of integral and local variables with experimental data.....90

Table 4.9 Errors of integral and local variables.....90

Table 4.10 Mean errors of local variables 91

Table 4.11 Comparison of keypoints and thickness of separation bubble.....91

Table 4.12 Key points of the present LES study 91

Table 4.13 Errors for key points of the present LES study.....92

Table 4.14 Mean errors of Reynolds stresses for sub-critical Re 92

Table 4.15 Effective shear layer length Ls and recirculation length Lr.....92

Table 4.16 Error of effective shear layer length Ls and recirculation length Lr 92

Table 4.17 Estimation of frequency of shear layer vortices 93

Table 4.18 Summary of comparison errors.....93

Table 5.1 Measuring points (circumferential and radial direction) across the separation bubble for FFT analysis.....123

Table 5.2 Karman vortex shedding frequency from POD results.....123

LIST OF FIGURES

Figure 1.1 Drag, separation angle and base pressure vs. Re (EFD).....22

Figure 1.2 RMS lift coefficient and Strouhal number vs. Re (EFD) 22

Figure 1.3 Pressure (left) and skin-friction (right) (EFD); orange=MP, red=LS, magenta=TT, blue=TR, purple=TS and green=BP. Solid black symbols overlaid on the skin-friction are angular pressure gradient. 23

Figure 1.4 Pressure (up) and skin-friction (bottom) (EFD); orange=MP, red=LS, blue=TR, purple=TS and green=BP. The TR is corresponding to the end of the laminar separation bubble. 24

Figure 1.5 MP, LS, LR, TS and BP points on the cylinder (EFD); ●=MP, ▲=LS, ▼=TR, ▶=TS and ◆=BP. 25

Figure 1.6 Mean velocity (top) and turbulence intensity (bottom) for $Re=6x10^5$ (Pfeil and Orth, 1990) 26

Figure 1.7 Definition of (a) L_s and (b) L_r.....26

Figure 1.8 Reynolds stresses for sub-critical Re($Re=1.4x10^5$) (EFD).....27

Figure 1.9 Correlation coefficient (a) and correlation length (b) (EFD) 27

Figure 1.10 Normalized shear layer frequency (EFD).....27

Figure 1.11 Drag, separation angle and base pressure vs. Re (URANS).....28

Figure 1.12 RMS lift coefficient and Strouhal number vs. Re (URANS) 28

Figure 1.13 Drag, separation angle and base pressure vs. Re (Hybrid).....29

Figure 1.14 RMS lift coefficient and Strouhal number vs. Re (Hybrid) 29

Figure 1.15 Pressure (left) and skin-friction (right) (Hybrid); orange=MP, red=LS, blue=TR, purple=TS and green=BP. Solid red line overlaid on the skin-friction are angular pressure gradient. 30

Figure 1.16 MP, LS, TR, TS and BP points on the cylinder (Hybrid); ●=MP, ▲=LS, ▼=TR, ▶=TS and ◆=BP. 31

Figure 1.17 Drag, separation angle and base pressure vs. Re (LES) 32

Figure 1.18 RMS lift coefficient and Strouhal number vs. Re (LES).....32

Figure 1.19 Pressure (left) and skin-friction (right) (LES); orange=MP, red=LS, blue=TR, purple=TS and green=BP. Solid red line overlaid on the skin-friction are angular pressure gradient. 33

Figure 1.20 MP, LS, TR, TS and BP points on the cylinder (LES); ●=MP, ▲=LS, ▼=TR, ▶=TS and ◆=BP. 33

Figure 2.1. Coordinate systems and boundary conditions; (a) X-Y plane and (b) X-Z plane 58

Figure 2.2 Domain size (a) and body-fitted grid around a cylinder (b) 59

Figure 2.3 Energy spectrum for streamwise velocity of a circular cycliner: (a) grid cutoff and numerical dissipation (Mittal and Moin, 1997) (b) largest scales of turbulent flow obtained from FFT analysis (c) energy spectrum with grid cutoff and Kolmogorov scale 60

Figure 3.1 Time history of drag and lift coefficients 72

Figure 3.2 FFT analysis of 20 cycles of drag and lift coefficients 73

Figure 4.1 IQ distribution with averaging regions; half region is indicated for the wake. 94

Figure 4.2 Balance of momentum equations at $Re=1.26x10^5$ 95

Figure 4.3 Averaged TKE budgets: (a) contour of residual with test region and (b) variation with cycles for super-critical Re ($Re=7.57x10^5$) 96

Figure 4.4 Ratio of residual to : (a) convection, (b) production, (c) pressure transport, (d) turbulent transport, (e) viscous diffusion, (f) viscous dissipation and (g) SGS transport 96

Figure 4.5 TKE budget at $Re=1.26x10^5$ with 10 cycles 97

Figure 4.6 TKE budget at $Re=2.52x10^5$ with 10 cycles 98

Figure 4.7 TKE budget at $Re=7.57x10^5$ with 120 cycles 99

Figure 4.8 TKE budget distribution before LS 100

Figure 4.9 TKE budget distribution across shear layer for sub-, and critical Re 100

Figure 4.10 TKE budget distribution at key points for $Re=7.57x10^5$ 100

Figure 4.11 Energy spectra in the shear layer near the body (left) and 3D away from the cylinder center of the wake centerline (right) 101

Figure 4.12 Drag, separation angle and base pressure vs. Re 102

Figure 4.13 RMS lift coefficient and Strouhal number vs. Re 102

Figure 4.14 Pressure (left) and skin-friction with pressure gradient in red (right); orange=MP, red=LS, blue=TR, purple=TS and green=BP. The TR is corresponding to the end of the laminar separation bubble. 103

Figure 4.15 Mean velocity (top) and turbulence intensity (bottom) for $Re=7.57x10^5$ 104

Figure 4.16 Turbulent intensity contour with stream line near separated flow 105

Figure 4.17 Present LES results of MP, LS, TR, TS and BP points on the cylinder; ●=MP, ▲=LS, ◀=TT, ▼=TR, ▶=TS and ◆=BP. 106

Figure 4.18 Mean streamline (left) and instantaneous streamline (right); ●=MP, ▲ =LS, ◀=TT, ▼=TR, ▶=TS and ◆=BP. 107

Figure 4.19 Mean streamline for critical (left) and super-critical (right) Re with key points.....108

Figure 4.20 Variation of Reynolds stresses with Re.....109

Figure 4.21 Comparison of correlation coefficient (a) and correlation length (b).....110

Figure 4.22 Mean velocity vector (left) and secondary vorticity contour (right). FFT analysis for shear layer and boundary layer is done at X mark 111

Figure 4.23 FFT analysis of streamwise velocity in shear layer.....112

Figure 4.24 Normalized shear layer frequency.....113

Figure 5.1 Mean flow features: sub-critical ($Re=1.26x10^5$) (left), critical ($Re=2.52x10^5$) (middle) and super-critical ($Re=7.57x10^5$) (right) 124

Figure 5.2 Reynolds stresses and resolved turbulent kinetic energy: sub-critical ($Re=1.26x10^5$) (left), critical ($Re=2.52x10^5$) (middle) and super-critical ($Re=7.57x10^5$) (right) 125

Figure 5.3 Instantaneous flow features: sub-critical ($Re=1.26x10^5$) (left), critical ($Re=2.52x10^5$) (middle) and super-critical ($Re=7.57x10^5$) (right) 126

Figure 5.4 Vortex structure with Q-criterion: (a) sub-critical ($Re=6.31x10^4$) (b) sub-critical ($Re=1.26x10^5$), (c) critical ($Re=2.52x10^5$) (d) super-critical ($Re=4.15x10^5$), (e) super-critical ($Re=5.06x10^5$) and (f) super-critical ($Re=7.57x10^5$).....127

Figure 5.5 Instantaneous velocity vector (top) and secondary vorticity with streamlines (middle) with the region for FFT analysis (bottom).....128

Figure 5.6 Enlarged secondary vorticity with mean center of shear layer.....128

Figure 5.7 Energy spectra near separation bubble: (a) critical Re ($Re=2.52x10^5$) and (b) super-critical Re ($7.57x10^5$) 129

Figure 5.8 Analysis region of POD in flow field.....130

Figure 5.9 Relative kinetic energy distribution in POD regions up to first 10 modes: (a) boundary layer, (b) shear layer and (c) wake 131

Figure 5.10 Streamlines in boundary layer at midspan.....132

Figure 5.11 Spanwise vortex structure with Q-criterion in boundary layer 133

Figure 5.12 Streamlines in shear layer at midspan 134
Figure 5.13 Spanwise vortex structure with Q-criterion in shear layer 135
Figure 5.14 Streamlines in wake at midspan 136
Figure 5.15 Spanwise vortex structure with Q-criterion in wake 137

CHAPTER 1

INTRODUCTION

1.1 Background and Motivation

Physics and simulation capability of 3D unsteady separation remains a significant challenge for many fields, including marine and ocean engineering. Ships and offshore structures suffer separations due to bluff bodies, sharp edges, appendages, wave-induced, and off-design conditions. A fundamental geometry for both applications is cylinder flow studied for many years focusing on Reynolds number (Re) effects on smooth surface separation and wake.

Present interest is in application of high fidelity LES of single-phase cylinder flow for sub- to super-critical Re for verification & validation, as well as analysis of physics in preparation for two-phase simulations and experiments. The research was conducted in parallel and the results were submitted to the ITTC OEC Workshop on VIV and Wave Run-up held in Nantes, France October 17-18, 2013. Additional motivation was to resolve issues in previous CFDShip-Iowa V6.2 two-phase surface-piercing cylinder simulation for critical and super-critical Re for which the deep flow did not display the correct single-phase behavior (Koo et al., 2014).

Williamson (1996), Sumer (2006), and Schewe (1983) define flow regimes: sub-critical $3x10^2<Re<2x10^5$, critical $2x10^5<Re<3.5x10^5$, super-critical $3.5x10^5<Re<1.5x10^6$, and post-critical $Re>1.5x10^6$. Experimental benchmark validation data and previous URANS, hybrid and LES studies provide assessment of the status of information. References are provided in figure keys and Tables 1.1 and 1.2. Laminar/turbulent separation, laminar separation bubble, turbulent transition, shear layer and Karman instabilities govern the nature of the flow separation for different flow regimes. Experimental benchmark validation data is available for mostly global/integral and limited local flow variables.

Fig. 1.1 (a), (b) and (c) show drag coefficient C_D, separation angle θ_s, and base pressure – C_{pb} against Re, respectively. The drag coefficient shows clear trends albeit with fairly large

scatter between the facilities due to many factors including aspect ratio (AR), free stream turbulence, roughness, blockage, etc. The drag coefficient is nearly constant for the sub-critical Re $C_D \approx 1.2$, drops dramatically (drag crisis) by a factor of 4 to $C_D \approx 0.28$ for the critical Re, nearly constant at this value for the super-critical Re, and increases by a factor of 2.5 up to $C_D \approx 0.7$ for the post-critical Re. The separation angle moves from $\theta_s \approx 75$ to 90 deg for the sub-critical Re, increases dramatically up to $\theta_s \approx 140$ deg for the critical Re, nearly constant at this value for the super-critical Re, and decreases to $\theta_s \approx 125$ deg for the super-critical Re. The base pressure trends closely follow the drag trends. Fig. 1.2 (a), (b), (c) show the mean side force (lift coefficient) C_L, RMS lift C_L^{RMS}, and Strouhal number St against Re, respectively. The mean lift is mostly zero except for border of critical- and super-critical Re where some experiments show large $C_L \approx 1.25$ due to asymmetric laminar separation bubble condition. The RMS lift is large $C_L^{RMS} \approx 0.4$ for the sub-critical Re, drops dramatically by a factor of 10 to $C_L^{RMS} \approx 0.04$ for the critical Re, nearly constant at this value for the super-critical Re, and increases by factor of 2 to $C_L^{RMS} \approx 0.08$ for the post-critical Re. The differences between RMS lift between facilities for the sub-critical Re is due to differences between use of load cell (lower values) and pressure-integration (higher values) measurement systems. The St is nearly constant St ≈ 0.2 for the sub-critical Re, increases dramatically to St ≈ 0.475 for the critical Re, drops to St ≈ 0.425 for the super-critical Re, and dramatically drops to St ≈ 0.1 for initial post-critical Re and increases up to St ≈ 0.3 for Re up to nearly 10^7. The boundary layer transition from laminar to turbulent flow delays separation, which narrows the wake and reduces the drag. The narrower the wakes the smaller the RMS lift, but the larger the St.

Table 1.3 and 1.4 show key points and values for minimum pressure (MP), laminar separation (LS), turbulent transition (TT), turbulent reattachment (TR), turbulent separation (TS) and base pressure (BP) positions. The key point positions and values in Table 1.3 are determined from the local flow pressure and shear stress distributions by Achenbach (1968). The positions and values in Table 1.4 are determined from the data by Pfeil and Orth (1990). MP is upstream of LS for the sub- and critical Re, at LS and upstream of TR and TS for the super-critical Re,

and upstream of TS for the post-critical Re. LS is where the shear stress changes from positive to negative. TT is determined by large rates of turbulence intensity, which occurs near the separation bubble boundary at its maximum thickness. TR is followed by TT for the super-critical Re and forms laminar separation bubble along with LS. TR is estimated where the pressure kink ends. TS is estimated where the shear stress changes from positive to negative or where it becomes constant after LS. BP is at 180 deg from stagnation point.

Fig. 1.3 shows the pressure and shear stress distributions for the sub- to the post-critical regimes with key points marked. Overlaid on the shear stress distributions is the angular pressure gradient $dp/d\theta$ determined from numerical differentiation of the pressure distributions. The differences between facilities are due to Re values and regimes transition differences. These differences are relatively small for the sub-critical Re compared with the critical, super- and post-critical Re. The shear stress directly correlates with $dp/d\theta$. On the forebody, the C_f local maximum occurs just after the $dp/d\theta$ local minimum. On the shoulder (sub-critical Re) and afterbody (critical, super- and post-critical Re), the maximum of $dp/d\theta$ matches with the point where the shear stress changes from positive to negative for the sub-, critical and post-critical Re. The maxima of $dp/d\theta$ are observed near a kink referred to as the separation bubble that are approximately corresponding to the points where the shear stress becomes zero for the critical and super-critical Re. One of the maxima is corresponding to TR where the shear stress is locally maximum. The acceleration/deceleration ($dp/d\theta$) and TT governs the flow pressure and shear stress distributions. The critical and super-critical Re indicated laminar separation bubbles for some Re/facilities; the separation bubble can be observed between at 100 deg (LS) and 114 deg (TR) as shown in Fig. 1.3. The TT was observed at around 110 deg followed by the TR and the transition occurred in the separation bubble (Pfeil and Orth, 1990). Fig. 1.4 (a) and (b) show the pressure and shear stress distributions for one facility covering all Re regimes. Fig. 1.5 graphically displays the key points for the Fig. 1.4 distributions where BP are the pressure at θ_s = 180 deg. The distance of LS is downstream from MP and increases from 5 to 9 to 20 deg for the sub- to increasing critical Re. For the super–critical Re, LS coincides with MP followed by TR

10 deg later and TS 28 deg after that for Achenbach (1968). LS is followed by TT 10 deg later and TR 4 deg after that for Pfeil and Orth (1990). Lastly, TS is 31 deg downstream of MP for the post-critical Re.

The laminar separation bubble was observed in the study of drag reduction in a wide range of Re and showed strong correlation to the drag crisis. Bearman (1969) and Schewe (1983) studied drag reduction for critical Re and observed two discontinuous transition in drag and St as shown in Fig. 1.1 (a) and 1.2 (c). At the first transition, the drag exhibited moderate decrease followed by sharp reduction where large mean lift coefficient (≈1) was observed due to the asymmetric formation of the laminar separation bubble as shown in Fig. 1.2 (a). At the second transition, the drag reached the minimum and mean lift coefficient was almost zero due to the symmetric formation of the laminar separation bubble. Achenbach (1968) studied drag reduction along with pressure and skin-friction distribution in a wide range of Re (up to post-critical Re). For the super-critical Re, the pressure distribution showed a kink in a range between 100 and 120 deg indicating the formation of laminar separation bubble. The skin-friction exhibited two points of zero indicating flow separation and showed the maximum when the reattachment was made. The second separation was observed far downstream at around 140 deg. For the post-critical Re, the kink was not observed in the pressure distribution and the separation point moved back upstream. Pfeil and Orth (1990) studied the influence of the flow disturbances on the separation and transition of the boundary layer and measured flow transition near the laminar separation bubble for the super-critical Re. The pressure distribution showed a kink in the range between 100 and 114 deg indicating the formation of the separation bubble. The mean streamline near the wall clearly showed the formation of the bubble. The turbulence intensity had a high level of turbulence, over 20% near the bubble and showed sharp gradient across the boundary of the bubble, especially at the maximum thickness as shown in Fig 1.6. It was found that the extent of the separation bubble decreases with flow disturbance in the incoming flow and disappear with higher turbulence disturbances. In summary, the laminar separation bubble has a crucial role in

the drag reduction and characteristic flow feature for the super-critical Re and the narrow band of critical Re. TT correlates with the formation of the laminar separation bubble.

Fig. 1.7 shows the definition of effective shear layer length Ls (Dong et al., 2006) and recirculation length Lr (Williamson, 1996). The Ls is defined by a level of 8% of the maximum mean vorticity magnitude along a vertical line crossing the cylinder axis. The Lr is defined by a distance from the center of the cylinder to the maximum of streamwise component of the Reynolds stress. Table 1.5 shows the DNS and experimental values for Ls and Lr (Dong et al., 2006; Cantwell and Coles, 1983), respectively. The Ls shows decreasing trend with increasing Re up to 10^4. The Lr for Re=$1.41x10^5$ is about 1D from the center of the cylinder.

Fig. 1.8 shows Reynolds stresses u'v' across the wake at x=1D downstream station and u'u' and v'v' along the wake centerline for 0<X/D<8. The u'v' is anti-symmetric about y=0 with maximum values $\pm$.12. The u'u' is maximum near 1.2D and rapidly decreases until 2D followed by gradual decrease. The v'v' shows similar trends as u'u' with its maximum at 1.6D. Fig. 1.9 (a) and (b) show the correlation coefficient for Re=$4.3x10^4$ and $2.4x10^5$ and correlation length against Re. The correlation coefficient rapidly decreases as Δz increases. The correlation length divided by D drops from 10 for Re=10^3 to 3 for the end of the sub-critical Re, suddenly precipitate to 1.5 for the critical Re and stays at that value for the super- and post-critical Re. Thus, large AR domains are required for CFD simulations for the sub-critical Re, e.g. L/D is about 5 for Re=10^4. Fig. 1.10 shows the shear layer frequency divided by the Karman frequency. For the sub-critical Re, the ratio follows a power law of $Re^{.67}$.

URANS methods cannot predict the drag crisis due to its inability to predict boundary layer transition to turbulence since most studies either neglect transition modeling or use models that do not display correct trends. 26th ITTC OEC Report reaches this conclusion based on benchmark studies by several facilities (ITTC, 2011) and recommends future research focused on LES or DNS methods. Table 1.2 summarizes typical studies, including Re range, 2D/3D cylinder simulation, grid size, y+, AR, turbulence model, inflow condition and validation variables. The Re range covers sub- to super-critical Re. Results are both for 2D and 3D

simulations. Grid sizes are coarse. y+ values are often larger than 1. One study with large y+ applied a wall model. AR ranges from 19D to 2D. Several turbulence models are used including one study with transition model. Most of the studies imposed uniform flow condition but one study (R2) adopted forced turbulent intensity to the incoming flow in order to stimulate early turbulent transition. Fig. 1.11 and 1.12 compares URANS studies R1-R4 with the validation variables. Drag coefficient follows a power law Re^{-p} with p mostly about .4 except for R1 as shown in Fig. 11 (a). Separation angle for R2 is over-predicted at the sub-critical Re as shown in Fig. 1.11 (b). The over-prediction is attributed to the early turbulent transition from the incoming flow condition. The separation angle agrees with the experimental data for the super-critical Re. The base suction pressure for R2 is under-predicted due to the delayed separation angle for the sub-critical Re as shown in Fig. 1.11 (c). The base suction pressure matches with the experimental data for the super-critical Re. Mean lift is nearly zero indicating symmetric flow separation as shown in Fig. 1.12 (a). For most studies, RMS lift linearly decreases from large to small values from sub- to super-critical Re as shown in Fig. 1.12 (b). R4 shows nonlinear trends with drop for the critical Re. St is over-predicted for the sub- and critical Re whereas is under-predicted for the super-critical Re, except for R2 as shown in Fig. 1.12 (c). In most cases, RMS lift and St seem to also follow power laws with p about .82 and .1, respectively.

Hybrid methods show some improvements over URANS, but only few studies to reach definitive conclusions. Table 1.2 includes summaries of hybrid methods. The Re range covers sub- to post- critical Re. All results are computed with 3D cylinder. Grid sizes are mostly coarse, but one study uses finer grids (H3). H2 has y+ larger than 1 and adopted wall model. H1 has y+ value close to 1 without wall model. The hybrid methods utilize the RANS approach in the boundary layer with turbulence model including SST k-w, k-e models while LES approach out of the boundary layer with Smagorinsky models. H1 imposed uniform flow condition for the sub- and super-critical Re. H2 adopted forced turbulent intensity to the incoming flow for the sub- and super-critical Re. H3 applied uniform flow condition for the sub-critical Re and forced turbulent intensity to the incoming flow for the post-critical Re. Figs. 1.13-1.16 show compares

hybrid studies H1-H3 with the validation variables. Trends for global/integral variables are hard to determine since three available studies only have two Re, which cover sub- and in two cases super- and in one case post-critical Re; thus, it is not possible to conclude if drag crisis is predicted or not as shown in Fig. 1.13 (a). For the sub-critical Re, all studies under-predict C_D; forced turbulent transition condition (H2) makes lower estimation than other two results. H1 over-predicts C_D for the super-critical Re. H2 and H3 agree with the experimental data for the super- and post-critical Re. H2 has delayed separation angle due to the turbulent transition for the sub-critical Re as shown in Fig. 1.13 (b). The separation angle is under-predicted for the super-critical Re and matches with that at the post-critical Re. H3 predicts the separation angle accurately for the sub- and post-critical Re, respectively. H2 has lower base suction pressure than other study for the sub-critical Re due to the forced turbulent transition and delayed separation angle as shown in Fig. 1.13 (c). For the super- and post-critical Re, the studies show good agreement. H2 shows increasing RMS lift for the sub- to the super-critical Re due to the early transition as shown in Fig. 1.14 (a). H3 shows decreasing RMS lift for the sub- to post-critical Re, respectively. The latter study shows good agreement with one of the facilities data for the sub-and post-critical Re whereas the former study under- and over-predicts for the sub- and super-critical Re, respectively. The predicted St at the sub-critical Re agrees with the experimental data with a little over-prediction without forced turbulent transition as shown in Fig. 1.14 (b). The St with the forced transition shows increasing trend but is under- and over-predicted for the sub- and post-critical Re, respectively. Limited pressure and shear stress distributions are available and the key points marked in Fig. 1.15. The TS at the super-critical Re is estimated by the inflection point of the pressure distributions due to the lack of shear stress distribution. Key point analysis indicates that the distributions at the sub-critical Re are fairly reasonable. For the limited distributions for the super- and post-critical Re within all cases, the key points show trends of the post-critical Re in Table 1.6. The pressure distribution at the super-critical Re is lack of the separation bubble. Fig. 1.16 graphically displays the key points for the Fig. 1.15 distributions. The distance of LS is 9 deg downstream from MP for the sub-critical Re.

For the super–critical Re, TS is 34 deg downstream with MP without any other transitions and remains almost constant with increasing Re. For the post-critical Re, TS is 31 deg downstream from MP and recovers about 3 deg in comparison with that at the super-critical regime.

LES methods show promise to predict smooth surface separation of cylinder, but only few studies can reach definitive conclusions. Table 1.2 includes summaries of LES methods. The Re range covers sub- to super-critical Re. All results are 3D cylinder simulations. Grid sizes are relatively coarse for LES as mostly under 10M. y+ values are less than 1 so boundary layer is resolved with grid. AR is less than 2 for all the flow regimes. CDS and upwind schemes are used. Mostly dynamic Smagorinsky LES model is used. Figs. 1.17-1.20 compare the LES studies L1-L4 with the validation variables. L3 predicts the drag crises while L4 suggests that capability but lacks super-critical results as shown in Fig. 1.17 (a). L2 shows good agreement for the sub-and super-critical Re but lacks critical results, and L1 shows good agreement for the super-critical Re but lacks other regimes. L1 shows reasonable key point angles, but under-predicts TS as shown in Fig. 1.17 (b). Two studies (L1 and L2) show good agreement for the base suction pressure as shown in Fig. 1.17 (c). Mean lift is nearly zero indicating symmetric flow separation for all the Re studied as shown in Fig. 1.18 (a). RMS lift shows fairly good agreement with one study showing critical like behavior (L3) as shown in Fig. 1.18 (b). Studies roughly show St trends, although in L4 with over-prediction as shown in Fig. 1.18 (c). Pressure and shear stress distributions are limited as shown in Fig. 1.19. Key point analysis for the super-critical Re shows qualitatively correct trends including the laminar separation bubble as shown in Table 1.7; however, TS are under-predicted at 112 deg instead of about 148 deg as shown in Fig. 1.20.

The convective terms in the momentum equations are given in an advective form (non-conservative form) from the derivation. With the continuity equation, they can also be written in a divergence form (conservative form). Sometimes a skew-symmetric form, as an arithmetic average of the advective and divergence forms, is also used in the literature (Morinish et al. 1998). Analytically, these three forms are equivalent. However, they can be quite different in

terms of numerical conservation and stability properties after discretization. In numerical simulations of free-surface or two-phase incompressible flows, usually the continuity and momentum equations are solved with the density only in the stresses and the free surface or the interface is advected using front tracking methods or interface-capture methods such as level set and volume of fluid methods. The discrepancy between volume conservation and mass conservation can make the divergence form of the convective terms numerically unstable unless the grid resolution is high enough to minimize it. Therefore, the advective form is widely used in free-surface and two-phase flow simulations. In Suh et al. (2011), LES of turbulent flow past an interface-piercing circular cylinder was performed with the advective form of the convective terms in the momentum equations. The Reynolds number is relatively low and a good agreement with reference data was observed. In Koo et al. (2014), the same problem, but with much higher Reynolds numbers, was studied. It was found that the deep flow did not follow the single flow pattern and it was concluded that the problem was mostly caused by the marginal grid resolution and the advective form of the convective terms that does not conserve momentum and kinetic energy.

In single-phase flow simulations, the divergence form of the convective terms can be used to guarantee the conservation of momentum in the solution process of the momentum equations without incurring numerical stability issues mentioned above. However, the conservation of kinetic energy is not that easy to achieve as there is no stand-alone equation for the kinetic energy transport, which can only be derived from the momentum equations. In direct numerical simulations of turbulent flows, the Kolmogorov scale is fully resolved and numerical schemes that do not conserve kinetic energy will not adversely change the energy cascade and affect the simulation results. In LES, however, only the large, energy carrying scales are resolved and scales smaller than the grid resolution have to be modeled. A subgrid scale (SGS) stress model is expected to remove exactly the amount of energy that corresponds to the scales beyond the grid cutoff length scales from the flow. With a numerical scheme that does not conserve the kinetic energy, the effectiveness and accuracy of the SGS model cannot be readily quantified. On

one hand, the simulation results may be contaminated by numerical errors from the kinetic energy non-conserving schemes. On the other hand, this is especially critical for situations in which too less energy is removed from the flow and the solution may become soon unstable due to the energy pileup in the solution field. Therefore, it is of great importance to adopt an energy conservative convection scheme for LES.

It is well-known that central difference schemes (CDS) are desirable in LES for their energy conservation properties and there are a lot of applications of CDS in LES of relatively low Reynolds number flows in simple geometries. Unfortunately, CDS are quite sensitive to grid quality. If the grid orthogonality is not optimal and the grid stretching factor is relatively large, which are usually necessary for high Reynolds number flows in complex geometries, the dispersion errors may become prominent, showing as short wavelength wiggles in the flow field, and make the solution useless. Upwind schemes have both dispersion and dissipation errors, but the latter are the leading-order errors in truncation errors. The dissipative properties of the upwind schemes can be helpful with removing the wiggles from the dispersion errors, although this is achieved at a price of dissipated energy. Therefore, a compromise for LES of high Reynolds number turbulent flows in complex geometries has to be made by allowing artificial energy dissipation at least in regions that the grid quality is not optimal for CDS. In addition, different upwind schemes show different dissipation errors. The first-order upwind scheme, which is usually the default choice of convection schemes in many commercial RANS solvers, is too dissipative for LES and should not be used. The third-order QUICK scheme is frequently used in LES of turbulent flows in simple geometries. The fifth-order WENO scheme is widely recognized for its high resolution, great flexibility, and low dissipation, though more expensive than the QUICK scheme.

It is possible to conserve momentum and kinetic energy with non-conservative convection schemes. In Lentine et al. (2011), a semi-Lagrangian advection scheme was developed to achieve this gain. A two-step approach was adopted in which the second step was designed to advect and distribute residual momentum and kinetic energy left out in the first step,

such that the final solution field conserves both momentum and energy. However, the applicability of this type of approaches in a LES setting is unclear yet.

In URANS, the correlation between the TKE production and dissipation can be studied by the TKE and viscous dissipation equations, e.g., the k-epsilon model. In LES, the estimation of TKE budgets are made with resolved solutions. The derivation of the resolved-scale TKE budgets in LES is not the same as traditional TKE budgets since the unresolved-scale information is removed from the solutions through the filtering operation in LES and modeled with subgrid-scale stress term (Yue et al., 2008). Due to the subgrid-scale stress term in the filtered Navier-Stokes equations, an additional term indicating transfer of energy from the resolved to the subgrid-scale is derived apart from the usual TKE budgets including turbulent convection, turbulent production, viscous dissipation, viscous diffusion, turbulent transport and pressure transport terms. The contribution of the additional term to the resolved-scale TKE budgets can be negligible as the turbulent eddy viscosity becomes small with increasing Re (Lopes et al, 2006). An energy conservative convection scheme should be used since the energy loss or energy pileup can significantly influence the LES solutions and eventually lead to incorrect TKE budget estimation (Sagaut, 2005). Quality of the energy spectrum resolved by the LES, especially energy decaying rate can be affected by the numerical dissipation due to the numerical scheme used (Mittal and Moin, 1990). In the process of computation of TKE budgets with a staggered grid, some imbalances can be observed since linear interpolation can produce numerical errors in the regions of strong shear and sharp gradient estimation (Yue et al., 2008). Since the analysis of the TKE budgets are assumed statistically stationary condition, a large volume of data is needed with expensive computational cost. The specific data size varies with flow type, e.g. over 150 averaging time scales for the shallow cumulus convective flows (Grant and Lock, 2004). The viscous dissipation occurs in small-scale (Kolmogorov scale) and will be under-estimated in the dissipated energy spectrum since the estimation of TKE budgets are made with resolved solutions without solving any TKE and viscous dissipation equations in LES. However, turbulence statistics including the Reynolds stresses are hardly affected except for the

case such as reactional flows even though the energy spectra shows considerable dissipation (Mittal and Moin, 1997). Yue et al. (2008) used CDS scheme for the LES study for low Re (Re=650); the resolved-scale viscous dissipative term was balanced with the turbulent production term. Yue et al. (2008) found that the ratio of residual (sum of all TKE budgets) to production term became about 0.1 in the shear layer.

Proper Orthogonal Decomposition (POD) method is a quantitative method for identifying the most energetic modes of instantaneous turbulent field and provides an effective way to extract coherent structure from the large volume of data with an linear combination of basis function (POD mode), e.g. snapshot POD method (Sirovisch, 1987). Recently, POD has been used in various flows including jets, channel flows and cylinder wakes as a technique for identifying not only the dominant features in flows but also for constructing a low-dimensional description of the flow dynamics (Dean et al. 1991; Ma et al, 2000; Perrin et al, 2007).

The POD allows for large-scale structures to be isolated from the small-scale structures. For example, DNS studies for Re=200 (Dean et al., 1991; Ma et al., 2000) and an experiment for Re= 1.4×10^5 (Perrin et al., 2007) were conducted for the flow past a circular cylinder and the POD method was applied to near wake. In the studies, a large fraction of kinetic energy was taken by the first two POD modes and higher modes showed rapid decay. The topologies of the first two POD modes formed pairs with a shift in the streamwise direction. The first two POD modes are highly correlated to the convection of the Karman shedding vortices. Reconstruction of flow field with higher POD modes just add smaller scale flow structures to the Karman shedding vortices.

Despite the usefulness in the extraction of dominant flow structures, the application of POD has limitations (Berkooz et al. 1993). The quality POD method is strongly dependent on the TKE intensity and proper choice of analysis region. If the TKE intensity is small in the region or broad range is selected as an analysis region, e.g. whole flow field instead of small region, the POD results are degraded and hard to observe clear flow structures. For instance, for the turbulent flow with a variety of length scales for a high Re, the POD analysis may require several

hundred modes to capture a large contribution of the kinetic energy in the flow, especially in the shear layer and boundary layer. In addition, the POD modes only represent time average information about flow structures since the POD is based on time averaged correlations.

1.2 Objectives and Approach

The objective of this thesis is to perform high-fidelity LES to investigate issues for current LES: only sparsely covers Re regimes up to the super-critical Re, use small AR especially at the sub-critical Re, use relatively coarse grids for the boundary layer, and do not make full use of the available experimental benchmark validation data. The effects of convection schemes including QUICK and WENO are also studied for the sub-, critical and super-critical Re. The influence of the conservative and non-conservative schemes in the solutions will be investigated in preparation of two-phase flow simulation for the super-critical Re since the CFDShip-Iowa V6.2 employs a non-conservative scheme for the two-phase flow simulation.

CFDShip-Iowa V6.2 is used for the high fidelity LES. Section 2 describes the computational methods, including modeling, numerical methods, HPC, computational setup, and analysis methods. Section 3 describes the verification and domain size studies, including statistical convergence, grid verification, and sensitivity studies for effects of AR, grid and convection scheme. Based on these studies using 30 simulations, 6 simulations covering sub to super critical were selected for submission ITTC OEC Workshop and used herein for validation and additional diagnostics, as described in Sections 4 and 5, respectively. The most in-depth studies are for three Re, which cover sub-, critical and super-critical Re. Section 6 provides overall conclusions and recommendations for future research.

1.3 References

1. Achenbach, E. (1968). Distribution of local pressure and skin friction around a circular cylinder in cross-flow up to Re= 5 x 106. Journal of Fluid Mechanics, Cambridge Univ Press. **34:** 625-639.

2. Bearman, P. W. (1969). On vortex shedding from a circular cylinder in the critical Reynolds number regime. Journal of Fluid Mechanics, Cambridge Univ Press. **37:** 577-585.

3. Bearman, P.W., Wadcock, A.J. (1973). The interaction between a pair of circular cylinders normal to a stream. Journal of Fluid Mechanics. 61: 499-511

4. Berkooz G, Holmes P, Lumley J (1993) The proper orthogonal decomposition in the analysis of turbulent flows. Annu Rev Fluid Mech 25:539–75

5. Bloor, M. S. (1964). The transition to turbulence in the wake of a circular cylinder. J. Fluid Mech.19: 290

6. Bruun, H.H., Davies, P.O.A.L. (1975). An experimental investigation of the unsteady pressure forces on a circular cylinder in a turbulent cross flow. Journal of Sound and Vibration. 40: 535-559

7. Cantwell, B. and D. Coles (1983). An experimental study of entrainment and transport in the turbulent near wake of a circular cylinder. Journal of Fluid Mechanics, Cambridge Univ Press. **136:** 321-374.

8. Deane, A. E., I. G. Kevrekidis, G. E. Karniadakis and S. A. Orszag (1991). Low-dimensional models for complex geometry flows: Application to grooved channels and circular cylinders. Physics of Fluids A: Fluid Dynamics, AIP Publishing. 3: 2337-2354.

9. Dong, S., G. E. Karniadakis, A. Ekmekci and D. Rockwell (2006). A combined direct numerical simulation–particle image velocimetry study of the turbulent near wake. Journal of Fluid Mechanics, Cambridge University Press. 569: 185-207.

10. Fage, A. and V. M. Falkner (1931). Further Experiments on the Flow Around a Circular Cylinder. Aeronautical Research Council Reports and Memoranda 1, No. 1369, 186-195.

11. Grant, A. L. M., and A. P. Lock. (2004), The turbulent kinetic energy budget for shallow cumulus convection. Quarterly Journal of the Royal Meteorological Society, 130: 401-422

12. Iida, A., Otaguro, T., Kato, C., Fujita, H. (1997). Prediction of aerodynamic sound spectra from a circular cylinder. In: S. of Instrument, C. E. of Japan (Eds.), Proceedings of the 5th Triennial International Symposium on Fluid Control, Measurement and Visualization (FLUCOME '97), Vol. 1. Hayama, Japan, 1–4 September, 1997, 126–131.

13. James, M. and Lloyd, T. (2013). Large Eddy Simulations of Circular Cylinders at a range of Reynolds Numbers. Proceedings of the 27th ITTC Workshop on Wave Run-up and Vortex Shedding.

14. Kacker, S.C., Pennington, B., Hill, R.S. (1974). Fluctuating lift coefficient for a circular cylinder in cross flow. Journal Mechanical Engineering Science 16: 215–224

15. Kim, S.-E. and L. S. Mohan (2005). Prediction of unsteady loading on a circular cylinder in high Reynolds number flows using large eddy simulation. ASME 2005 24th International Conference on Offshore Mechanics and Arctic Engineering: 775-783.

16. Kourta, A., Boisson, H. C., Chassaing, P. & Ha Minh, H. (1987). Nonlinear interaction and the transition to turbulence in the wake of a circular cylinder. J. Fluid Mech. 181: 141.

17. Lee, K. and Yang, K.S. (2013). Large Eddy Simulation of Turbulent Fow Past a Circular Cylinder. Proceedings of the 27th ITTC Workshop on Wave Run-up and Vortex Shedding.

18. Leehey, P., Hanson, C.E. (1971). Aeolian tones associated with resonated vibration. Journal of Sound and Vibration 13: 465–483

19. Lentine, M., Grétarsson, J. and Fedkiw, R., "An Unconditionally Stable Fully Conservative Semi-Lagrangian Method", J. Comp. Phys. 230, 2857-2879 (2011).

20. Ma, X., G. S. Karamanos and G. E. Karniadakis (2000). Dynamics and low-dimensionality of a turbulent near wake. Journal of Fluid Mechanics, Cambridge University Press. 410: 29-65.

21. Maekawa, T. & Mizuno, S. (1967). Flow around the separation point and in the near-wake of a circular cylinder. Phys. Fluids Suppl. S184.

22. Mittal, Rajat and Moin, Parviz (1997), Suitability of Upwind-Biased Finite Difference Schemes for Large-Eddy Simulation of Turbulent Flows, AIAA, 35:1415-1417

23. Moeller, M.J. (1982). Measurement of unsteady forces on a circular cylinder in cross flowat subcritical Reynolds numbers, Ph.D. Thesis, Massachusetts Institute of Technology, USA

24. Morinishi, Y., T. S. Lund, O. V. Vasilyev, and P. Moin. (1998), Fully conservative higher order finite difference schemes for incompressible flow. Journal of computational physics 143:90-124.

25. Moussaed, C., M. V. Salvetti, S. Wornom, B. Koobus and A. Dervieux (2013). Simulation of the flow past a circular cylinder in the supercritical regime by blending RANS and variational-multiscale LES models. Journal of Fluids and Structures.

26. Norberg, C. (1987). Effects of Reynolds number and a low-intensity freestream turbulence on the flow around a circular cylinder. Dept of Appl Thermodynamics and Fluid Mech.

27. Norberg, C. (1992). Pressure forces on a circular cylinder in cross flow. IUTAM Symposium on Bluff Body Wakes, Dynamics and Instabilities**:** 275-278.

28. Novak, M., Tanaka, H. (1977). Pressure correlations on a vibrating cylinder. In: Eaton, K.J. (Ed.), Proceedings of the 4th International Conference on Wind Effects on Buildings and Structures, Heathrow, UK, 1975, Cambridge University Press, Cambridge 227–232

29. Okamoto, S., Hirose, T. & Adachi, T. (1981). The effect of sound on the vortex-shedding from a circular cylinder. Bull. JSME 24: 45.

30. Ono, Y. and T. Tamura (2008). LES of flows around a circular cylinder in the critical reynolds number region. Proc. 6 th International Conference on Bluff Body Aerodynamics and Applications: 1-10.

31. Pfeil H. and Orth U. (1990), Boundary-layer transition on a cylinder with and without separation bubbles. Experiments in Fluids, **10**:23-32

32. Perrin, R., M. Braza, E. Cid, S. Cazin, A. Barthet, A. Sevrain, C. Mockett and F. Thiele (2007). Obtaining phase averaged turbulence properties in the near wake of a circular cylinder at high Reynolds number using POD. Exp Fluids. 43: 341-355.

33. Roshko, A. (1953). On the drag and shedding frequency of two-dimensional bluff bodies. National Advisory Committee for Aeronautics, NACA TN 3169. (Th. Exp. Notch hodograph theory). 3,5.

34. Roshko, A. (1961). Experiments on the flow past a circular cylinder at very high Reynolds number. Journal of Fluid Mechanics, Cambridge Univ Press. **10:** 345-356.

35. Schewe, G. (1983). On the force fluctuations acting on a circular cylinder in crossflow from subcritical up to transcritical Reynolds numbers. Journal of Fluid Mechanics, Cambridge Univ Press. **133:** 265-285.

36. Sonneville, P. (1976). Etude de la structure tridimensionelle des ecoulements autour d'un cylindre circulaire, Bulletin de la Direction des Etudes et Recherches, Serie A, No. 3 – 1976, Electricite de France.

37. Sumer, B Mutlu. (2006). Hydrodynamics around cylindrical structures. World Scientific.

38. Shih, W., C. Wang, D. Coles and A. Roshko (1993). Experiments on flow past rough circular cylinders at large Reynolds numbers. Journal of Wind Engineering and Industrial Aerodynamics, Elsevier. **49:** 351-368.

39. Szepessy, S. and P. W. Bearman (1992). Aspect ratio and end plate effects on vortex shedding from a circular cylinder. Journal of Fluid Mechanics.

40. Travin, A., M. Shur, M. Strelets and P. Spalart (2000). Detached-eddy simulations past a circular cylinder. Flow, Turbulence and Combustion, Springer. 63: 293-313.

41. Vaz, G., C. Mabilat, R. van der Wal and P. Gallagher (2007). Viscous Flow Computations on a Smooth Cylinders: A Detailed Numerical Study With Validation.

Proceedings of the 26th International Conference on Offshore Mechanics and Arctic Engineering.

42. Warschauer, K.A. and Leene, J.A. (1971). Experiments on mean and fluctuating pressures of circular cylinders at cross flow at very high Reynolds numbers. Proceedings of International Conference on Wind Effects on Buildings and Structures.

43. Wei, T. & Smith, C. R. (1986). Secondary vortices in the wake of circular cylinders. J. Fluid Mech. 169:513.

44. Wen Peng and Qiu Wei (2013). Numerical Studies of VIV of a Smooth Cylinder. Proceedings of the 27th ITTC Workshop on Wave Run-up and Vortex Shedding.

45. West, G. S. and C. J. Apelt (1993). Measurements of Fluctuating Pressures and Forces on a Circular Cylinder in the Reynolds Number Range 104 to 2·5 × 105. Journal of Fluids and Structures. **7:** 227-244.

46. Wieselsberger, C. v. (1921). Neuere feststellungen über die gesetze des flüssigkeits-und luftwiderstands. Phys. Z. **22:** 321-328.

47. Williamson, C. (1996). Vortex dynamics in the cylinder wake. Annual Review of Fluid Mechanics, Annual Reviews 4139 El Camino Way, PO Box 10139, Palo Alto, CA 94303-0139, USA. 28: 477-539.

48. Ye, H., Zhong, Q. and Wan, D. (2013). Benchmark Computations of Flows around a Stationary Cylinder with High Reynolds number by RANS-Overset Grid Approach. Proceedings of the 27th ITTC Workshop on Wave Run-up and Vortex Shedding.

49. Yue, Wusi, Charles Meneveau, Marc B. Parlange, Weihong Zhu, Hyung Suk Kang, and Joseph Katz. (2008), Turbulent kinetic energy budgets in a model canopy: comparisons between LES and wind-tunnel experiments. Environmental Fluid Mechanics 8: 73-95.

50. Yeon, Seong Mo, Yang Jianming and Stern Frederick (2013). Large Eddy Simulation of Drag Crisis in Turbulent Flow Past a Circular Cylinder. Proceedings of the 27th ITTC Workshop on Wave Run-up and Vortex Shedding.

Table 1.1 Summary of experimental studies and validation variables

EFD	Re ($x10^{-5}$)	Aspect ratio (L/D)	Tu (%)	Roughness (k/D)	Blockage (%)	Variables
Wieselsberger (1921)	Sub-post	N/A	N/A	N/A	N/A	C_D
Achenbach (1968)	0.6-50	Abt 3.3	0.7	Smooth	17	C_D, θ_s, Cp and Cf
Schewe (1983)	0.2-71	10	0.4	Smooth	10	C_D, C_L, C_L^{rms} and St
MARIN exp.	Abt.0.3-8	Abt 18.6	N/A	N/A	N/A	C_D
Bearman (1969)	1-7.5	12	0.2	Smooth	6.5	C_D, C_L, -Cpb and St
Norberg (1987)	0.0005-2	2	0.1	Smooth	1	-Cpb
Shih et al. (1993)	3-80	Abt. 8.2	N/A	$3.0x10^{-4}$	11	-Cpb
Szepessy and Bearman (1992)	0.08-1.4	6.7	0.05	N/A	7.7	C_L^{rms}
West and Apelt (1993)	0.11-2.2	15-35	0.2	Smooth	8.2	St
Roshko (1953)	0.8-4.5	N/A	N/A	N/A	N/A	St
Cantwell and Coles (1983)	0.69-3.37	>10	<1	Smooth	<10	Cp and Cf
Bearman and Wadcock (1973)	0.025	N/A	N/A	N/A	N/A	Λ
Bruun and Davies (1975)	0.6-6	10	0.1	Smooth	13	R_{pp},Λ
Iida et al. (1997)	0.06-1.5	N/A	N/A	N/A	N/A	Λ
Kacker et al. (1974)	0.1-3	8.0	0.4	Smooth	4.7	Λ
Leehey and Hanson (1971)	0.04-0.07	97	0.04	Smooth	Open jet	R_{pp}, Λ
Moeller (1982)	0.05-0.56	16/19	0.3	Smooth	Open jet	Λ
Novak and Tanaka (1977)	0.02	N/A	N/A	N/A	N/A	Λ
Sonneville (1976)	0.45	13	0.4	N/A	5.6	Λ
Szepessy (1974)	0.43	10	0.05	Smooth	7.7	Λ
Maekawa and Mizuno (1967)	0.37-2.8	3	N/A	Smooth	23	f_{SL}
Bloor (1964)	0.002-0.5	20-655	0.03	Smooth	5	f_{SL}
Kourta et al. (1987)	0.02-0.6	7	0.1	Smooth	3	f_{SL}
Okamoto et al. (1981)	0.025-0.045	4	N/A	Smooth	8	f_{SL}
Wei and Smith (1986)	0.012-0.11	14-34	N/A	Smooth	1-19	f_{SL}

Table 1.2 Summary of numerical studies and validation variables

	Author	Re ($x10^{-5}$)	Method	2D/3D	Grid size (Mil.)	y+	Wall model	AR (L/D)	Convection scheme	Turbulent model	Inflow Condition	variables
R1	Vaz et al. (2007)	0.93/5.5	URANS	2D/3D	0.16 1.2	1	No	18.6	N/A	k-w k-w+transition RSTM	Uniform	C_D St
R2	Moussaed et al. (2013)	1.4-12.5		3D	0.46 1.40	28	Yes	2	N/A	k-e	Forced Turbulent Intensity	C_D C_L^{rms} $-C_{pb}$ St C_p θ_s
R3	Wen and Qui (2013)	0.631-7.57		2D	N/A	24-225 (coarse) 12-112 (medium) 6-56 (fine)	N/A	N/A	N/A	SST k-w k-e RSTM	Uniform	C_D C_L C_L^{rms} St
R4	Ye et al. (2013)	0.631-7.57		3D	N/A	N/A	N/A	N/A	N/A	N/A	N/A	C_D C_L C_L^{rms} St
H1	Vaz et al. (2007)	0.93/5.5	Hybrid	3D	1.2	1	No	18.6	N/A	DES (SST k-w/DSM)	Uniform	C_D St
H2	Moussaed et al. (2013)	1.4-12.5		3D	0.4 1.40	28	Yes	2	N/A	Hybrid RANS/VMS-LES (k-e/DSM)	Forced Turbulent Intensity	C_D C_L^{rms} $-C_{pb}$ St C_p θ_s
H3	Travin et al (2000)	0.056-36		3D	11 32	N/A	N/A	2	Upwind	DES (SST k-w/DSM)	Uniform/ Forced Turbulent Intensity	C_D C_L^{rms} $-C_{pb}$ St θ_s
L1	Ono and Tamura (2008)	6	LES	3D	4 13	N/A	No	2 1	Higher-order interpolation method	DSM DMM	Uniform	C_D C_L^{rms} St C_p C_f θ_s
L2	Kim and Mohan (2005)	1.4/10 10		3D	6.8	< 1	No	2	CDS	DSM	Uniform	C_D C_L^{rms} $-C_{pb}$ St C_p C_f
L3	James and Lloyd (2013)	0.631-7.57		3D	2 – 6	1	No	1.7	CDS CDS+upwind	SSM DSM	Uniform	C_D C_L C_L^{rms} St
L4	Lee and Yang (2013)	0.631-7.57		3D	N/A	N/A	N/A	N/A	N/A	DSM	N/A	C_D C_L C_L^{rms} St

where SSM: Standard Smagorinsky model, DSM: Dynamic Smagorinsky model and DMM: Dynamic mixed model

Table 1.3 Key point angles (Achenbach, 1968)

	Re	θ_{MP} (deg)	θ_{LS} (deg)	$\delta(\theta_{LS}-\theta_{MP})$ (deg)	θ_{TT} (deg)	$\delta(\theta_{TT}-\theta_{LS})$ (deg)	θ_{TR} (deg)	$\delta(\theta_{TR}-\theta_{LS})$ (deg)	θ_{TS} (deg)	$\delta(\theta_{TS}-\theta_{MP/LS/TR})$ (deg)
Sub-critical	$1.0x10^5$	75	80	5						
Critical	$2.1x10^5$	78	89	9						
	$2.6x10^5$	74	94	20						
Super-critical	$8.5x10^5$	110	110	0			120	10	148	28
Post-critical	$3.6x10^6$	79							110	31

Table 1.4 Key point angles (Pfeil and Orth, 1990)

	Re	θ_{MP} (deg)	θ_{LS} (deg)	$\delta(\theta_{LS}-\theta_{MP})$ (deg)	θ_{TT} (deg)	$\delta(\theta_{TT}-\theta_{LS})$ (deg)	θ_{TR} (deg)	$\delta(\theta_{TR}-\theta_{LS})$ (deg)	θ_{TS} (deg)	$\delta(\theta_{TS}-\theta_{MP/LS/TR})$ (deg)
Super-critical	$6.0x10^5$		100		110	10	114	4		

Table 1.5 Effective shear layer length Ls and recirculation length Lr

	Re	L_s/D	L_r/D
Experiment(Cantwell and Coles 1983)	$1.41x10^5$	-	0.94
DNS(Dong et al. 2006)	$3.90x10^3$	1.59	-
	$1.00x10^4$	1.03	-

Table 1.6 Key point angles for hybrid methods

	Re	θ_{MP} (deg)	θ_{LS} (deg)	$\delta(\theta_{LS}-\theta_{MP})$ (deg)	θ_{TT} (deg)	$\delta(\theta_{TT}-\theta_{LS})$ (deg)	θ_{TR} (deg)	$\delta(\theta_{TR}-\theta_{LS})$ (deg)	θ_{TS} (deg)	$\delta(\theta_{TS}-\theta_{MP/LS/TR})$ (deg)
Sub-critical	$1.4x10^5$	68	77	9						
Super-critical	$6.7x10^5$	84							118	34
	$1.25x10^6$	84							117	33
Post-critical	$3.6x10^6$	80							111	31

Table 1.7 Key point angles for LES

	Re	θ_{MP} (deg)	θ_{LS} (deg)	$\delta(\theta_{LS}-\theta_{MP})$ (deg)	θ_{TT} (deg)	$\delta(\theta_{TT}-\theta_{LS})$ (deg)	θ_{TR} (deg)	$\delta(\theta_{TR}-\theta_{LS})$ (deg)	θ_{TS} (deg)	$\delta(\theta_{TS}-\theta_{MP/LS/TR})$ (deg)
Super-critical	$6.0x10^5$	84	97	13			104	7	112	8

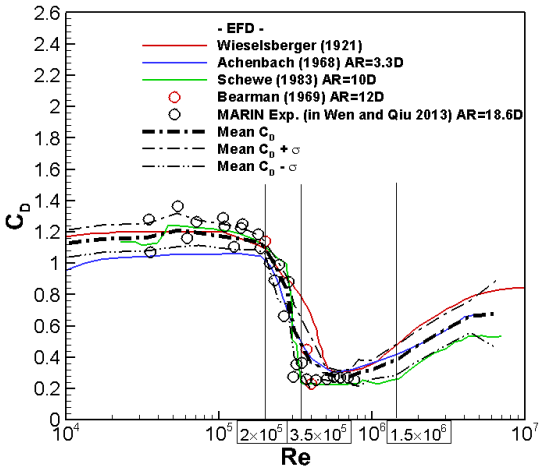

(a) C_D

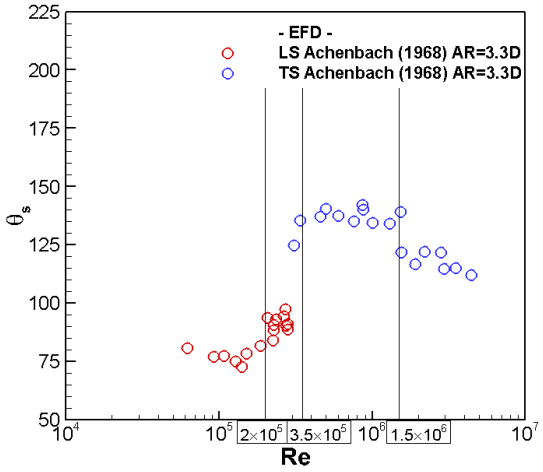

(b) θ_s

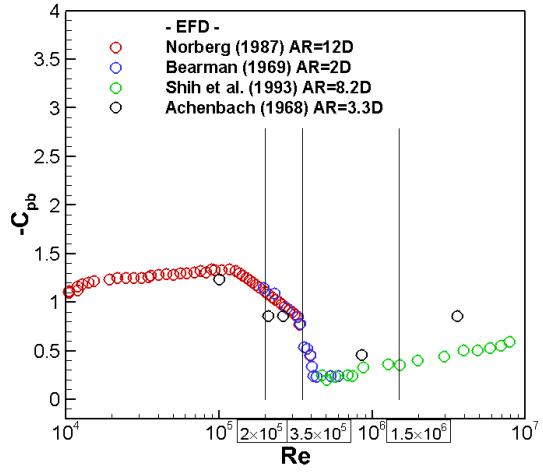

(c) $-C_{pb}$

Figure 1.1 Drag, separation angle and base pressure vs. Re (EFD)

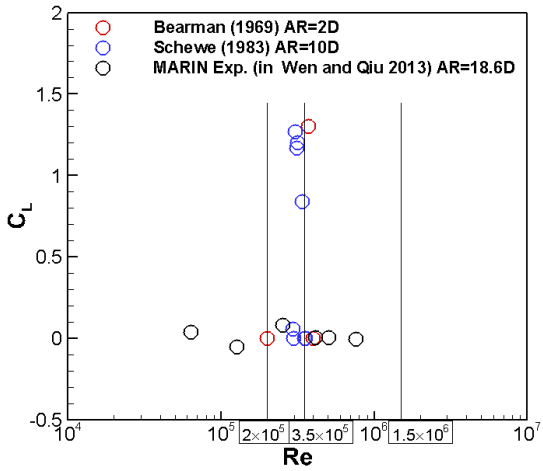

(a) Mean C_L

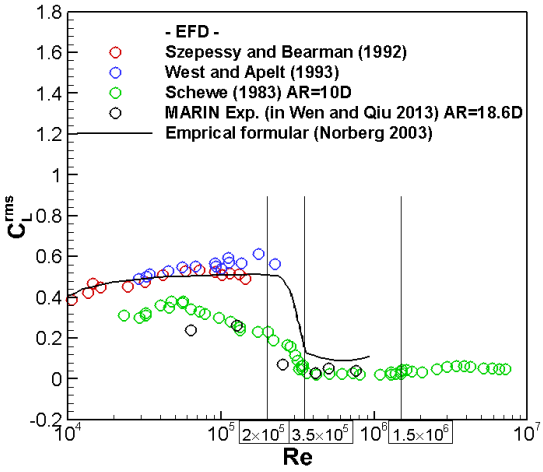

(b) C_L^{rms}

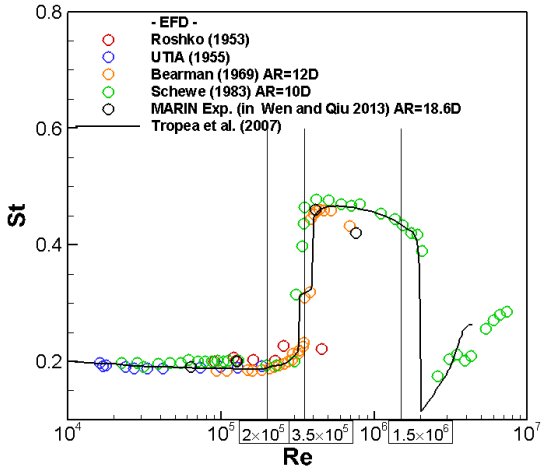

(c) St

Figure 1.2 RMS lift coefficient and Strouhal number vs. Re (EFD)

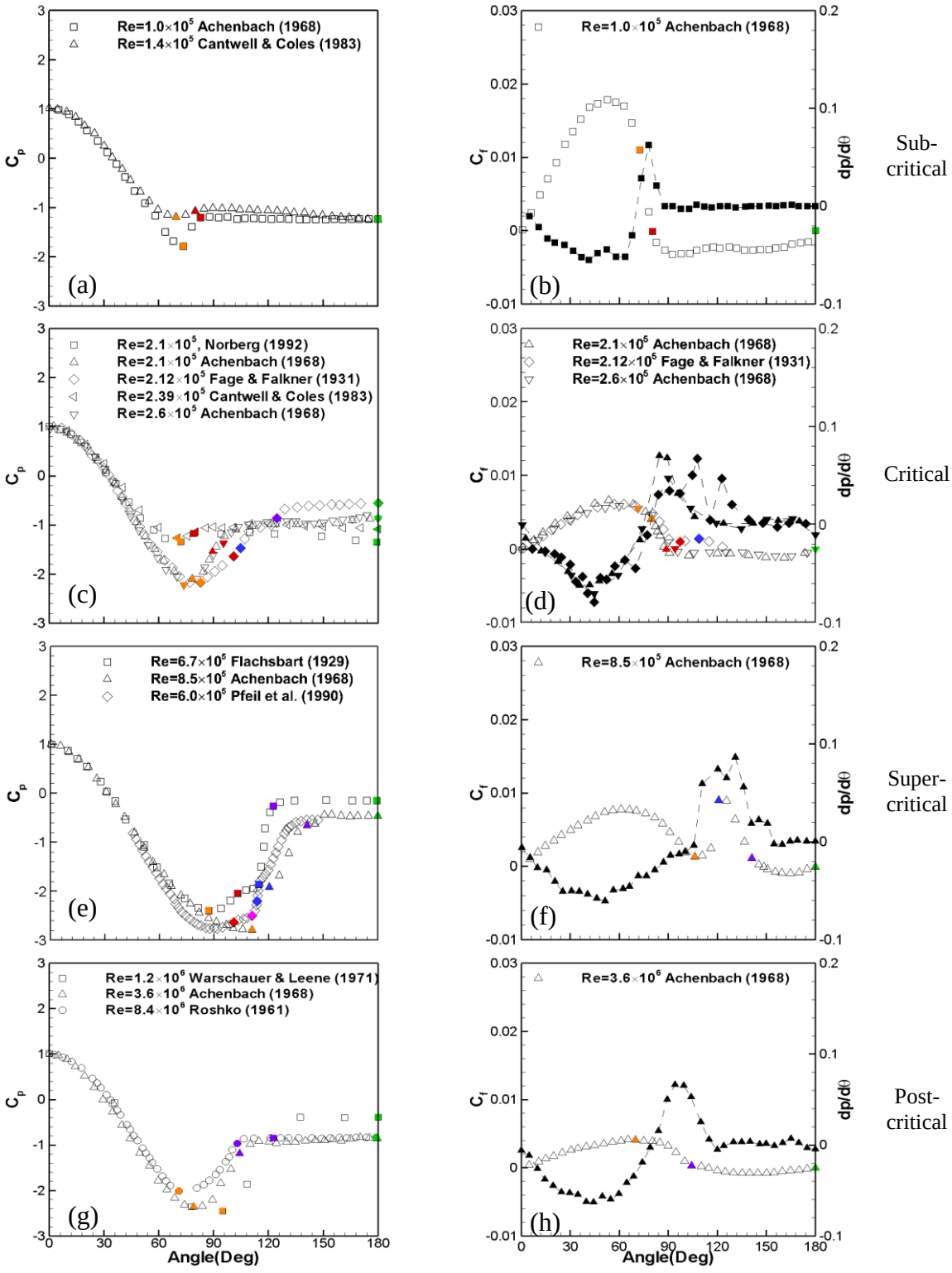

Figure 1.3 Pressure (left) and skin-friction (right) (EFD); orange=MP, red=LS, magenta=TT, blue=TR, purple=TS and green=BP. Solid black symbols overlaid on the skin-friction are angular pressure gradient.

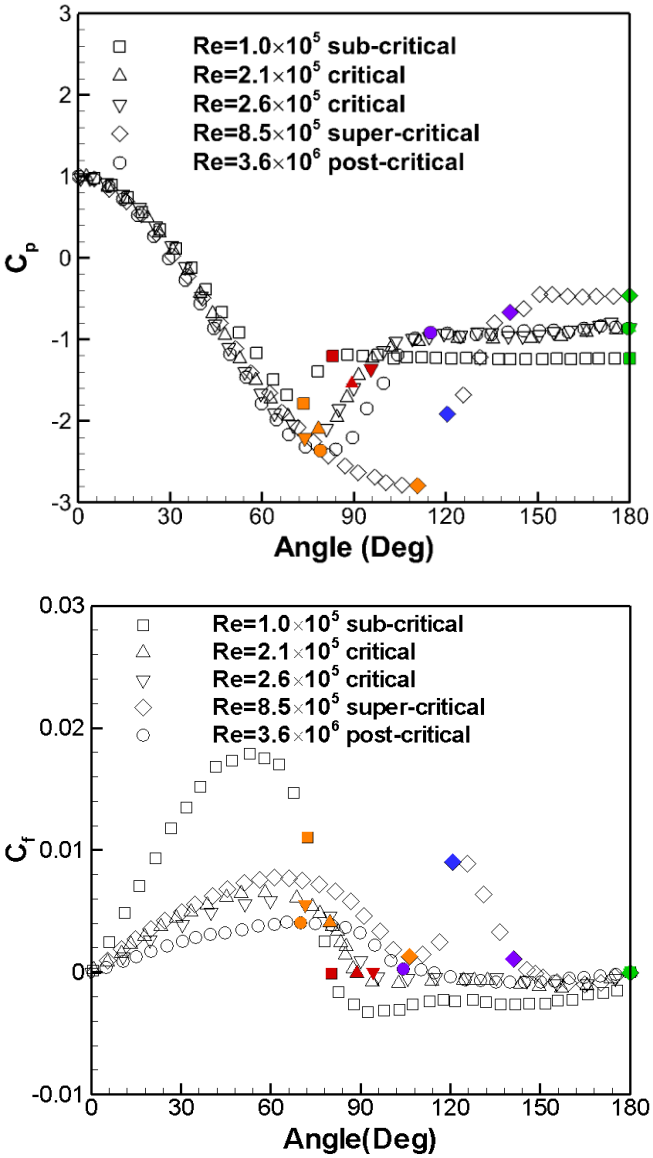

Figure 1.4 Pressure (up) and skin-friction (bottom) (EFD); orange=MP, red=LS, blue=TR, purple=TS and green=BP. The TR is corresponding to the end of the laminar separation bubble.

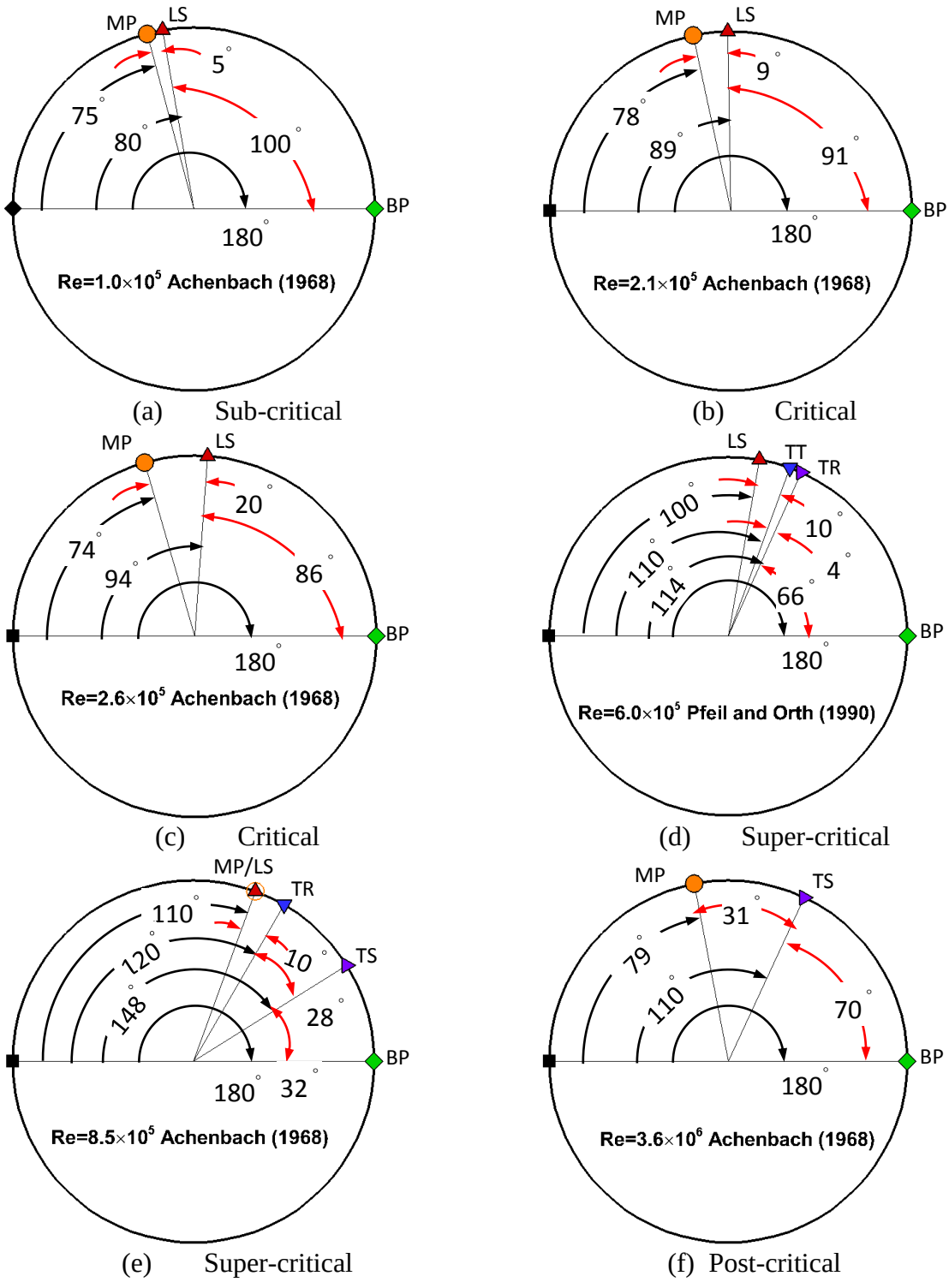

Figure 1.5 MP, LS, LR, TS and BP points on the cylinder (EFD); ●=MP, ▲=LS, ▼=TR, ▶ =TS and ◆=BP.

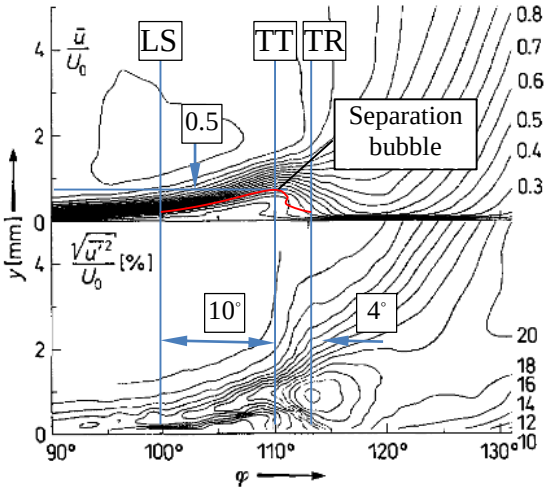

Figure 1.6 Mean velocity (top) and turbulence intensity (bottom) for Re=6x10^5 (Pfeil and Orth, 1990)

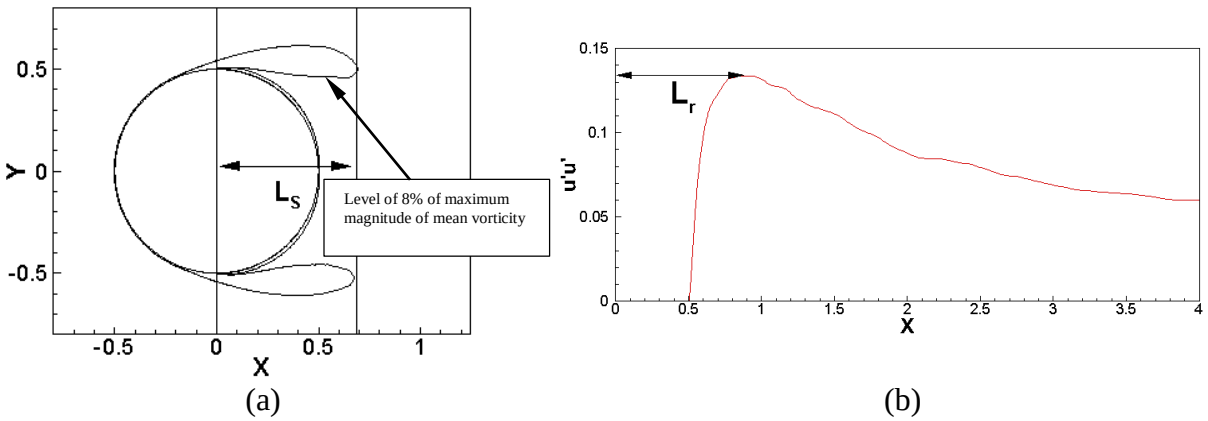

Figure 1.7 Definition of (a) L_s and (b) L_r

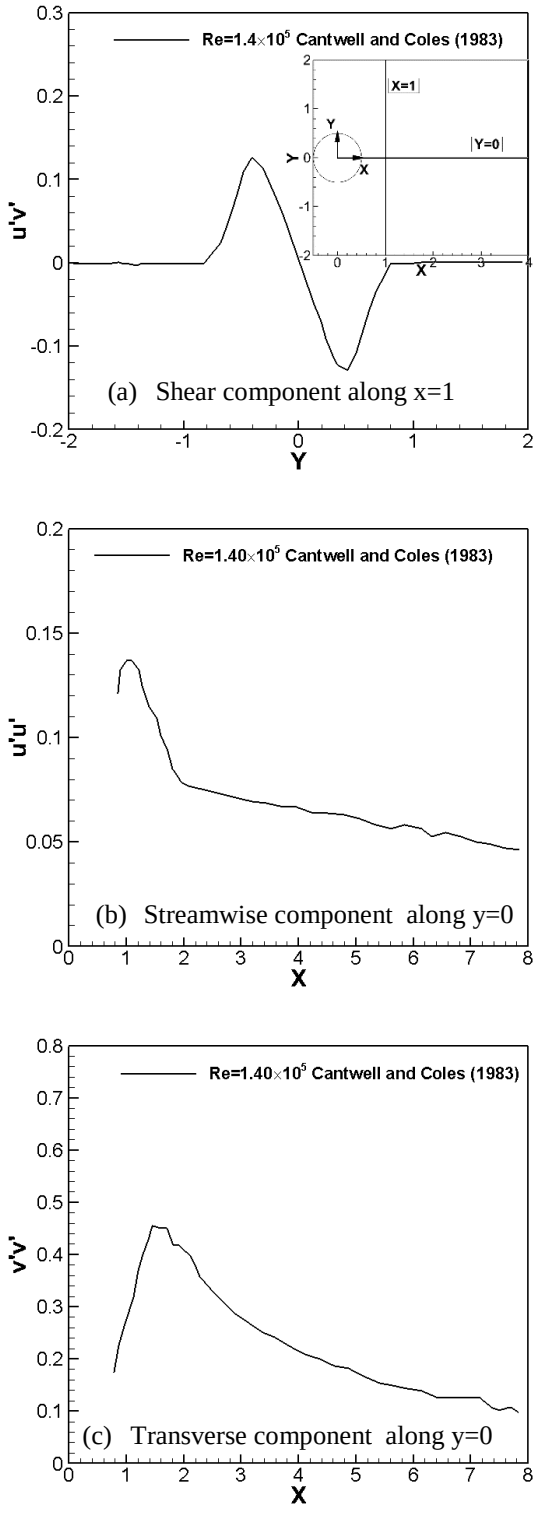

Figure 1.8 Reynolds stresses for sub-critical Re(Re=1.4x10^5) (EFD)

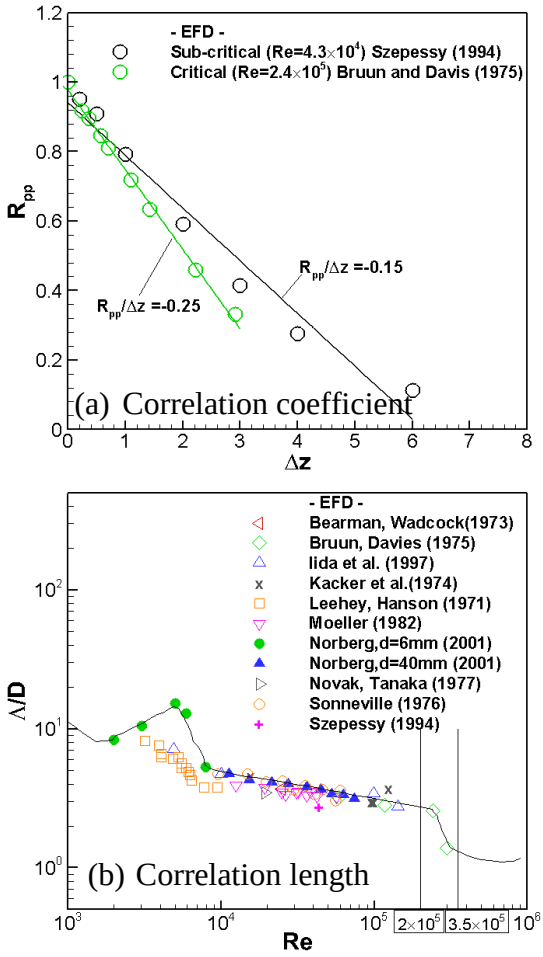

Figure 1.9 Correlation coefficient (a) and correlation length (b) (EFD)

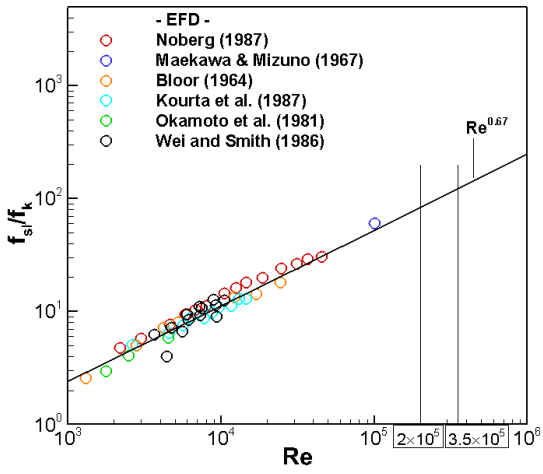

Figure 1.10 Normalized shear layer frequency (EFD)

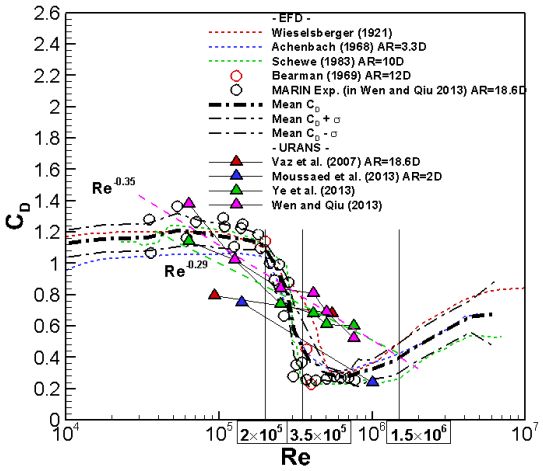

(a) C_D

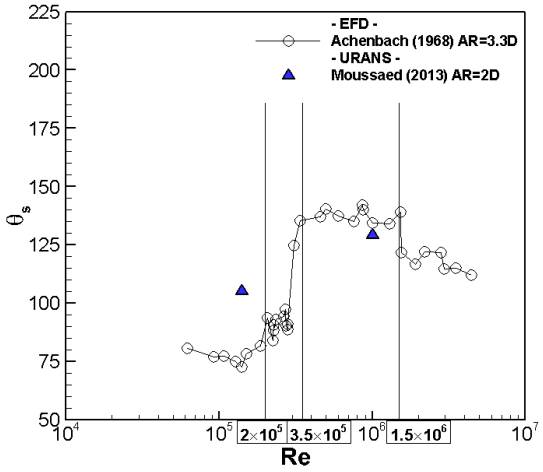

(b) θ_s

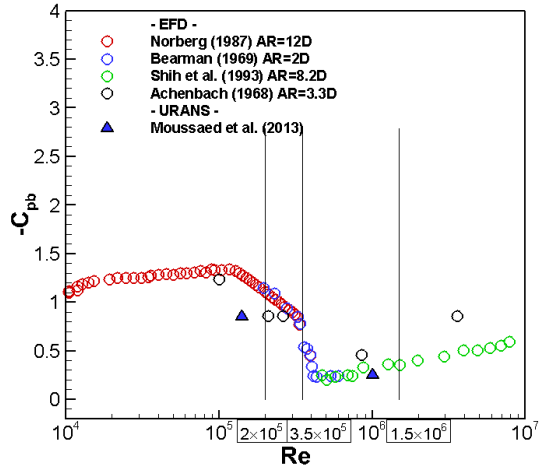

(c) $-C_{pb}$

Figure 1.11 Drag, separation angle and base pressure vs. Re (URANS)

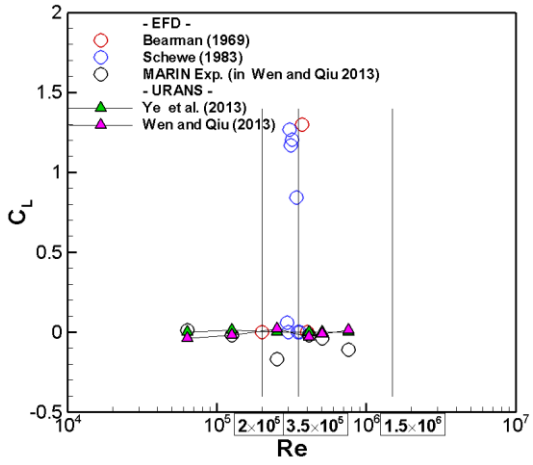

(a) Mean C_L

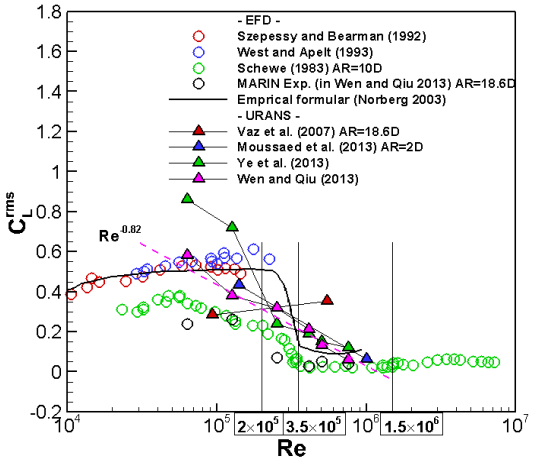

(b) C_L^{rms}

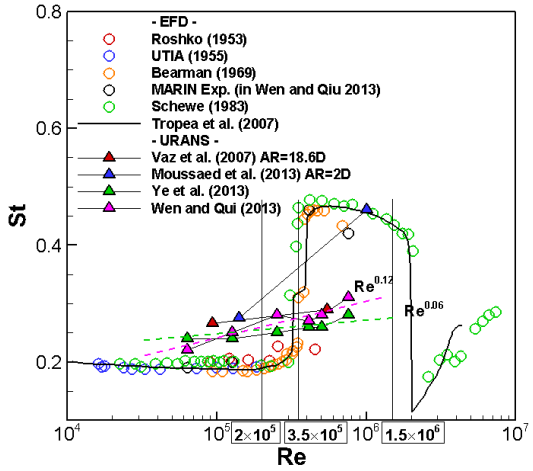

(c) St

Figure 1.12 RMS lift coefficient and Strouhal number vs. Re (URANS)

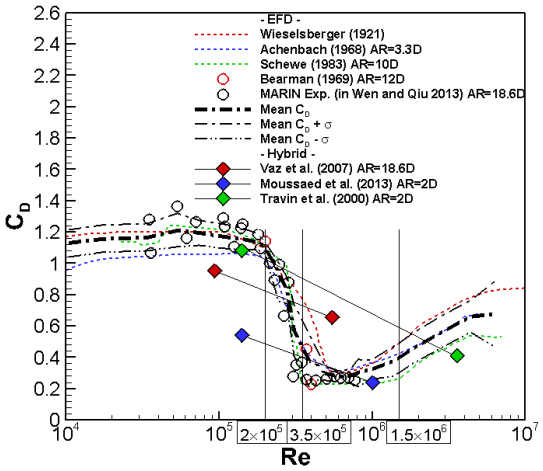

(a) C_D

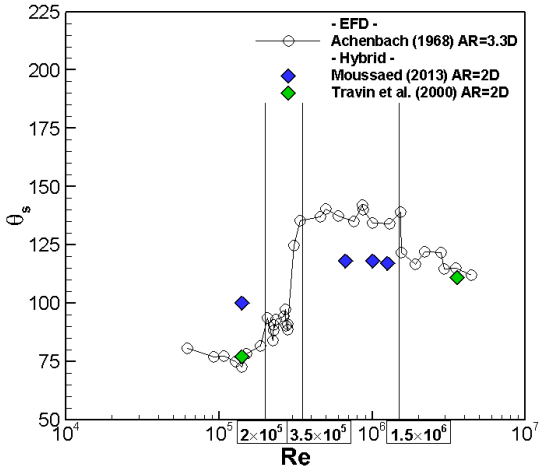

(b) θ_s

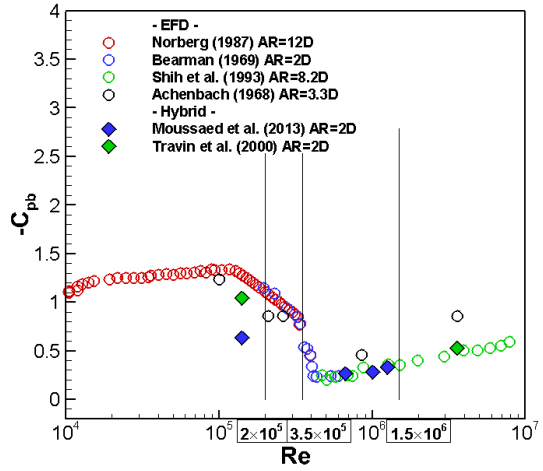

(c) $-C_{pb}$

Figure 1.13 Drag, separation angle and base pressure vs. Re (Hybrid)

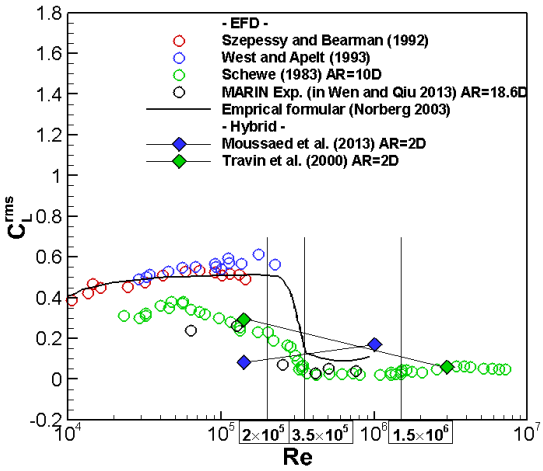

(a) C_L^{rms}

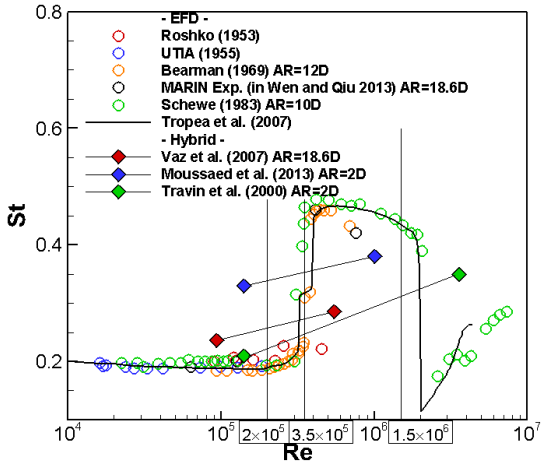

(b) St

Figure 1.14 RMS lift coefficient and Strouhal number vs. Re (Hybrid)

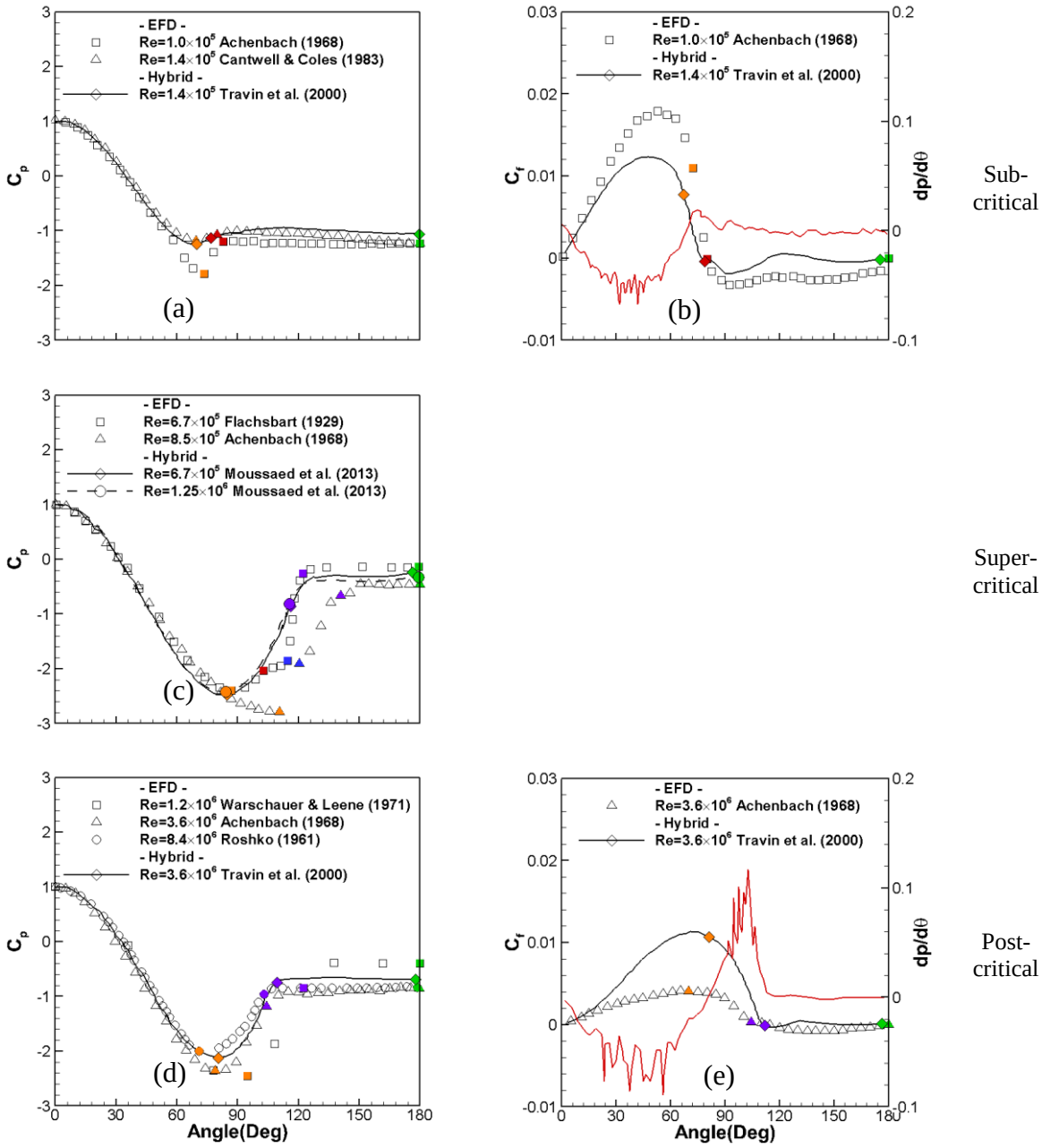

Figure 1.15 Pressure (left) and skin-friction (right) (Hybrid); orange=MP, red=LS, blue=TR, purple=TS and green=BP. Solid red line overlaid on the skin-friction are angular pressure gradient.

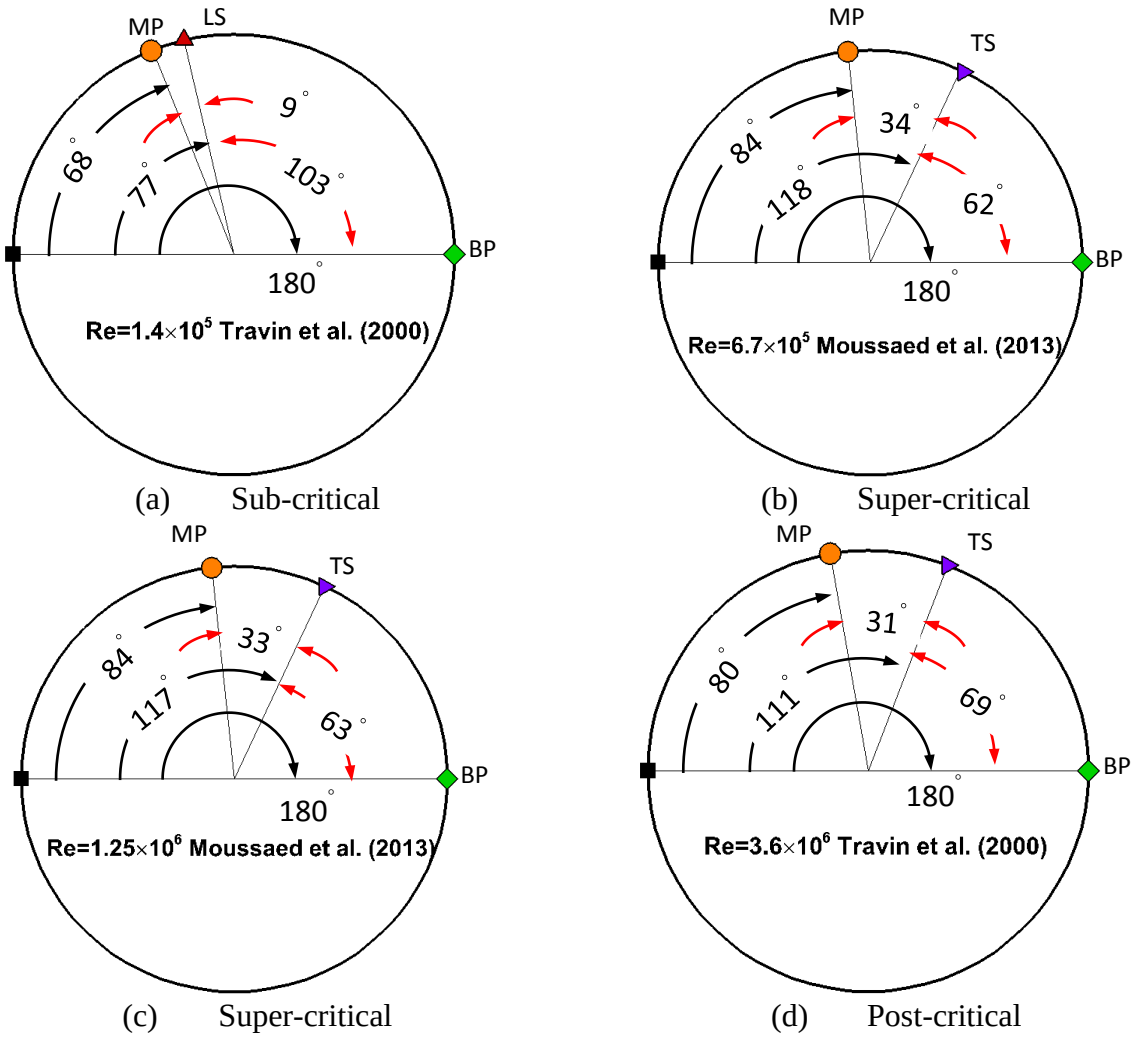

Figure 1.16 MP, LS, TR, TS and BP points on the cylinder (Hybrid); ●=MP, ▲=LS, ▼=TR, ▶ =TS and ◆=BP.

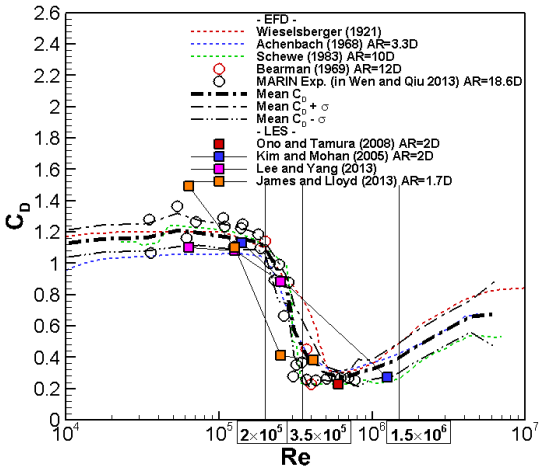

(a) C_D

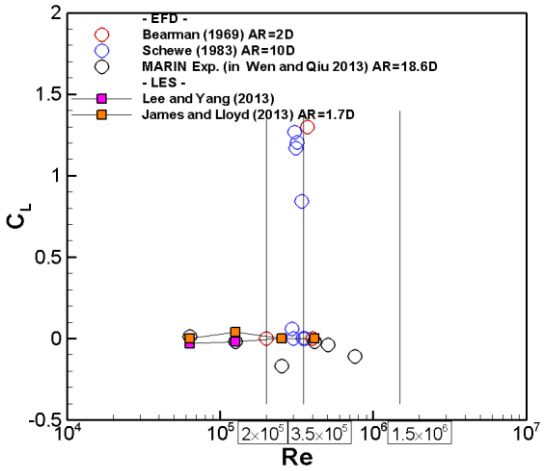

(a) Mean C_L

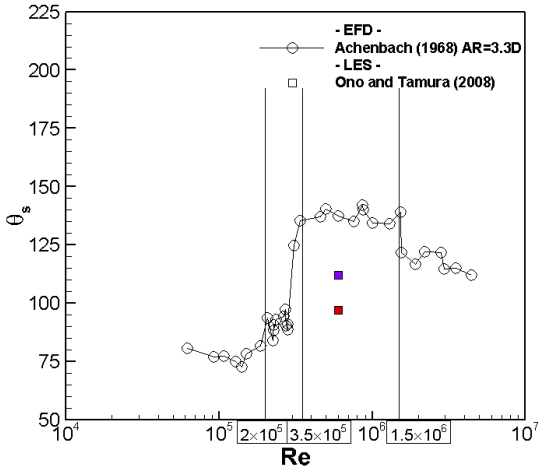

(b) θ_s

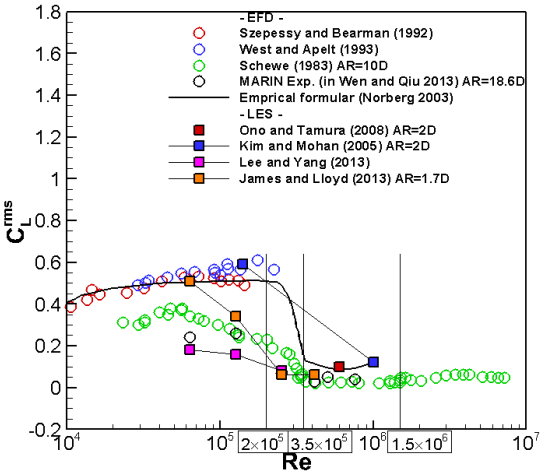

(b) C_L^{rms}

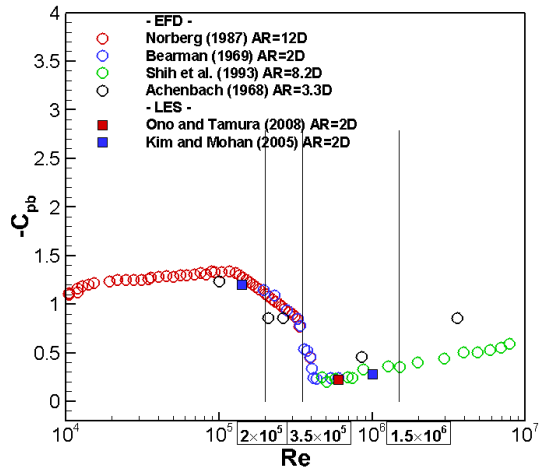

(c) $-C_{pb}$

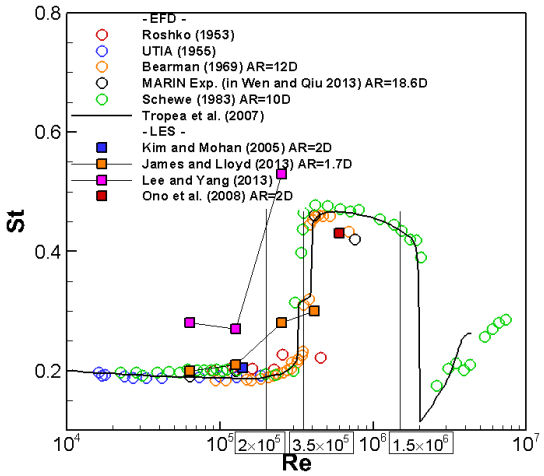

(c) St

Figure 1.17 Drag, separation angle and base pressure vs. Re (LES)

Figure 1.18 RMS lift coefficient and Strouhal number vs. Re (LES)

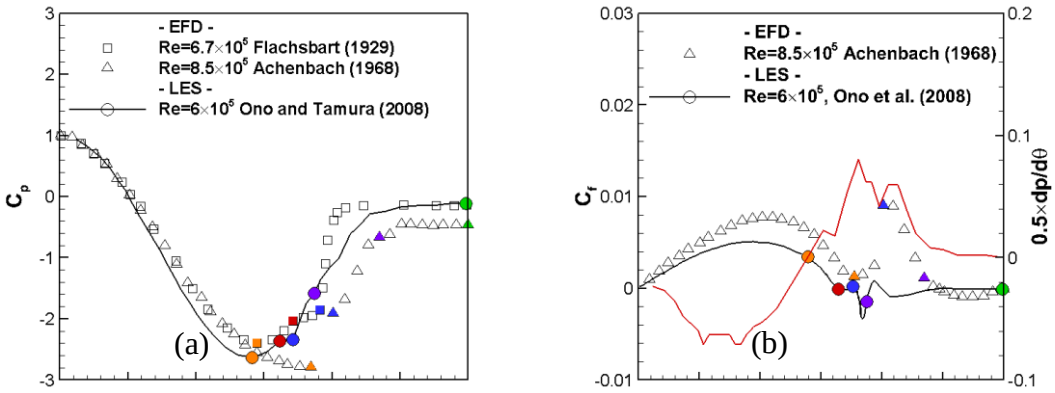

Super-critical

Figure 1.19 Pressure (left) and skin-friction (right) (LES); orange=MP, red=LS, blue=TR, purple=TS and green=BP. Solid red line overlaid on the skin-friction are angular pressure gradient.

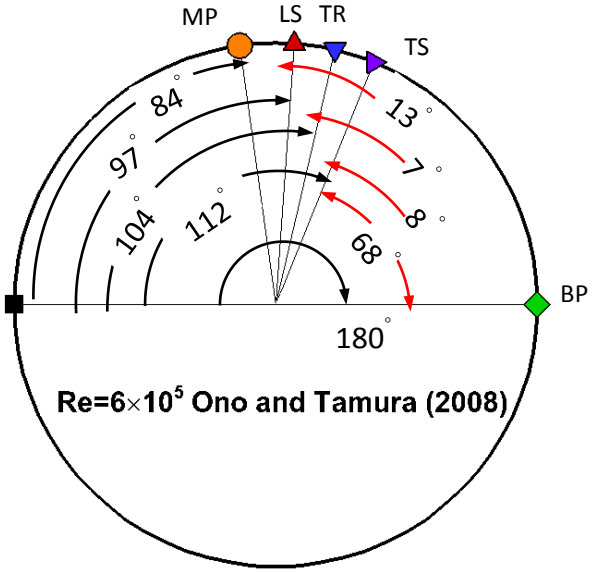

Figure 1.20 MP, LS, TR, TS and BP points on the cylinder (LES); ●=MP, ▲=LS, ▼=TR, ▶ =TS and ◆=BP.

CHAPTER 2

COMPUTATIONAL METHODS

In the present study, an orthogonal curvilinear grid flow solver, CFDShip-Iowa V6.2 (Yang and Stern, 2009; Suh et al., 2011; Wang et al. 2012), is used for the LES study of the single-phase flow simulation.

2.1 Mathematical Model

2.1.1 Navier-Stokes equations

The incompressible viscous flows are governed by the Navier-Stokes equations:

$$\frac{\partial \mathbf{u}}{\partial t} + \mathbf{u} \cdot \nabla \mathbf{u} = \frac{1}{\rho} \nabla \cdot (-p\mathbf{I} + \mathbf{T}), \tag{1}$$

$$\nabla \cdot \mathbf{u} = 0, \tag{2}$$

where t is the time, $\mathbf{u}$ is the velocity vector, ρ is the density, p is the pressure, $\mathbf{I}$ is the unit tensor, $\mathbf{T}$ is the viscous stress tensor defined with the strain rate tensor $\mathbf{S}$:

$$\mathbf{T} = 2\mu\mathbf{S}, \tag{3}$$

$$\mathbf{S} = \frac{1}{2}[\nabla \mathbf{u} + (\nabla \mathbf{u})^{T}], \tag{4}$$

where μ is for the dynamic viscosity and superscript T for transpose operation.

2.1.2 LES Turbulence model

In the LES approach, the Navier-Stokes equations are spatially filtered so that the large, energy carrying eddies are resolved and the small-scale, dissipative eddies are modeled by a SGS model.

The filtered equations are obtained after applying filtering operation to Eq. (1) and (2):

$$\frac{\partial \bar{\mathbf{u}}}{\partial t} + \bar{\mathbf{u}} \cdot \nabla \bar{\mathbf{u}} = -\frac{1}{\rho} \nabla \bar{p} + \frac{1}{\rho} \nabla \cdot [\mu (\nabla \bar{\mathbf{u}} + (\nabla \bar{\mathbf{u}})^{T})] - \nabla \cdot \bar{\boldsymbol{\tau}}, \tag{5}$$

$$\nabla \cdot \bar{\mathbf{u}} = 0, \tag{6}$$

where the bar on a variable $\bar{}$ denotes the filtered variable and $\bar{\boldsymbol{\tau}} = \overline{\mathbf{u}\mathbf{u}} - \bar{\mathbf{u}}\bar{\mathbf{u}}$ is SGS stress tensor.

Deviatoric stress of the SGS stress tensor is modeled by the Smagorinsky procedure:

$$\bar{\boldsymbol{\tau}} - \frac{1}{3}\mathrm{trace}(\bar{\boldsymbol{\tau}})\mathbf{I} = -2\nu_t \bar{\mathbf{S}}, \tag{7}$$

The turbulent eddy viscosity is defined as (Smagorinsky, 1963; Lilly, 1967):

$$\nu_t = C\Delta^2|\bar{\mathbf{S}}| \text{ and } |\bar{\mathbf{S}}| = \sqrt{2S_{ij}S_{ij}}\,. \tag{8}$$

$$\bar{\mathbf{S}} = \frac{1}{2}[\nabla\bar{\mathbf{u}} + (\nabla\bar{\mathbf{u}})^T] \tag{9}$$

where Δ is a filter length. The coefficient C in the eddy viscosity definition should be determined to close the equations.

Hence, Eq. (5) can be rewritten as the following form:

$$\frac{\partial\bar{\mathbf{u}}}{\partial t} + \bar{\mathbf{u}}\cdot\nabla\bar{\mathbf{u}} = -\frac{1}{\rho}\nabla\bar{p} + \frac{1}{\rho}\nabla\cdot[\mu\,(\nabla\bar{\mathbf{u}} + (\nabla\bar{\mathbf{u}})^T)] + \nabla\cdot[\nu_t\,(\nabla\bar{\mathbf{u}} + (\nabla\bar{\mathbf{u}})^T)], \tag{10}$$

where the trace of SGS stress tensor $\frac{1}{3}\mathrm{trace}(\bar{\boldsymbol{\tau}})$ or SGS turbulent kinetic energy k_{sgs} in Eq. (7) is incorporated into $\bar{p}$:

$$\bar{p} = \bar{p} + \frac{2}{3}k_{sgs}\,. \tag{11}$$

2.2 Numerical Methods

2.2.1 Navier-Stokes solver

A finite difference method is used to discretize the governing equations on a general orthogonal curvilinear grid. A staggered variable arrangement is adopted. For instance, contravariant velocity components u_1, u_2, u_3 are defined at cell faces in the ξ_1, ξ_2, ξ_3 directions, respectively. All other variables including pressure, density and turbulent eddy viscosity are defined at cell centers.

The continuity equation in orthogonal curvilinear coordinate system is written as the following form:

$$\nabla\cdot\mathbf{u} = \frac{\partial}{\partial\xi_1}(h_2h_3u_1) + \frac{\partial}{\partial\xi_2}(h_1h_3u_2) + \frac{\partial}{\partial\xi_3}(h_1h_2u_3) = 0 \tag{12}$$

where u_i is the contravariant velocity in the orthogonal coordinate (ξ_1, ξ_2, ξ_3) and $h_i = \partial x_i/\partial\xi_i$ is scale factor and x_i represents a Cartesian coordiante.

The Momentum equations in the orthogonal coordinate system for Eq. (10) are rewritten as the following form:

$$\frac{\partial u_1}{\partial t}+\frac{1}{J}\frac{\partial}{\partial \xi_1}\left[\frac{J}{h_1}\left(u_1u_1-\tau_{11}\right)\right]+\frac{1}{J}\frac{\partial}{\partial \xi_2}\left[\frac{J}{h_2}\left(u_1u_2-\tau_{12}\right)\right]+\frac{1}{J}\frac{\partial}{\partial \xi_3}\left[\frac{J}{h_3}\left(u_1u_3-\tau_{13}\right)\right]$$
$$=-\frac{1}{\rho}\frac{1}{h_1}\frac{\partial p}{\partial \xi_1}+\frac{1}{h_1h_2}\frac{\partial h_2}{\partial \xi_1}\left[u_2u_2-\tau_{22}\right]+\frac{1}{h_1h_3}\frac{\partial h_3}{\partial \xi_1}\left[u_3u_3-\tau_{33}\right] \quad (13)$$
$$-\frac{1}{h_1h_2}\frac{\partial h_1}{\partial \xi_2}\left[u_1u_2-\tau_{12}\right]-\frac{1}{h_1h_3}\frac{\partial h_1}{\partial \xi_3}\left[u_1u_3-\tau_{13}\right]$$

$$\frac{\partial u_2}{\partial t}+\frac{1}{J}\frac{\partial}{\partial \xi_1}\left[\frac{J}{h_1}\left(u_1u_2-\tau_{12}\right)\right]+\frac{1}{J}\frac{\partial}{\partial \xi_2}\left[\frac{J}{h_2}\left(u_2u_2-\tau_{22}\right)\right]+\frac{1}{J}\frac{\partial}{\partial \xi_3}\left[\frac{J}{h_3}\left(u_2u_3-\tau_{23}\right)\right]$$
$$=-\frac{1}{\rho}\frac{1}{h_2}\frac{\partial p}{\partial \xi_2}+\frac{1}{h_1h_2}\frac{\partial h_1}{\partial \xi_2}\left[u_1u_1-\tau_{11}\right]+\frac{1}{h_2h_3}\frac{\partial h_3}{\partial \xi_2}\left[u_3u_3-\tau_{33}\right] \quad (14)$$
$$-\frac{1}{h_2h_1}\frac{\partial h_2}{\partial \xi_1}\left[u_1u_2-\tau_{12}\right]-\frac{1}{h_2h_3}\frac{\partial h_2}{\partial \xi_3}\left[u_2u_3-\tau_{23}\right]$$

$$\frac{\partial u_3}{\partial t}+\frac{1}{J}\frac{\partial}{\partial \xi_1}\left[\frac{J}{h_1}\left(u_1u_3-\tau_{13}\right)\right]+\frac{1}{J}\frac{\partial}{\partial \xi_2}\left[\frac{J}{h_2}\left(u_2u_3-\tau_{23}\right)\right]+\frac{1}{J}\frac{\partial}{\partial \xi_3}\left[\frac{J}{h_3}\left(u_3u_3-\tau_{33}\right)\right]$$
$$=-\frac{1}{\rho}\frac{1}{h_3}\frac{\partial p}{\partial \xi_3}+\frac{1}{h_1h_3}\frac{\partial h_1}{\partial \xi_3}\left[u_1u_1-\tau_{11}\right]+\frac{1}{h_2h_3}\frac{\partial h_2}{\partial \xi_3}\left[u_2u_2-\tau_{22}\right] \quad (15)$$
$$-\frac{1}{h_3h_1}\frac{\partial h_3}{\partial \xi_1}\left[u_1u_3-\tau_{13}\right]-\frac{1}{h_2h_3}\frac{\partial h_3}{\partial \xi_2}\left[u_2u_3-\tau_{23}\right]$$

where $J=h_1h_2h_3$.

The shear stress components are rewritten as the following form:

$$\tau_{11}=2(\mu+\nu_t\rho)\left[\frac{1}{h_1}\frac{\partial u_1}{\partial \xi_1}+u_2\frac{1}{h_1h_2}\frac{\partial h_1}{\partial \xi_2}+u_3\frac{1}{h_1h_3}\frac{\partial h_1}{\partial \xi_3}\right] \quad (16)$$

$$\tau_{22}=2(\mu+\nu_t\rho)\left[\frac{1}{h_2}\frac{\partial u_2}{\partial \xi_2}+u_1\frac{1}{h_1h_2}\frac{\partial h_2}{\partial \xi_1}+u_3\frac{1}{h_2h_3}\frac{\partial h_2}{\partial \xi_3}\right] \quad (17)$$

$$\tau_{33}=2(\mu+\nu_t\rho)\left[\frac{1}{h_3}\frac{\partial u_3}{\partial \xi_3}+u_1\frac{1}{h_1h_3}\frac{\partial h_3}{\partial \xi_1}+u_2\frac{1}{h_2h_3}\frac{\partial h_3}{\partial \xi_2}\right] \quad (18)$$

$$\tau_{12}=(\mu+\nu_t\rho)\left[\frac{1}{h_2}\frac{\partial u_1}{\partial \xi_2}+\frac{1}{h_1}\frac{\partial u_2}{\partial \xi_1}-u_1\frac{1}{h_1h_2}\frac{\partial h_1}{\partial \xi_2}-u_2\frac{1}{h_1h_2}\frac{\partial h_2}{\partial \xi_1}\right] \quad (19)$$

$$\tau_{13}=(\mu+\nu_t\rho)\left[\frac{1}{h_3}\frac{\partial u_1}{\partial \xi_3}+\frac{1}{h_1}\frac{\partial u_3}{\partial \xi_1}-u_1\frac{1}{h_1h_3}\frac{\partial h_1}{\partial \xi_3}-u_3\frac{1}{h_1h_3}\frac{\partial h_3}{\partial \xi_1}\right] \quad (20)$$

$$\tau_{23}=(\mu+\nu_t\rho)\left[\frac{1}{h_2}\frac{\partial u_3}{\partial \xi_2}+\frac{1}{h_3}\frac{\partial u_2}{\partial \xi_3}-u_3\frac{1}{h_2h_3}\frac{\partial h_3}{\partial \xi_2}-u_2\frac{1}{h_2h_3}\frac{\partial h_2}{\partial \xi_3}\right] \quad (21)$$

In the present study, The orthogonal curvilinear grid reduces into a cylindrical coordinate with $(\xi_1,\xi_2,\xi_3)=(z,r,\theta)$ and the scale factor, $h_1=1$, $h_2=1$ and $h_3=r$. As a result, Eqs. (13) - (15) are simplified as the following form:

$$\frac{\partial u_z}{\partial t}+\left(u_r\frac{\partial u_z}{\partial r}+\frac{u_\theta}{r}\frac{\partial u_z}{\partial \theta}+u_z\frac{\partial u_z}{\partial z}\right)=-\frac{1}{\rho}\frac{\partial p}{\partial z}+\left(\frac{\partial}{\partial z}(\tau_{zz})+\frac{1}{r}\frac{\partial}{\partial r}(r\,\tau_{zr})+\frac{1}{r}\frac{\partial}{\partial \theta}\left(\tau_{z\theta}\right)\right) \quad (22)$$

$$\frac{\partial u_r}{\partial t}+\left(u_r\frac{\partial u_r}{\partial r}+\frac{u_\theta}{r}\frac{\partial u_r}{\partial \theta}+u_z\frac{\partial u_r}{\partial z}\right) \tag{23}$$
$$=-\frac{1}{\rho}\frac{\partial p}{\partial r}+\left(\frac{\partial}{\partial z}(\tau_{zr})+\frac{1}{r}\frac{\partial}{\partial r}(r\tau_{rr})+\frac{1}{r}\frac{\partial}{\partial \theta}(\tau_{r\theta})-\frac{\tau_{\theta\theta}}{r}\right)+\frac{u_\theta^2}{r}$$

$$\frac{\partial u_\theta}{\partial t}+\left(u_r\frac{\partial u_\theta}{\partial r}+\frac{u_\theta}{r}\frac{\partial u_\theta}{\partial \theta}+u_z\frac{\partial u_\theta}{\partial z}\right) \tag{24}$$
$$=-\frac{1}{\rho r}\frac{\partial p}{\partial \theta}+\left(\frac{\partial}{\partial z}(\tau_{z\theta})+\frac{1}{r}\frac{\partial}{\partial r}(r\tau_{r\theta})+\frac{1}{r}\frac{\partial}{\partial \theta}(\tau_{\theta\theta})+\frac{\tau_{r\theta}}{r}\right)-\frac{u_r u_\theta}{r}$$

where

$$\tau_{zz}=2(\nu+\nu_t)\frac{\partial u_z}{\partial z} \qquad \tau_{rr}=2(\nu+\nu_t)\frac{\partial u_r}{\partial r} \tag{25}$$

$$\tau_{\theta\theta}=2(\nu+\nu_t)\left(\frac{1}{r}\frac{\partial u_\theta}{\partial \theta}+\frac{u_r}{r}\right) \qquad \tau_{zr}=(\nu+\nu_t)\left(\frac{\partial u_z}{\partial r}+\frac{\partial u_r}{\partial z}\right) \tag{26}$$

$$\tau_{z\theta}=(\nu+\nu_t)\left(\frac{\partial u_\theta}{\partial z}+\frac{1}{r}\frac{\partial u_z}{\partial \theta}\right) \qquad \tau_{r\theta}=(\nu+\nu_t)\left(\frac{1}{r}\frac{\partial u_r}{\partial \theta}+\frac{\partial u_\theta}{\partial r}-\frac{u_\theta}{r}\right) \tag{27}$$

2.2.2 Fractional step method

A four-step fractional-step method is employed for velocity-pressure coupling where a pressure Poisson equation is solved to enforce the continuity equation as the following form:

1. Predictor:

$$\frac{\hat{u}_i-u_i^n}{\Delta t}=\frac{1}{2}\left(3A_i^n-A_i^{n-1}\right)+\frac{1}{2}\left(C_i^{n+1}+C_i^n\right)-\mathrm{Grad}_i(p^n) \tag{28}$$

where superscript $n+1$ is corresponding to the intermediate time level of $\hat{u}_i$. A semi-implicit time-advancement scheme is adopted to integrate the momentum equations with the second-order Crank-Nicolson scheme for the diagonal viscous terms and the second-order Adams-Bashforth scheme for the convective terms and other viscous terms as in the following form:

$$\mathbf{A}=-\mathbf{u}\cdot\nabla\mathbf{u}+\frac{1}{\rho}\nabla\cdot[\mu(\nabla\mathbf{u})^T]+\nabla\cdot[\nu_t(\nabla\mathbf{u})^T] \tag{29}$$

$$\mathbf{C}=\frac{1}{\rho}\nabla\cdot[\mu(\nabla\mathbf{u})]+\nabla\cdot[\nu_t(\nabla\mathbf{u})] \tag{30}$$

where A and C denote terms treated by the Adams-Bashforth and Crank-Nicolson schemes, respectively.

2. First Corrector:

$$\frac{u_i^*-\hat{u}_i}{\Delta t}=\mathrm{Grad}_i(p^n) \tag{31}$$

3. Pressure Poisson Equation:

$$\frac{\partial}{\partial x_i}\,\mathrm{Grad}_i(p^{n+1}) = \frac{1}{\Delta t}\frac{\partial u_i^*}{\partial x_i} \tag{32}$$

4. Second Corrector:

$$\frac{u_i^{n+1} - u_i^*}{\Delta t} = -\mathrm{Grad}_i(p^{n+1}) \tag{33}$$

where superscript n denotes time step, subscript $i = 1, 2, 3$ represents coordinate component, $\hat{u}_i$ and u_i^* are the first and second intermediate velocities, respectively. $\mathrm{Grad}_i(p)$ is a pressure gradient term defined at the center of the cell faces (collocated with velocity components).

2.2.3 Spatial discretization

A third-order Quadratic Upstream Interpolation for Convective Kinematics (QUICK) and a fifth-order Weighted-ENO (WENO) scheme are used for the approximation of the convective terms in divergence form (conservative form) $\nabla \cdot (\mathbf{u}\phi)$.

For instance, streamwise direction component is discretized as the following form:

$$\left.\frac{du\phi}{dx}\right|_i \approx \frac{1}{\Delta x}\left(u_{i+\frac{1}{2}}\phi|_{i+\frac{1}{2}} - u|_{i-\frac{1}{2}}\phi|_{i-\frac{1}{2}}\right) \tag{34}$$

where u is advecting velocity component and ϕ represents a flow variable and $|_{i+1/2}$ and $|_{i-1/2}$ represent values evaluated on the right and left cell faces, respectively. A central difference scheme (CDS) is used for other terms.

(1) <u>QUICK implementation (Leonard, 1979)</u>

Given a uniform three-point stencil, third-order polynomial interpolation is performed for the evaluation of the flow variable ϕ on a cell face as in the following form:

$$\phi_{i+\frac{1}{2}} = \begin{cases} \frac{1}{8}(-\phi_{i-1} + 6\phi_i + 3\phi_{i+1}) & \text{, if } u_{i+\frac{1}{2}} \geq 0, \\ \frac{1}{8}(-\phi_{i+2} + 6\phi_{i+1} + 3\phi_i) & \text{if } u_{i+\frac{1}{2}} < 0 \end{cases} \tag{35}$$

on a uniform grid.

(2) Fifth-order WENO implementation (Jiang and Shu 1996)

Typically, artificial compressibility is introduced to the scheme when extending the schemes developed for compressible flows such as WENO to incompressible flows (Chen et al., 1999). In the present study, upwind approach is adopted as in applying ENO to the incompressible Navier-Stokes equation (Shu 1993).

Given a uniform five-point stencil following the ENO approach, there are three candidate stencils that can be used to construct an essentially non-oscillatory third-order polynomial interpolation of a flow variable ϕ on a cell face as in the following form:

$$\phi_{i+\frac{1}{2}} = \sum_{k=1}^{3} \omega_k \phi^k_{i+\frac{1}{2}}$$
$$\omega_k = \frac{\widetilde{\omega}_k}{\sum_{l=1}^{3} \widetilde{\omega_l}}, \qquad \widetilde{\omega}_l = \frac{\gamma_l}{(\varepsilon + \beta_l)^2} \tag{36}$$

where ω_k is a nonlinear weight and γ_l is linear weight to ensure a high-order solution in smooth regions of flow and β_l is smoothness indicators. ε is a small constant to prevent the denominator from approaching to zero, e.g. 10^{-6}.

The interpolated flow variable with advecting velocity $u_{i+1/2} \geq 0$ is determined as in the following form:

$$\phi_{i+\frac{1}{2}} = \omega_1 \phi^1_{i+\frac{1}{2}} + \omega_2 \phi^2_{i+\frac{1}{2}} + \omega_3 \phi^3_{i+\frac{1}{2}}$$
$$\phi^1_{i+\frac{1}{2}} = \frac{1}{3}\phi_i + \frac{5}{6}\phi_{i+1} - \frac{1}{6}\phi_{i+2}$$
$$\phi^2_{i+\frac{1}{2}} = -\frac{1}{6}\phi_{i-1} + \frac{5}{6}\phi_i + \frac{1}{3}\phi_{i+1}$$
$$\phi^3_{i+\frac{1}{2}} = \frac{1}{3}\phi_{i-2} - \frac{7}{6}\phi_{i-1} + \frac{11}{6}\phi_i \tag{37}$$

with linear weights given by

$$\gamma_1 = \frac{3}{10}, \gamma_2 = \frac{3}{5}, \gamma_3 = \frac{1}{10} \tag{38}$$

and the smoothness indicators given by

$$\beta_1 = \frac{13}{12}(\phi_i - 2\phi_{i+1} + \phi_{i+2})^2 + \frac{1}{4}(3\phi_i - 4\phi_{i+1} + \phi_{i+2})^2$$
$$\beta_2 = \frac{13}{12}(\phi_{i-1} - 2\phi_i + \phi_{i+1})^2 + \frac{1}{4}(\phi_{i-1} - \phi_{i+1})^2$$

$$\beta_3 = \frac{13}{12}(\phi_{i-2} - 2\phi_{i-1} + \phi_i)^2 + \frac{1}{4}(\phi_{i-2} - 4\phi_{i-1} + 3\phi_i)^2. \quad (39)$$

The interpolated flow variable with advecting velocity $u_{i+1/2} < 0$ is determined as in the following form:

$$\begin{aligned}
\phi_{i+\frac{1}{2}} &= \omega_1\phi^1_{i+\frac{1}{2}} + \omega_2\phi^2_{i+\frac{1}{2}} + \omega_3\phi^3_{i+\frac{1}{2}} \\
\phi^1_{i+\frac{1}{2}} &= \frac{11}{6}\phi_{i+1} - \frac{7}{6}\phi_{i+2} + \frac{1}{3}\phi_{i+3} \\
\phi^2_{i+\frac{1}{2}} &= \frac{1}{3}\phi_i + \frac{5}{6}\phi_{i+1} - \frac{1}{6}\phi_{i+2} \\
\phi^3_{i+\frac{1}{2}} &= -\frac{1}{6}\phi_{i-1} + \frac{5}{6}\phi_i + \frac{1}{3}\phi_{i+1}
\end{aligned} \quad (40)$$

with linear weights given by

$$\gamma_1 = \frac{1}{10}, \gamma_2 = \frac{3}{5}, \gamma_3 = \frac{3}{10} \quad (41)$$

and the smoothness indicators given by

$$\begin{aligned}
\beta_1 &= \frac{13}{12}(\phi_{i+1} - 2\phi_{i+2} + \phi_{i+3})^2 + \frac{1}{4}(3\phi_{i+1} - 4\phi_{i+2} + \phi_{i+3})^2 \\
\beta_2 &= \frac{13}{12}(\phi_i - 2\phi_{i+1} + \phi_{i+2})^2 + \frac{1}{4}(\phi_i - \phi_{i+2})^2 \\
\beta_3 &= \frac{13}{12}(\phi_{i-1} - 2\phi_i + \phi_{i+1})^2 + \frac{1}{4}(\phi_{i-1} - 4\phi_i + 3\phi_{i+1})^2.
\end{aligned} \quad (42)$$

(3) <u>WENO in non-conservative form</u>

The interpolation of flow variable ϕ mentioned above is applied to the convection term in advective form (non-conservative form) $\mathbf{u} \cdot \nabla\phi$.

For instance, the streamwise component is discretized as the following form:

$$u\frac{d\phi}{dx}\Big|_i \approx \frac{1}{\Delta x}\, u_i \left(\phi|_{i+\frac{1}{2}} - \phi|_{i-\frac{1}{2}}\right) \quad (43)$$

where the upwind approach is applied to the sign of u_i.

2.2.4 Direct Poisson equation solver

Poisson equation in a cylindrical coordinate is expressed as the following form:

$$\nabla^2\phi = \frac{1}{r}\frac{\partial}{\partial r}\left(r\frac{\partial}{\partial r} + \frac{1}{r^2}\frac{\partial^2}{\partial\theta^2} + \frac{\partial^2}{\partial z^2}\right)\phi = f. \quad (44)$$

In discrete form

$$\frac{1}{r}\frac{\delta}{\delta r}\left(r\frac{\delta}{\delta r}+\frac{1}{r^2}\frac{\delta^2}{\delta^2\theta}+\frac{\delta^2}{\delta^2 z}\right)\phi_{i,j,k}=f_{i,j,k}\,. \tag{45}$$

If grid is uniform and periodic boundary conditions are applied in the spanwise and azimuthal directions, discrete Fourier transform can be applied to Eq. (45).

The second derivatives in the spanwise and azimuthal directions are approximated as the following form:

$$\left.\frac{\delta^2\phi}{\delta x^2}\right|_j \approx \frac{1}{\Delta x^2}\left[\phi_{j+1}-2\phi_j+\phi_{j-1}\right]=\sum_{l=-\frac{N}{2}}^{\frac{N}{2}-1}-\widehat{\phi}_l k' e^{ikx_j} \tag{46}$$

where the hat symbol on the variable $\widehat{\ }$ is the variable in spectral space, k' is modified wave number $k'=\frac{2}{\Delta x^2}\left[1-\cos\left(\frac{2\pi l}{N}\right)\right]$, k is wave number $k=l\frac{2\pi}{N}$, x_j is discretized point $x_j=\frac{L}{N}j$, L is length of domain and N is the size of the domain.

Thus, partial differential equation of Eq. (45) is reduced to ordinary differential equation as the following form:

$$\left[\frac{1}{r}\frac{\delta}{\delta r}\left(r\frac{\delta}{\delta r}\right)+\frac{1}{r^2}k_l'+k_m'\right]\widehat{\phi}_{i,l,m}\Big|^p=\hat{f}_{i,l,m}\Big|^p \tag{47}$$

where super script p means that the evaluation is carried out at the cell center.

The central difference scheme is applied to the radial direction and rewritten as the following form:

$$am_i\,\widehat{\phi}_{i-1,l,m}+\left(bm_i-\frac{k_l'}{r_p\big|_i^2}-k_m'\right)\widehat{\phi}_{i,l,m}+cm_i\widehat{\phi}_{i+1,l,m}=\hat{f}_{i,l,m} \tag{48}$$

where coefficients are

$$am_i=\frac{1}{\Delta\xi^2}\frac{1}{r_p\big|_i}r_u\big|_{i-1}\,\xi_r\big|_i^p\xi_r\big|_{i-1}^u \tag{49}$$

$$cm_i=\frac{1}{\Delta\xi^2}\frac{1}{r_p\big|_i}r_u\big|_i\,\xi_r\big|_i^p\xi_r\big|_i^u \tag{50}$$

$$bm_i=-am_i-cm_i \tag{51}$$

where r_p is radius at a cell center and r_u is radius at a cell face and $\xi_r=\delta\xi/\delta r$. Since Eq. (48) forms a tridiagonal matrix, the Thomas algorithm is used to inverse the matrix.

2.2.5 LES model implementation

The model coefficient C in the eddy viscosity definition in Eq. (8) should be given to solve the closure problem arised in Eq. (5). It has been identified that the model parameter C should have different values for different flow configurations such as inhomogeneous turbulent flow and local region including near wall. Thus, the parameter should be dynamically calculated as the simulation goes. In the presetn study, the Lagrangian dynamic Subgrid-scale (SGS) model (Meneveau et al., 1996) is adopted to handle complex geometries without the requirement of homogeneous directions.

In dynamic approach, two filter width, $\widehat{\Delta}$ and $\overline{\Delta}$ are used where $\widehat{\Delta} = \alpha\overline{\Delta}$ is for test filter width and $\overline{\Delta}$ is for grid filter width while $\widehat{\Delta} > \overline{\Delta}$. Applying the test filter $\widehat{G}$ to the filtered equation Eq. (5) yields the subtest scale T_{ij} in the similar form to the SGS stresses τ_{ij} as the following form:

$$\tau_{ij} - \frac{\delta_{ij}}{3}\tau_{kk} = -2\upsilon_T\bar{S}_{ij} = -2C(\overline{\Delta})^2|\bar{S}|\bar{S}_{ij} \tag{52}$$

$$T_{ij} - \frac{\delta_{ij}}{3}T_{kk} = -2\hat{\upsilon}_T\hat{\bar{S}}_{ij} = -2C\left(\hat{\overline{\Delta}}\right)^2\left|\hat{\bar{S}}\right|\hat{\bar{S}}_{ij}\,. \tag{53}$$

The resolved turbulent stresses are yielded by using the Germano identity

$$L_{ij} = \widehat{\bar{u}_i\bar{u}_j} - \hat{\bar{u}}_i\hat{\bar{u}}_j = T_{ij} - \hat{\tau}_{ij} \tag{54}$$

The subtest scale stresses have the similar form to that of the SGS stresses by substituting Eq. (52) and (53) into Eq. (54) as the following form:

$$L_{ij} - \frac{\delta_{ij}}{3}L_{kk} = -2C(\alpha\overline{\Delta})^2\left|\hat{\bar{S}}\right|\hat{\bar{S}}_{ij} + 2C\widehat{(\overline{\Delta})^2|\bar{S}|\bar{S}_{ij}} \tag{55}$$

With the assumption that the coefficient C is constant over the filter width, $\alpha\overline{\Delta}$, Eq. (55) can be rewritten as the following form:

$$L_{ij} - \frac{\delta_{ij}}{3}L_{kk} = -2CM_{ij} \tag{56}$$

where $M_{ij} = \overline{\Delta}^2\left(\alpha^2\left|\hat{\bar{S}}\right|\hat{\bar{S}}_{ij} - \widehat{|\bar{S}|\bar{S}_{ij}}\right)$. With the assumption that L_{ij} is trace free, Eq. (56) is solved in a least squares method in order to minimize the error as it is indeterminate for nine equations with one unknown. The squared error e_{ij}

$$e_{ij}^2 = \left(L_{ij} + 2CM_{ij}\right)^2 = L_{ij}^2 + 4CL_{ij}M_{ij} + 4C^2M_{ij}M_{ij} \tag{57}$$

To minimize error, Eq. (57) should satisfy the following relation:

$$\frac{\partial e_{ij}^2}{\partial C} = 4L_{ij}M_{ij} + 8CM_{ij}M_{ij} = 0 \tag{58}$$

and yields the coefficient C as the following form:

$$C = -\frac{1}{2}\frac{L_{ij}M_{ij}}{M_{ij}M_{ij}} \tag{59}$$

To remove sharp fluctuations of the parameter resulting in unstable simulation, ensemble average $\langle \quad \rangle$ is introduced in both nominator and denominator as follows:

$$C = -\frac{1}{2}\frac{\langle L_{ij}M_{ij}\rangle}{\langle M_{ij}M_{ij}\rangle} \tag{60}$$

In the Lagrangian dynamic SGS model, the ensemble average $\langle\varphi\rangle$ for $\langle L_{ij}M_{ij}\rangle$ and $\langle M_{ij}M_{ij}\rangle$ is applied along the fluid particle trajectories as the following form:

$$\langle\varphi\rangle = \int_{-\infty}^{t} \varphi(t')\, W(t-t')dt' \tag{61}$$

where $W(t)$ is an exponential weighting functions chosen to give more weight to recent times.

The introduction of the exponential weighting function has the practical advantage as the ensemble average is the solution to the relaxation-transport equation

$$\frac{D\langle\varphi\rangle}{Dt} = \frac{\partial\langle\varphi\rangle}{\partial t} + \mathbf{u}\cdot\nabla\langle\varphi\rangle = \frac{1}{T}\,(\varphi - \langle\varphi\rangle) \tag{62}$$

where T is a characteristic time for motions near the grid scale.

The grid filter $\overline{G}$ is the implicit top-hat filter so that no actual grid filtering operation is needed in the implementation. The grid filter size is $\bar{\Delta} = (\Delta x\Delta y\Delta z)^{1/3}$ where Δx, Δy, Δz are the grid cell sizes in three directions, respectively. The ratio between the test filter and grid filter is

$$\alpha = \hat{\bar{\Delta}}/\bar{\Delta} = \sqrt{6} \tag{63}$$

Test-filtering operation follows the trapezoidal rule and it is applied to each direction in order as the following form:

$$\hat{\bar{u}}_{i,j,k} = \tfrac{1}{4}\bar{u}_{i-1,j,k} + \tfrac{1}{2}\bar{u}_{i,j,k} + \tfrac{1}{4}\bar{u}_{i+1,j,k} \tag{64}$$

The discretization to get the Lagrangian averaging over flow path lines $\langle\varphi\rangle$ is applied to Eq. (62) as follows:

$$\langle\varphi^n(\mathbf{x})\rangle = \varepsilon^{n-1}\varphi^n(\mathbf{x}) + (1-\varepsilon^{n-1})\langle\varphi^{n-1}\rangle(\mathbf{x}') \tag{65}$$

where superscript n means time level at t^n, $\mathbf{x}$ is the grid point location and $\mathbf{x}' = \mathbf{x} - \mathbf{u}^{\mathbf{n}}(\mathbf{x})\Delta t$ is the flow particle location at t^{n-1} with the use of the first order Lagrangian tracking method**.** The weighting function ε is defined as the following form:

$$\varepsilon^n = \frac{\Delta t/T^n}{\Delta t + \Delta t/T^n} \tag{66}$$

where the flow memory length is given by $T^n = 1.5\bar{\Delta}\left[-8\langle L_{ij}M_{ij}\rangle^n\langle M_{ij}M_{ij}\rangle^n\right]^{-1/8}$ (Sarghini et al., 1999).

2.3 Software Architecture and High Performance Computing

The simple topologic structure of orthogonal grids is favorable for coarse-grain parallelization where communication between subdomains does not occur many times. The parallelization is done via a domain decomposition technique using the MPI library. A simple domain decomposition technique is used in CFDShip-Iowa version 6 where the orthogonal grid is divided into pieces, each of which resides in one CPU core.

A parallel tri-diagonal system solver is used with the approximate factorization of momentum equations and no iterations are needed for the inversion of the momentum equations. It is crucial to reduce computational time of the Poisson equation involved in the fractional step method due to the fact that the elliptic equations such as the Poisson equation are expensive to compute. To this end, a direct Poisson equation solver for single-phase flows has been included in the code. Usually, the Poisson equation solver, if not a direct solver, takes most of the CPU time in a single time step.

Parallel I/O based on MPI 2 is implemented. Instead of the usual approaches that one process collects all data from all processes and write to one file, or, each process write its data to its own file, in the current approach all processes write its data to one single file, which is highly scalable and can greatly simplify the I/O operation and minimize the post-processing overhead.

2.4 Computational Setup

Figure 2.1 (a) and (b) show the coordinate systems and boundary conditions. The origin of the coordinates is located at the center of the circular cylinder. The streamwise, transverse and spanwise directions are set to X, Y and Z, respectively. The flows are computed in a cylindrical coordinate where radial direction r extends from the center of the cylinder, azimuthal direction θ is assigned in anti-clockwise direction starting from the downstream direction and the axis z coinsides with the spanwise direction.

The radial outer boundary is divided at $\theta = 90$ and $\theta = 270$ and left part and right part are assigned to inlet and outlet boundaries. The uniform free stream flows into the inlet boundary along the X direction. A convective outflow boundary condition is used for the outlet boundary (Breuer, 1998). No-slip boundary condition is imposed on the cylinder wall. Periodic boundary conditions are employed on the top and bottom of the cylinder.

Figure 2.2 (a) and (b) show the domain size and body-fitted grid used in the present study. The length and velocity are non-dimensionalized with the diameter of the cylinder D and the free stream velocity U_∞. The distance from the center of the cylinder to the radial outer boundary is 20D. The length of the span L varies from 2D to 8D. The points of the body-fitted grid are uniformly distributed in the spanwise and azimuthal directions. The points in the radial direction are clustred near the cylinder wall to resolve the boundary layer and flow separation.

Table 2.1 summarizes all the simulations performed for the 6 Re values required for submission to the ITTC Workshop where Re is defined in the following form:

$$\mathrm{Re} = \frac{U_\infty D}{\nu}. \tag{67}$$

where ν is kinematic viscosity. Initially, simulations were performed for AR=2 with medium grid, based on AR values used in previous simulations. The medium grid has about 67 million grid points. Subsequently additional simulations were performed to study the effects of AR, grid resolution (134 and 8 million grid points for fine and coarse grid, respectively) and convection scheme. For sub-critical Re, cases 1-7 are for $\mathrm{Re}=6.31\times10^4$ and cases 8-13 are for $\mathrm{Re}=1.26\times10^5$.

For critical Re, cases 14-19 are for Re=2.52x10^5. For super-critical Re, case 20 is for Re=4.15x10^5; cases 21-22 are for Re=5.06x10^5 and cases 23-30 are for Re=7.57x10^5. Cases 5, 12, 18, 20, 21, and 26 were submitted to the ITTC workshop. Cases 23-25 are for quantitative verification and validation. The y^+ corresponding to the first grid point is 0.67 for the coarse grid and 0.15 for the fine grid at Re=7.57x10^5. The y^+ value decreases as Re decreases and reach to 0.03 at Re=6.31x10^4. For all cases, 512 CPU cores are used for the computation. Each case takes over 2500 wall clock hours; about 1500 hours to reach statistically stationary solutions and about 1000 hours to get data covering 20 Karman vortex shedding cycles. A constant time step Δt=1x10^{-4} is used and solution files are written every 1000 time steps unless otherwise stated. The time interval between solution files is 1x10^{-1}. 50 files for sub-critical and critical Re and 30 files for super-critical Re are contained in one Karman vortex shedding cycle.

2.5 Analysis Methods

2.5.1 Verification and validation

Verification is a process for assessing the simulation numerical uncertainty U_{SN}, which is defined as $U_{SN}^2 = U_I^2 + U_T^2 + U_G^2$ where U_I is the iterative uncertainty, U_T is the time-step uncertainty, and U_G is the grid uncertainty. The methodology and procedures follows the way proposed by Stern et al. (2006) and Xing and Stern (2010). The iterative uncertainty U_I is estimated as half the range of the maximum and minimum solution, S_U and S_L:

$$U_I = \left|\frac{1}{2}(S_U - S_L)\right|. \tag{68}$$

The three solutions are obtained by using systematically refined grid with refinement ratio

$$r_G = \frac{\Delta x_2}{\Delta x_1} = \frac{\Delta x_3}{\Delta x_2} \tag{69}$$

where the subscript 3, 2, and 1 represent the coarse, medium and fine grids, respectively, Δx is grid spacing. The grid convergence ratio R_G is used to check convergence of the solution (S) on the three grids

$$R_G = \frac{\varepsilon_{12}}{\varepsilon_{23}} = \frac{S_2 - S_1}{S_3 - S_2} \tag{70}$$

where

$$\begin{aligned} 0 < R_G < 1 &\quad \text{Monotonic convergence} \\ -1 < R_G < 0 &\quad \text{Oscillatory convergence} \\ R_G \geq 1 &\quad \text{Monotonic divergence} \\ R_G \leq -1 &\quad \text{Oscillatory divergence} \end{aligned}$$

The ratio of numerical, P_{RE} and theoretical, P_{th} order of accuracy P is defined as the following form:

$$P = \frac{P_{RE}}{P_{th}} = \frac{\ln(\varepsilon_{32}/\varepsilon_{21})/\ln r_G}{P_{th}} \tag{71}$$

Ideally, the solutions are expected to be in the asymptotic range when $P = 1$.

Validation is a process for assessing the simulation modeling uncertainty by comaparing with experimental data D. The comparison error E is defined as the difference between D and the simulation S as follows:

$$E = \frac{D - S}{D} \times 100 \tag{72}$$

The validation uncertainty U_V is given by the relation as the following form:

$$U_V^2 = U_D^2 + U_{SN}^2 \tag{73}$$

where U_D is the uncertainty in the experimental data. If the absolute value of E is less than the validation uncertainty U_V, the numerical predictions are validated at U_V interval when $|E| \leq U_V$.

The verification and validation are carried out by examining the drag and lift coefficient defined as the following form:

$$C_D = \frac{\text{Drag}}{\frac{1}{2}\rho U_\infty^2 DL} \tag{74}$$

$$C_L = \frac{\text{Lift}}{\frac{1}{2}\rho U_\infty^2 DL} \tag{75}$$

where L is the span length of the cylinder and ρ density of water. The lift coefficient is highly correlated with the vortex shedding frequency represented by the Strouhal number, $St = fD/U_\infty$ where f is the vortex shedding frequency. The drag of a cylinder is composed of pressure and friction forces. The local pressure and friction coefficients acting on the circular cylinder are defined as the following form:

$$C_p = \frac{\overline{p} - p_\infty}{\frac{1}{2}\rho U_\infty^2} \tag{76}$$

$$C_f = \frac{\tau_w}{\frac{1}{2}\rho U_\infty^2} \tag{77}$$

where τ_w is the wall shear stress.

2.5.2 Quality assessment criteria for LES

It is essential to analyze whether the LES grid has sufficient grid resolution for the quality of the LES results. Several approaches were proposed to assess the quality and they fall into two categories: single-grid estimators and multi-grid estimators (Celik et al., 2005). The single-grid estimators require a single LES solution whereas the multi-grid estimators use a number of LES solutions for systematic grid study and involves the form of Richardson extrapolation. The single-grid estimators are useful compared with the multi-grid estimators when the LES computation is expensive.

A single-grid estimator denoted as IQ is one of estimators suggested by Celik et al. (2005). The estimator is derived by comparing the LES grid resolution to the Kolmogorov length scale and can be calculated as the following form:

$$IQ = \frac{1}{1 + \alpha_\nu \left(\frac{\nu_{eff}}{\nu}\right)^n} \tag{78}$$

The effective viscosity ν_{eff} is approximated as $\nu_{eff} = \nu + \nu_t + \nu_{num}$ where ν is molecular viscosity, ν_t is turbulent eddy viscosity and ν_{num} is viscosity from numerical dissipation. The magnitude of ν_{num} is assumed comparable to ν_t, i.g. $\nu_t = \nu_{num}$ and the coefficients $\alpha_\nu = 0.05$ and $n = 0.53$ are derived by studying homogeneous isotropic turbulence (Celik et al., 2005). It has been suggested that LES should resolve at least 80% of the turbulent kinetic energy (Pope, 2000). The value of IQ should be maintained above 0.8 for a good LES (Celik et al., 2005).

2.5.3 Cross correlation coefficient and correlation length

Three-dimensional effect of solutions is examined with the cross correlation coefficient of pressure (Szepessy, 1994) as the following form:

$$R_{pp} = \frac{\overline{p_i p_j}}{\sqrt{\overline{p_i^2}}\sqrt{\overline{p_j^2}}} \tag{79}$$

where subscript i is located at midspan and subscript j is distanced from i along the span. The estimated correlation coefficients are integrated over spanwise direction to get correlation length (Norberg, 2001),

$$\Lambda = \int R_{pp}(z)dz \tag{80}$$

where z is the location in spanwise direction. The computed correlation length is examined to determine proper span length for the present study.

2.5.4 Energy spectra, grid cutoff and Kolmogorov scale

Energy spectra $E_{ij}(\omega)$ are defined as the following form (Pope, 2000):

$$E_{ij}(\omega) = \frac{1}{2\pi}\int_{-\infty}^{\infty} R_{ij}(\tau)e^{-i\omega\tau}d\tau \tag{81}$$

where R_{ij} is two-point crosscorrelation between u_i and u_j as the following form:

$$R_{ij}(\tau) = \langle u_i(t)u_j(t+\tau)\rangle \tag{82}$$

where $\langle \quad \rangle$ is temporal average on the time span T as the following form:

$$\langle U(x,t)\rangle = \frac{1}{T}\int_{t-\frac{T}{2}}^{t+\frac{T}{2}} U(x,\tau)d\tau \tag{83}$$

In the present study, the energy spectra for streamwise velocity E_{11} are calculated with the Welch's method provided by MATLAB (Welch, 1967). Based on the energy spectra, inertial subrange is determined by fitting the Kolmogorov's -5/3 slope. Energy-containg range is determined in the lower frequencies than the inertial subrange.

The grid cutoff wave number associated with grid (Sagaut, 2006) is defined as in the following form:

$$k_c = \frac{\pi}{\Delta x} \tag{84}$$

where Δx is grid size at a point. The corresponding cutoff frequency is estimated with the grid cutoff wave number and local mean velocity at the measuring point as a convective velocity by applying the Taylor's hypothesis of frozen turbulence as in the following form:

$$\omega_c = 2\pi f_c = vk_c \tag{85}$$

where ω_c is angular frequency of cutoff frequency f_c, v is local mean velocity at the point. As shown in Fig. 2.3(a), the energy spectrum shows different behavior with CDS and upwind schemes (Mittal and Moin) up to the grid cutoff. The upwind scheme is highly dissipative and significant damping is shown in the higher range. The energy disappears even before the grid cutoff whereas the CDS scheme retain its energy up to the grid cutoff.

The Kolmogorov scales for the present study can be estimated from the similarity relation as in the following form:

$$\begin{aligned} \eta/l_0 &= \mathrm{Re}^{-3/4} \\ u_\eta/u_0 &= \mathrm{Re}^{-1/4} \\ \tau_\eta/\tau_0 &= \mathrm{Re}^{-1/2} \end{aligned} \tag{86}$$

where l_0, u_0 and τ_0 are largest scale of the turbulent flow, respectively and η, u_η and τ_η are the Kolmogorov scales for length, velocity and time defined as in the following form:

$$\begin{aligned} \eta &= (\nu^3/\varepsilon)^{1/4} \\ u_\eta &= \left(\varepsilon\nu\right)^{1/4} \\ \tau_\eta &= (\nu/\varepsilon)^{1/2} \end{aligned} \tag{87}$$

where ν is kinematic viscosity of flow and ε is viscous dissipation rate.

If u_0 is velocity scale of turbulent fluctuation, the largest velocity scale and corresponding time scale can be determined with FFT analysis. The Kolmogorov's scales for velocity and time as shown in Fig 2.3 (b) and (c) are estimated by using Eq. (86) and the length scale is determined with kinematic viscosity and viscous dissipation as in the following form:

$$\varepsilon = u_\eta^2/\tau_\eta \tag{88}$$

2.5.5 Shear layer instability analysis

In order to visualize the shear layer shedding, secondary vorticity is used. The secondary vorticity is computed by subtracting the mean velocity components $(\bar{u}, \bar{v}, \bar{w})$ from instantaneous velocity components (u, v, w). The secondary vorticity ω is expressed as the following form:

$$\boldsymbol{\omega} = \nabla \times \mathbf{v} \tag{89}$$

where components of v is $(u - \bar{u}, v - \bar{v}, w - \bar{w})$.

It is known that the ratio of the shear layer instabilities to the frequency of the Karman shedding vortices for the sub-critical Re follow a power law R^p where the exponent p is 0.67 (Prasad and Williamson, 1997) as the following form:

$$\frac{f_{sl}}{f_k} = 0.0235 \times Re^{0.67} \tag{90}$$

where f_{sl} is the shear layer instability and f_k is the frequency of the Karman shedding vortices. The f_{sl} is estimated by the FFT analysis of the streamwise velocity for the sub-, critical and super-critical Re and the trend on Re is studied in the present study.

The shear layer instabilities can be scaled on a characteristic velocity and length in a dimensional analysis (Prasad and Williamson, 1997) in the following form:

$$f_{sl} \sim \frac{V_o}{\theta} \tag{91}$$

where V_o is for the velocity outside the boundary layer at the separation point and θ for the momentum thickness. The momentum thickness Strouhal number for the shear layer instabilities is studied with the following form:

$$St_\theta = f_{sl}\theta/V_o \tag{92}$$

The momentum thickness θ is defined by the following form:

$$\theta = \int_0^\infty \frac{V(r)}{V_o}\left(1 - \frac{V(r)}{V_o}\right) dr \tag{93}$$

where the velocity V_o is defined at the point where the velocity profile reaches maximum at the separation point.

2.5.6 Turbulence intensity

The flow conditions, laminar and turbulent flows can be determined by the Turbulence intensity (White, 2010). Turbulence intensity Tu is used to determine the turbulent transition region in the laminar separation bubble. Tu is defined as in the following form:

$$Tu = \frac{u'}{U_\infty} \tag{94}$$

where u' is the root-mean-square of the turbulent velocity fluctuation and U_∞ is freestream velocity. The laminar flow appears in less than 1% Tu and the turbulent flow appears in between 5 and 20% for high-turbulence case. The transition region across the laminar separation bubble shows over 20% Tu (Pfeil and Orth 1990).

2.5.7 TKE budget equation

The resolved TKE budget for the single-phase simulation is derived from the Eq. (10). Since the density is constant with regard to time and space for the single-phase flow, Eq. (10) is rewritten in the conservative form as the following form:

$$\frac{\partial \overline{\mathbf{u}}}{\partial t} + \nabla \cdot (\overline{\mathbf{u}}\overline{\mathbf{u}}) = -\frac{1}{\rho}\nabla \bar{p} + \nu \nabla \cdot [(\nabla \overline{\mathbf{u}} + (\nabla \overline{\mathbf{u}})^T)] - \nabla \cdot \bar{\tau}, \tag{95}$$

where $\bar{\tau} = -\nu_t\,(\nabla \overline{\mathbf{u}} + (\nabla \overline{\mathbf{u}})^T)$

Momentum equation for mean flow is derived from taking time averaging operator $\langle \quad \rangle$ from Eq.(95).

$$\frac{\partial \langle \overline{u}_i \rangle}{\partial t} + \frac{\partial}{\partial x_j}\langle \overline{u}_i \overline{u}_j \rangle = -\frac{1}{\rho}\frac{\partial \langle \overline{p} \rangle}{\partial x_i} + \nu \frac{\partial}{\partial x_j}\left(\frac{\partial \langle \overline{u}_i \rangle}{\partial x_j} + \frac{\partial \langle \overline{u}_j \rangle}{\partial x_i}\right) - \frac{\partial \langle \bar{\tau}_{ij} \rangle}{\partial x_j} \tag{96}$$

where u_i,u_j are assumed to be in a Cartesian coordinate for simplicity.

Subtraction of Eq. (96) from Eq.(95) gives momentum equation of fluctuating component as the following form:

$$\frac{\partial u_i'}{\partial t} + \frac{\partial}{\partial x_j}\left(\overline{u}_i \overline{u}_j - \langle \overline{u}_i \overline{u}_j \rangle\right) = -\frac{1}{\rho}\frac{\partial p'}{\partial x_i} + \nu \frac{\partial}{\partial x_j}\left(\frac{\partial u_i'}{\partial x_j} + \frac{\partial u_j'}{\partial x_i}\right) - \frac{\partial}{\partial x_j}\left(\tau_{ij} - \tau_{ij}'\right) \tag{97}$$

Multiplying u_i' to Eq. (97) and applying the time averaging operator produce resolved-scale TKE transfer equation as the following form:

$$\frac{\partial k_{res}}{\partial t} = \underbrace{-\langle \overline{u}_j \rangle \frac{\partial k_{res}}{\partial x_j}}_{C} \underbrace{-\langle u_i' u_j' \rangle \langle \bar{S}_{ij} \rangle}_{P} \underbrace{-\frac{1}{\rho}\frac{\partial \langle u_i' p' \rangle}{\partial x_i}}_{P_T} \underbrace{-\frac{1}{2}\frac{\partial \langle u_i' u_i' u_j' \rangle}{\partial x_j}}_{T_T} + \underbrace{\nu \frac{\partial^2 k_{res}}{\partial x_j^2}}_{D} \underbrace{-2\nu \langle \bar{S}_{ij}' \bar{S}_{ij}' \rangle - \langle 2\nu_t \bar{S}_{ij} \bar{S}_{ij}' \rangle}_{\varepsilon} + \underbrace{\frac{\partial}{\partial x_j}\langle 2\nu_t u_i' \bar{S}_{ij} \rangle}_{T_{SGS}} \tag{98}$$

where resolved-scale TKE $k_{res} = \frac{1}{2}\langle u_i' u_i' \rangle$, turbulent convection C, turbulent production P, viscous dissipation ε, viscous diffusion D, turbulence transport T_T, pressure transport P_T and SGS

transport term T_{SGS} (Yue et al., 2008). In the present study, the time averaged solutions are computed for a given time span, e.g. 10 time periods corresponding to the Karman shedding frequency. The fluctuating components are calculated by subtracting the time averaged solutions from instantaneous solutions. In the present study, the resolved-scale TKE is estimated at the cell center of a grid due to the use of the staggered grid. The differentiation of each term on the RHS is implemented with the central difference scheme.

2.5.8 Proper Orthogonal Decomposition analysis

A snapshot Proper Orthogonal Decomposition (POD) is employed to assess flow structures in the shear layer and wake (Sirovich, 1987). The snapshot matrix $\mathbf{U}$ is composed of N snapshots of velocity vector $\mathbf{q}$ that consists of velocity components (u, v, w). The velocity components are fluctuating velocity calculated by subtracting the mean velocities from the individual snapshots in the present study.

$$\mathbf{U} = [\mathbf{q^1} \quad \mathbf{q^2} \quad \cdots \quad \mathbf{q^N}] = \begin{bmatrix} u_1^1 & u_1^2 & \cdots & u_1^N \\ \vdots & \vdots & \vdots & \vdots \\ u_{lmn}^1 & u_{lmn}^2 & \cdots & u_{lmn}^N \\ v_1^1 & v_1^2 & \cdots & v_1^N \\ \vdots & \vdots & \vdots & \vdots \\ v_{lmn}^1 & v_{lmn}^2 & \cdots & v_{lmn}^2 \\ w_1^1 & w_1^2 & \cdots & w_1^N \\ \vdots & \vdots & \vdots & \vdots \\ w_{lmn}^1 & w_{lmn}^2 & \cdots & w_{lmn}^N \end{bmatrix} \in R^{3lmn \times N} \tag{99}$$

where l, m and n are the size in ξ_1, ξ_2 and ξ_3 direction ad N is the number of snapshopts.

Autocovariance matrix $\tilde{\mathbf{C}}$, which is semi-definite by nature is computed as the following form:

$$\tilde{\mathbf{C}} = \mathbf{U^T U} \in R^{N \times N} \tag{100}$$

The eigenvalue problem for the autocovariance matrix provides kinetic energy (eigenvalue) and corresponding eigenvector as the following form:

$$\tilde{\mathbf{C}}\mathbf{A^i} = \lambda^i \mathbf{A^i} \tag{101}$$

where λ_i is eigenvalue and corresponding eigenvector $\mathbf{A^i} \in R^{N \times 1}$.

The eigenvalues reflecting the energies in different POD modes are arranged in descending order.

$$\lambda_1 > \lambda_2 > \cdots > \lambda_N = 0 \tag{102}$$

POD modes ϕ^i are constructed by using the eigenvectors corresponding to the ordered eigenvalues as the following form:

$$\phi^i = \frac{\sum_{n=1}^{N} A_n^i \mathbf{q^n}}{\left\| \sum_{n=1}^{N} A_n^i \mathbf{q^n} \right\|} \in R^{3lmn \times 1} \tag{103}$$

Relative kinetic energy associated with the POD mode i is obtained as the following form:

$$k^i = \frac{\lambda^i}{\sum_{i=1}^{N} \lambda^i} \tag{104}$$

In the present study, velocity vector $\mathbf{q}$ consists of contravarient variables (u_1, u_2, u_3) and snapshot matrix $\mathbf{U}$ is built with the solutions containing 10 time periods corresponding to the Karman shedding frequency. Eigenvalue problem is solved with the use of FEAST Eigenvalue Solver (Polizzi, 2009) and Intel Math Kernel Library (MKL).

2.6 References

1. Celik, I. B., Z. N. Cehreli and I. Yavuz (2005). Index of resolution quality for large eddy simulations. Journal of Fluid Engineering

2. Le, H., Moin, P. and Kim, J., 1997, Direct numerical simulation of turbulent flow over a backward-facing step. Journal of Fluid Mechanics, 330: 349–374.

3. Lilly, D. K. (1967). The representation of small scale turbulence in numerical simulation experiments.

4. Lopes, A. Silva, Ugo Piomelli, and Jose MLM Palma. (2006), Large-eddy simulation of the flow in an S-duct. Journal of Turbulence 7.

5. Meneveau, C., Lund, T. S. and Cabot W.H. (1996), A Lagrangian dynamic subgrid-scale model of turbulence. Journal of Fluid Mechanics, 319:353-385

6. Mittal, Rajat and Moin, Parviz (1997), Suitability of Upwind-Biased Finite Difference Schemes for Large-Eddy Simulation of Turbulent Flows, AIAA, 35:1415-1417

7. Norberg, C. (2001). Flow around a circular cylinder: aspects of fluctuating lift. Journal of Fluids and Structures, Elsevier. 15: 459-469

8. Pfeil H. and Orth U. (1990), Boundary-layer transition on a cylinder with and without separation bubbles. Experiments in Fluids, 10:23-32

9. Polizzi, E. (2009). Density-Matrix-Based Algorithms for Solving Eingenvalue Problems. Physical Review B

10. Prasad, A. and C. H. Williamson (1997). The instability of the shear layer separating from a bluff body. Journal of Fluid Mechanics, Cambridge Univ Press. 333: 375-402

11. Sagaut (2006). Large eddy simulation for incompressible flows. Springer. 18-19

12. Sarghini, F., U. Piomelli and E. Balaras (1999). Scale-similar models for large-eddy simulations. Physics of Fluids. 11: 1596-1607.

13. Sirovich, L. (1987). Turbulence and the dynamics of coherent structures. I - Coherent structures. II - Symmetries and transformations. III - Dynamics and scaling. Quarterly of Applied Mathematics. 45: 561-571

14. Stern, Fred, Robert Wilson, and Jun Shao. (2006), Quantitative V&V of CFD simulations and certification of CFD codes. International journal for numerical methods in fluids 50:1335-1355.

15. Suh, Jungsoo, Yang, Jianming, Stern Frederick. (2011). The effect of air-water interface on the vortex shedding from a vertical circular cylinder. Journal of Fluids and Structures, 27: 1-22.

16. Smagorinsky, J. (1963). General circulation experiments with the primitive equations: I. The basic experiment. Monthly weather review

17. Szepessy, S. (1994). On the spanwise correlation of vortex shedding from a circular cylinder at high subcritical Reynolds number. Physics of Fluids. 6: 2406-2416

18. Welch, P. (1967). The use of fast Fourier transform for the estimation of power spectra: a method based on time averaging over short, modified periodograms. IEEE Trans. Audio Electroacoust. 15:70-73

19. White, Frank M. (2010). Fluid Mechanics, 7 th, Macgraw-Hill

20. Xing, Tao, and Frederick Stern. (2010), Factors of safety for Richardson extrapolation. Journal of Fluids Engineering 132:061403.

21. Yang, J. and E. Balaras (2006). An embedded-boundary formulation for large-eddy simulation of turbulent flows interacting with moving boundaries. Journal of Computational Physics, Elsevier. 215: 12-40.

22. Yang, J. and Stern. F (2009), Sharp interface immersed-boundary/level-set method for wave-body interactions. Journal of Computational Physics, Elsevier. 228: 6590--6616

23. Yue, Wusi, Charles Meneveau, Marc B. Parlange, Weihong Zhu, Hyung Suk Kang, and Joseph Katz. (2008). Turbulent kinetic energy budgets in a model canopy: comparisons between LES and wind-tunnel experiments. Environmental Fluid Mechanics 8: 73-95.

24. Wang, Zhaoyuan, Jungsoo Suh, Jianming Yang, and Frederick Stern. (2012), Sharp Interface LES of Breaking Waves by an Interface Piercing Body in Orthogonal Curvilinear Coordinates. 50th AIAA Paper.

Table 2.1 Test cases

Case		Re	Grid	$N_x \times N_r \times N_\theta$	AR (L/D)	Method†	y^+
Sub-critical	1	6.31×10^4	Medium	$256 \times 512 \times 512 = 67M$	2	QUICK	0.03
	2		Medium	$256 \times 512 \times 512 = 67M$	2	WENO	
	3		Medium	$256 \times 512 \times 512 = 67M$	4	WENO	
	4		Fine	$512 \times 512 \times 512 = 134M$	4	WENO	
	5		Medium	$256 \times 512 \times 512 = 67M$	8	WENO	
	6		Coarse	$128 \times 256 \times 256 = 8M$	8	WENO	
	7		Medium	$256 \times 512 \times 512 = 67M$	2	NC-WENO	
	8	1.26×10^5	Medium	$256 \times 512 \times 512 = 67M$	2	QUICK	0.05
	9		Medium	$256 \times 512 \times 512 = 67M$	2	WENO	
	10		Medium	$256 \times 512 \times 512 = 67M$	4	WENO	
	11		Fine	$512 \times 512 \times 512 = 134M$	4	WENO	
	12		Medium	$256 \times 512 \times 512 = 67M$	8	WENO	
	13		Medium	$256 \times 512 \times 512 = 67M$	2	NC-WENO	
Critical	14	2.52×10^5	Medium	$256 \times 512 \times 512 = 67M$	2	QUICK	0.08
	15		Medium	$256 \times 512 \times 512 = 67M$	2	WENO	
	16		Medium	$256 \times 512 \times 512 = 67M$	4	WENO	
	17		Fine	$512 \times 512 \times 512 = 134M$	4	WENO	
	18		Medium	$256 \times 512 \times 512 = 67M$	8	WENO	
	19		Medium	$256 \times 512 \times 512 = 67M$	2	NC-WENO	
Super-critical	20	4.15×10^5	Medium	$256 \times 512 \times 512 = 67M$	2	QUICK	0.10
	21	5.06×10^5	Medium	$256 \times 512 \times 512 = 67M$	2	QUICK	0.14
	22		Medium	$256 \times 512 \times 512 = 67M$	2	NC-WENO	
	23	7.57×10^5	Medium (F)	$256 \times 512 \times 512 = 67M$	2	QUICK	0.15
	24		M	$128 \times 256 \times 256 = 8$M	2	QUICK	0.33
	25		C	$64 \times 128 \times 128 = 1M$	2	QUICK	0.67
	26		Medium	$256 \times 512 \times 512 = 67M$	2	WENO	0.15
	27		Medium	$256 \times 512 \times 512 = 67M$	4	WENO	
	28		Fine	$512 \times 512 \times 512 = 134M$	4	WENO	
	29		Medium	$256 \times 512 \times 512 = 67M$	8	WENO	
	30		Medium	$256 \times 512 \times 512 = 67M$	2	NC-WENO	

† NC-WENO is Non-conservative WENO scheme. QUICK and WENO are conservative schemes.

†† Color coded cases are to be submitted to ITTC. Detailed analysis is carried out with purple color.

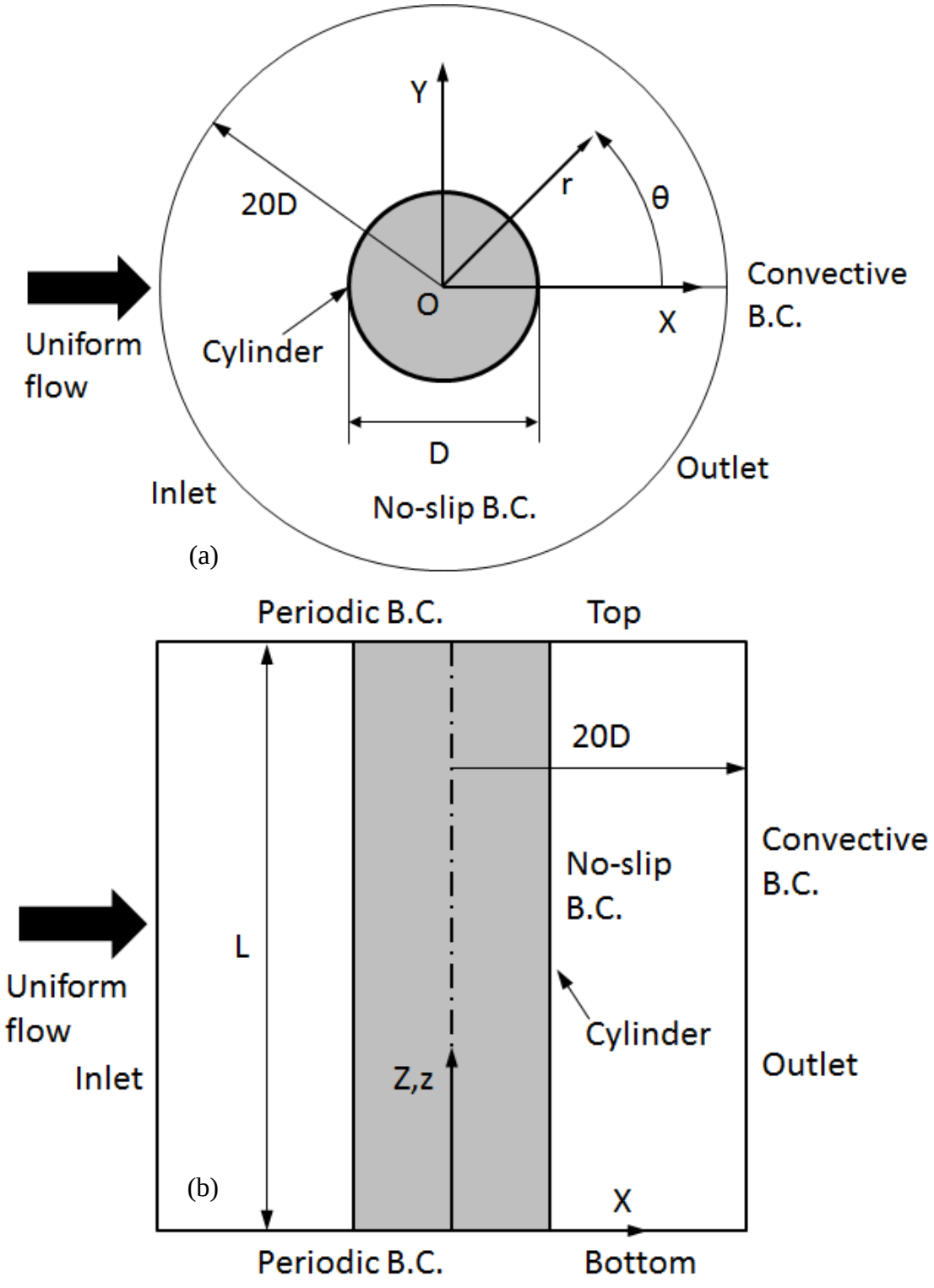

Figure 2.1. Coordinate systems and boundary conditions; (a) X-Y plane and (b) X-Z plane

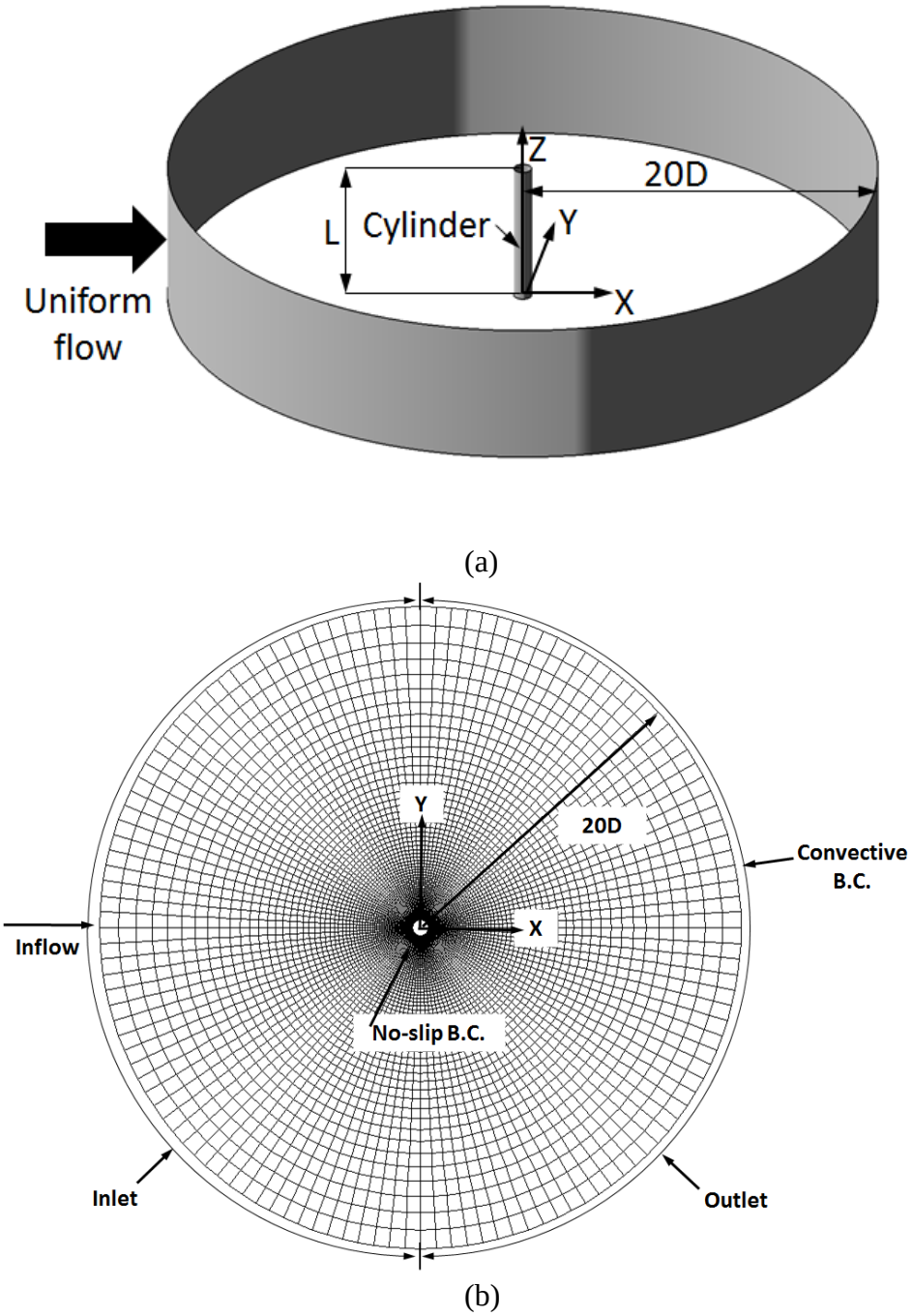

Figure 2.2 Domain size (a) and body-fitted grid around a cylinder (b)

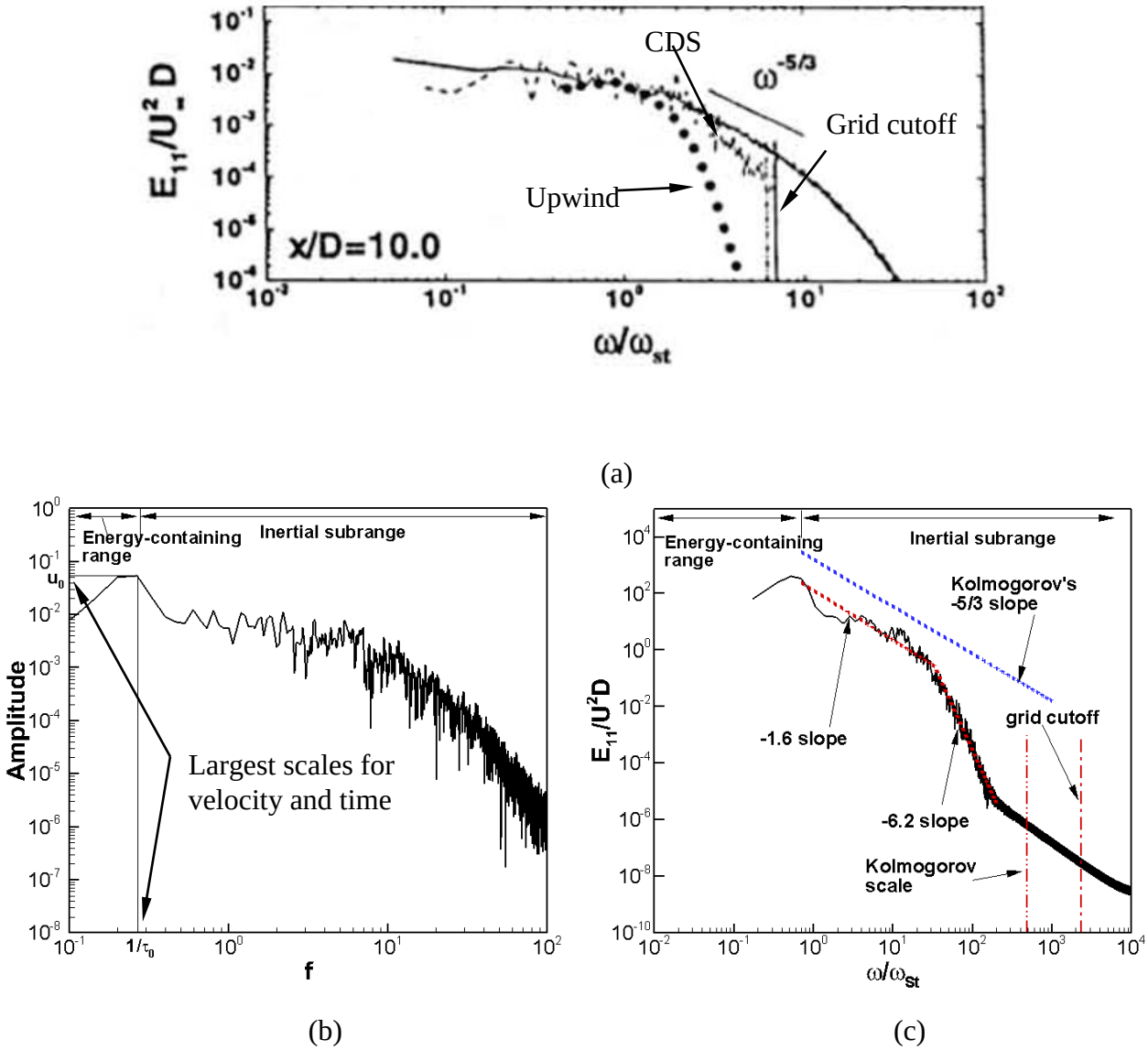

Figure 2.3 Energy spectrum for streamwise velocity of a circular cycliner: (a) grid cutoff and numerical dissipation (Mittal and Moin, 1997) (b) largest scales of turbulent flow obtained from FFT analysis (c) energy spectrum with grid cutoff and Kolmogorov scale

CHAPTER 3

QUANTITATIVE VERIFICATION AND VALIDATION AND SENSITIVITY STUDIES

3.1 Statistical Convergence

Fig. 3.1 shows time history of the drag (C_D) and lift (C_L) coefficients with running mean. The statistically stationary state is determined by using the convergence of the running mean of the C_D. When the fluctuations of the running mean are smaller than 1% of the mean value, the flow is considered as statistically stationary. For instance, the C_D reaches statistically stationary state at t=80 in Fig. 3.1 (a). After reaching the statistically stationary state, flow field data covering 20 vortex shedding cycles are used for the statistics as specified in the ITTC OEC Workshop. The shedding period is obtained from the FFT analysis of the C_L and corresponds to the Strouhal number. Fig. 3.2 shows FFT analysis of the drag and lift coefficients where the mean is removed from the signal. The dominant frequencies from the lift coefficient are: about 0.2 for the sub-critical Re [Fig. 3.2 (a) and (b)]; broad range for the critical Re [Fig. 3.2 (c)]; and in a range of 0.34 – 0.41 for the super-critical Re [Fig. (d), (e) and (f)]. The dominant frequencies from the drag coefficient are: about 0.35-0.37 for the sub-critical Re [Fig. 3.2 (a) and (b)]; broad range for the critical Re [Fig. 3.2 (c)]; and in a range of 0.72-0.80 for the super-critical Re [Fig. (d), (e) and (f)]. The frequencies for the drag coefficients are about twice of those from the lift coefficients and agree with results from VIV studies (Bearman, 1984).

3.2 Quantitative Verification and Validation

Table 3.1 shows the study of quantitative verification and validation for $Re=7.57x10^5$. The computations are conducted with QUICK scheme since its numerical stability property is better than the CDS scheme and it is less expensive than the WENO scheme in terms of computational cost. The grids denoted by F, M and C represent fine, medium and coarse grids systematically refined by the refinement ratio r_G of 2, respectively. As the grid is refined, the C_D, C_L^{RMS} are close to the experimental data whereas the $-C_{pb}$ is almost constant around the

experimental data.

Since the Courant-Friedrichs-Lewy (CFL) number corresponding to the present time step of $1x10^{-4}$ is in a range between 0.3 and 0.4, the time step uncertainty U_T is not considered in the present study. The iterative uncertainty U_I is estimated from the dynamic range of the running mean for the C_D. The C_D, C_L^{RMS} and $-C_{pb}$ are in monotonic convergence since the convergence ratio R_G is in the interval between 0 and 1. The theoretical order of accuracy of the QUICK scheme p_{th} is assumed second order of accuracy due to the use of a non-uniform grid. The ratio P for the C_D, C_L^{RMS} and $-C_{pb}$ is 0.7, 0.8 and 0.9. The grid uncertainty U_G for the C_D, C_L^{RMS} and $-C_{pb}$ is relatively large, 24.9%S_1, 50.4%S_1 and 0.34%S_1, respectively. It implies that the grid can be refined for the improvement of the solutions. Further grid refinement is not considered due to the limited computational resources and time. The U_I for the C_D is two order less than U_G and negligible.

The comparison error E for the C_D is 2.8%D and less than the validation uncertainty U_V of 24.9%D where experimental uncertainty U_D is assumed 2%D and facility bias uncertainty U_{FB} is 5%D. The E for the C_L^{RMS} is 4.0%D and less than the U_V of 4.9%D. The E for the $-C_{pb}$ is 1.4%S_1 and less than the U_V of 2.0%D. Therefore, the C_D, C_L^{RMS} and $-C_{pb}$ is validated at the U_V interval.

3.3 Effect of Aspect Ratio, Grid resolution and Convection Scheme

Sensitivity studies were conducted for the effect of AR, grid resolution and convection scheme for the C_D, C_L^{RMS} and $-C_{pb}$ as shown in Tables 3.2-3.5. The cases submitted to the workshop are highlighted. The correlation length of experimental data Λ/D from Fig. 1.9 (b) is included in the table captions for reference.

For the sub-critical Re, tables 3.2 and 3.3 clearly show that the error is decreasing in terms of $\overline{E}$ with increasing AR, where $\overline{E}$ is the average of comparative errors for C_D, C_L^{RMS} and $-C_{pb}$. The best results are obtained for the AR=8 which indicates AR=8 needed even if the spanwise density decreases with AR. For the grid resolution study, the $\overline{E}$ shows increasing

behavior with increasing grid resolution. For the convection scheme study, the NC-WENO shows the best results in terms of $\overline{E}$. However, it is premature to deduce definitive conclusions about the grid resolution and convection scheme as AR may play a major role in these cases; small AR (AR=4 and 2) were used for the grid resolution and convection scheme studies, respectively.

For the critical Re, table 3.4 shows that the $\overline{E}$ is slightly increasing with increasing AR in terms of $\overline{E}$. The oscillatory convergence for effects of AR are observed in terms of C_D but the variation is little; the best result based on C_D was obtained at AR=8. For the grid resolution study, $\overline{E}$ increases slightly for increased grid resolution but the variation is relatively small compared with that for the sub-critical Re. The Λ/D is small which indicates large AR not needed. However, the grid resolution study for AR=4 show increasing behavior. It is premature to conclude if the solutions show converging behavior due to the lack of cases for systematic grid study. Based on the fact that the variations with AR and grid resolution are little, it can be concluded that the effect of AR and grid resolution is little under the present setup. The variables undergo critical behavior and small deviations from experimental data can result in large errors. As observed in Fig. 1.1 (a), the variations of variables differ from facilities and flow conditions for the critical Re. Thus, the main cause of the large comparison error is due to the sharp behavior of variables as well as different flow conditions including turbulence intensity of freestream. For the convection scheme study, the WENO and NC-WENO schemes have much less error than QUICK. The prediction for QUICK is much smaller than that of two schemes, WENO and NC-WENO that are comparable each other. Although further investigation is needed for clarification, the main differences between QUICK and WENO (including NC-WENO) schemes may be attributed to the order of accuracy as well as numerical dissipation. The relatively small differences between WENO and NC-WENO are attributed to the form of convection scheme.

For the super-critical Re, table 3.5 shows that AR=2 provides the best results since grid resolution is best and large AR not needed since Λ/D is small. The error is decreasing with

decreasing AR. For the grid resolution study, the results show converging behavior with increasing grid resolution. For the convection scheme study, the results of the WENO and QUICK are acceptable since errors of both WENO and QUICK are relatively small whereas the errors of the NC-WENO are very large. Based on the results, it can be concluded that the form of convection scheme has much influence to the solution compared with order of accuracy of the scheme.

3.4 Conclusions

The solutions were considered statistically converged when the running mean oscillations were smaller than 1% of the mean value. The simulations were continued for 20 Karman vortex shedding for statistical analysis, as specified in the ITTC OEC Workshop.

A quantitative verification and validation study was conducted with the statistically stationary variables, C_D, C_L^{RMS} and $-C_{pb}$ for the super-critical Re ($Re=7.57x10^5$) using the QUICK scheme. The variables showed monotonic convergence; however, the grid uncertainties for C_D and C_L^{RMS} have large values over $20\%S_1$ and $50\%S_1$, respectively. This implies that grids much finer than the current fine grid (67M) are required for the super-critical Re. The E values were 2.8, 4 and 1.4%D, respectively. Thus, the solutions were validated but with very large validation uncertainty due to large numerical grid uncertainty.

For the sub-critical Re, the strong dependency on the AR was observed. The AR=8 provided the best results for the sub-critical Re. The results of the grid resolution and convection scheme studies were not conclusive since small AR was used.

For the critical Re, in general, the effect of AR and grid resolution was small under the present setup despite small variations with increasing AR and grid resolution. The best results were obtained with AR=8 in terms of C_D. Main cause of the large comparison difference was due to the critical behavior of variables and flow conditions including turbulence intensity of freestream. For the convection scheme, two schemes (QUICK and WENO) showed significantly different results which is likely due to the order of accuracy, numerical dissipation and numerical

errors. Two schemes (WENO and NC-WENO) with conservative and non-conservative form provided results with little variations. The inherent momentum conservation of numerical scheme may hardly influence the solutions for critical Re regime but further scrutiny over the behavior of the schemes is needed for clear conclusion.

For the super-critical Re, the best results were observed for AR=2 since the grid resolution was good enough to resolve the turbulent flow structures and large AR was not needed. For the grid resolution study, the results showed converging behavior with increasing grid resolution. For the convection scheme, conservative form (QUICK and WENO) provided acceptable results compared with non-conservative form (NC-WENO). It implies that the momentum conservation is crucial for the solutions for super-critical Re regime.

Based on the AR, grid resolution and convection scheme studies, best results were selected for the submission to the ITTC OEC Workshop. Definitely, AR=8 gave the best results for the sub-critical Re. It was not easy to decide the best case for the critical Re because the average errors were large for all the study cases. Nonetheless, AR=8 gave better results in terms of C_D for the critical Re despite small variation with AR. Clearly, AR=2 gave the best results for the super-critical Re. For the convection scheme, conclusive results were not found for the sub-critical Re since AR effect prevailed with the use of small AR. For the critical Re, the results by QUICK showed early drag crisis compared with experimental data and that by WENO with the same AR. For the super-critical Re, conservative form showed better results for the super-critical Re. Even though QUICK provided better results than others, the results by WENO was considered as more reliable since QUICK scheme had an issue of early formation of drag crisis for the critical Re. Furthermore, one of the main purpose of this study was to study the behavior of the WENO in conservative and non-conservative form for the super-critical Re. In this regard, the results by WENO scheme was chosen for the further studies. Therefore, case 5 and 12 for the sub-critical and case 18 for the critical and case 20, 21 and 26 for the super critical Re were chosen and submitted to the ITTC OEC Workshop; case 20 and 21 was computed by only QUICK scheme.

Clearly more comprehensive and systematic convergence studies are needed especially for the sub-critical Re using large AR for the grid and convection scheme studies.

3.5 References

1. Bearman, P W (1984). Vortex shedding from oscillating bluff bodies. Annual Review of Fluid Mechanics, 16: 195—222

Table 3.1 Summary of simulations performed for verification and validation for super-critical Re ($Re=7.57x10^5$)

Study	AR	Grid size (M)	C_D	C_L^{RMS}	$-C_{pb}$
Experiment					
Schewe (1983)	10		0.23	0.027	-
Shih et al. (1993)	8.2		-	-	0.24
Grid study					
Case 23 (F)	2	67	0.224	0.052	0.236
Case 24 (M)	2	8	0.266	0.083	0.238
Case25 (C)	2	1	0.373	0.177	0.244
Verification					
		$U_I\%S_1$	0.27	-	-
		U_I/ε_{21}	0.48	-	-
		R_G	0.40	0.33	0.28
		P_{RE}	1.30	1.60	1.80
		P	0.70	0.80	0.90
		$U_G\%S_1$	24.9	50.4	0.34
Validation					
		$U_{SN}\%D$	24.3	4.4	0.3
		$U_{FB}\%D$	5.0	-	-
		$U_V\%D$	24.9	4.9	2.0
		E%D	2.8	4.0	1.4

Table 3.2 Sensitivity study for sub-critical Re ($Re=6.31x10^4$) and computed integral parameters with $\Lambda/D=3.3$

Case	Grid (N_x x N_r x N_θ)	AR	Density (N_x/AR)	Scheme	C_D	E%D	C_L^{rms}	E%D	$-C_{pb}$	E%D	$\bar{E}$
Medium grid w/ different AR											
2	256x512x512=67Mil.	2	128	WENO	1.60	33	1.14	101	2.11	62	65
3	256x512x512=67Mil.	4	64	WENO	1.41	18	0.95	68	1.11	-15	34
5	256x512x512=67Mil.	8	32	WENO	1.37	14	0.60	9	1.42	9	11
	Average										37
Different grid density w/ AR=4											
3	256x512x512=67Mil.	4	64	WENO	1.41	18	1.14	101	1.11	-15	45
4	512x512x512=134Mil.	4	128	WENO	1.65	38	0.95	68	2.02	56	54
	Average										49
Medium grid w/ different convection schemes											
1	256x512x512=67Mil.	2	128	QUICK	1.69	41	1.32	131	2.00	54	75
2	256x512x512=67Mil.	2	128	WENO	1.60	33	1.14	101	2.11	62	65
7	256x512x512=67Mil.	2	128	NC-WENO	1.35	13	0.83	48	2.02	56	39
	Average										60
Experiment											
	Schewe (1983)				1.20		-		-		
	Norberg (1987)				-		-		1.30		
Szepessy and Bearman (1992)					-		0.55		-		

Table 3.3 Sensitivity study for sub-critical Re ($Re=1.26x10^5$) and computed integral parameters with $\Lambda/D=2.9$

Case	Grid (N_x x N_r x N_θ)	AR	Density (N_x/AR)	Scheme	C_D	E%D	C_L^{rms}	E%D	$-C_{pb}$	E%D	$\overline{E}$
Medium grid w/ different AR											
9	256x512x512=67Mil.	2	128	WENO	1.25	5	1.08	89	1.78	34	43
10	256x512x512=67Mil.	4	64	WENO	1.46	23	0.97	70	1.97	48	47
12	256x512x512=67Mil.	8	32	WENO	1.37	15	0.62	10	1.43	8	11
	Average										34
Different grid density w/ AR=4											
10	256x512x512=67Mil.	4	64	WENO	1.46	23	0.97	70	1.97	48	47
11	512x512x512=134Mil.	4	128	WENO	1.58	33	1.21	111	2.10	58	67
	Average										57
Medium grid w/ different convection schemes											
8	256x512x512=67Mil.	2	128	QUICK	0.83	-30	0.035	-90	0.34	-75	65
9	256x512x512=67Mil.	2	128	WENO	1.25	5	1.08	89	1.78	34	43
13	256x512x512=67Mil.	2	128	NC-WENO	1.25	5	0.76	34	1.72	30	23
	Average										44
Experiment											
	Schewe (1983)				1.29		-		-		
	Norberg (1987)				-		-		1.32		
Szepessy and Bearman (1992)					-		0.56		-		

Table 3.4 Sensitivity study for critical Re ($Re=2.52x10^5$) and computed integral parameters with $\Lambda/D=0.8$

Case	Grid (N_x x N_r x N_θ)	AR	Density (N_x/AR)	Scheme	C_D	E%D	C_L^{rms}	E%D	$-C_{pb}$	E%D	$\bar{E}$
Medium grid w/ different AR											
15	256x512x512=67Mil.	2	128	WENO	0.55	-45	0.15	-3	0.49	-51	33
16	256x512x512=67Mil.	4	64	WENO	0.54	-46	0.17	0	0.44	-56	34
18	256x512x512=67Mil.	8	32	WENO	0.56	-44	0.12	-9	0.44	-56	36
	Average										34
Different grid density w/ AR=4											
16	256x512x512=67Mil.	4	64	WENO	0.54	-46	0.17	0	0.44	-56	34
17	512x512x512=134Mil.	4	128	WENO	0.48	-52	0.14	-5	0.46	-54	37
	Average										36
Medium grid w/ different convection schemes											
14	256x512x512=67Mil.	2	128	QUICK	0.27	-73	0.06	-19	2.00	54	49
15	256x512x512=67Mil.	2	128	WENO	0.55	-45	0.15	-3	2.11	62	37
19	256x512x512=67Mil.	2	128	NC-WENO	0.62	-38	0.22	9	2.02	56	34
	Average										40
Experiment											
	Schewe (1983)				1.01		0.17		-		
	Norberg (1987)				-		-		1.00		

Table 3.5 Sensitivity study for super-critical Re ($Re=7.57x10^5$) and computed integral parameters with $\Lambda/D=1.3$

Case	Grid (N_x x N_r x N_θ)	AR	Density (N_x/AR)	Scheme	C_D	E%D	C_L^{rms}	E%D	$-C_{pb}$	E%D	$\bar{E}$
Medium grid w/ different AR											
26	256x512x512=67Mil.	2	128	WENO	0.21	-9	0.04	2	0.34	35	15
27	256x512x512=67Mil.	4	64	WENO	0.34	48	0.10	12	0.31	23	28
29	256x512x512=67Mil.	8	32	WENO	0.30	65	0.09	11	0.36	43	40
	Average										28
Different grid density w/ AR=4											
27	256x512x512=67Mil.	4	64	WENO	0.34	48	0.10	12	0.31	23	28
28	512x512x512=134Mil.	4	128	WENO	0.30	30	0.07	7	0.36	42	26
	Average										27
Medium grid w/ different convection schemes											
23	256x512x512=67Mil.	2	128	QUICK	0.22	-4	0.05	4	0.24	-7	5
26	256x512x512=67Mil.	2	128	WENO	0.21	-9	0.04	2	0.34	35	15
30	256x512x512=67Mil.	2	128	NC-WENO	0.43	87	0.10	12	0.50	98	66
	Average										29
Experiment											
Schewe (1983)					0.23		0.027		-		
Shih et al. (1993)					-		-		0.24		

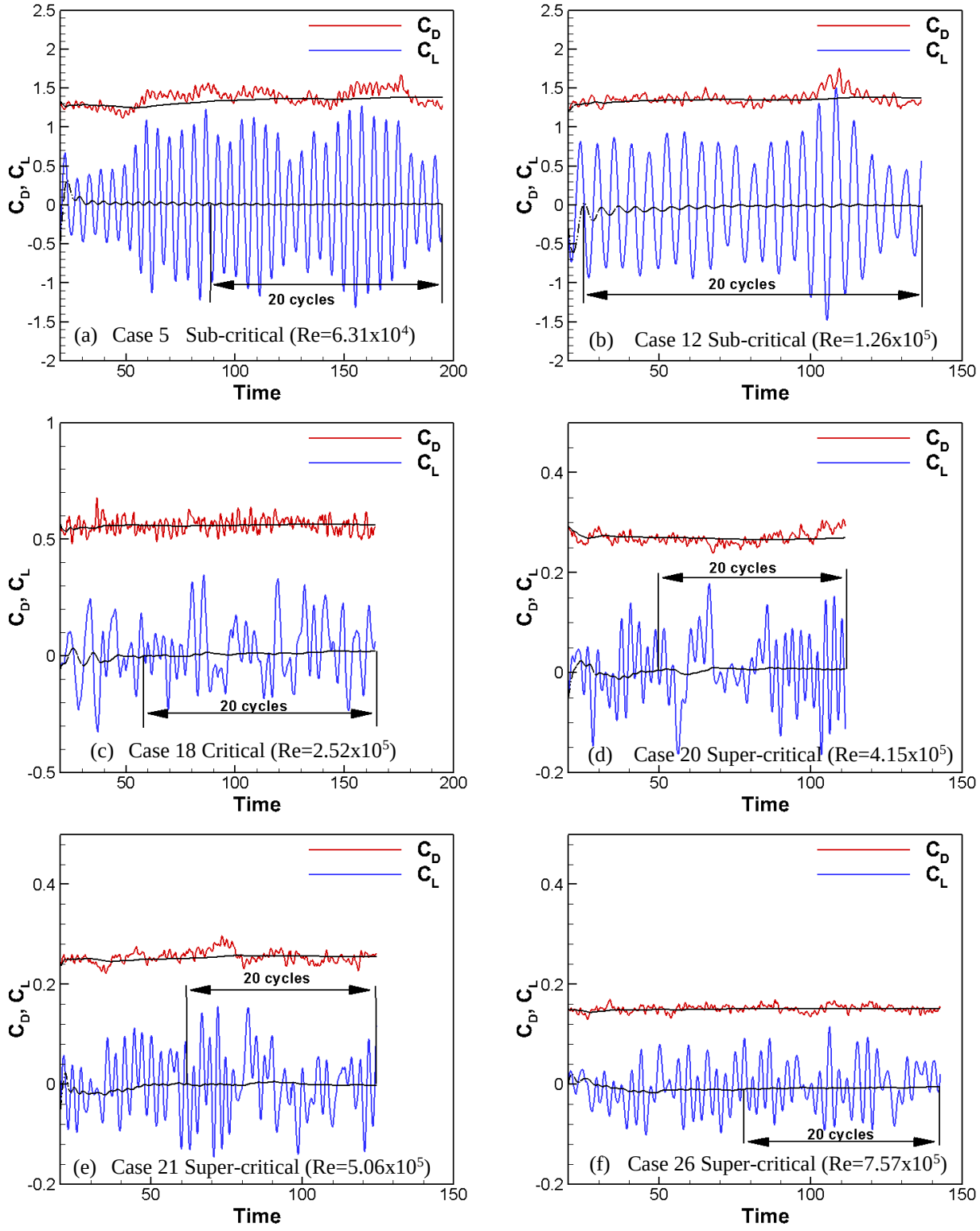

Figure 3.1 Time history of drag and lift coefficients

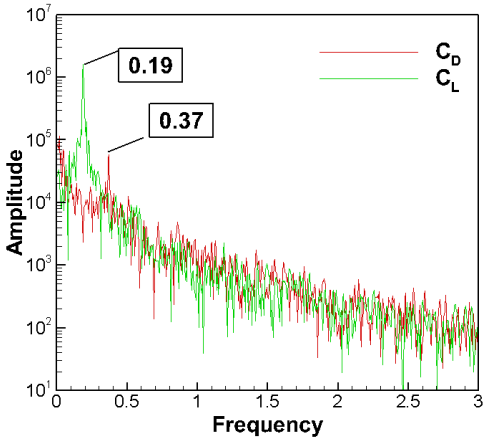

(a) Case 5 Sub-critical ($Re=6.31x10^4$)

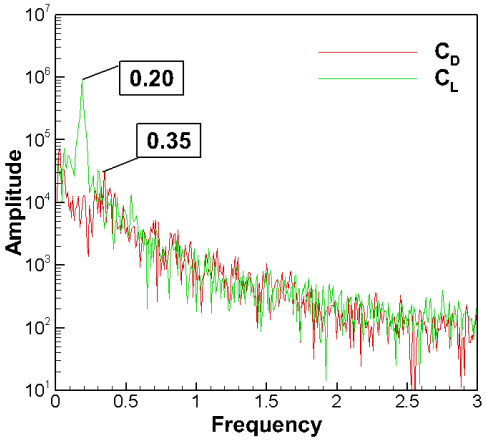

(b) Case 12 Sub-critical ($Re=1.26x10^5$)

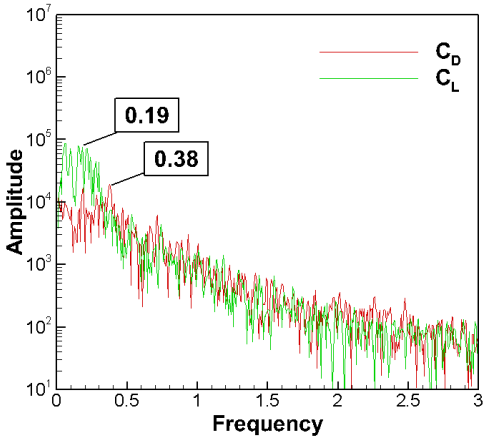

(c) Case 18 Critical ($Re=2.52x10^5$)

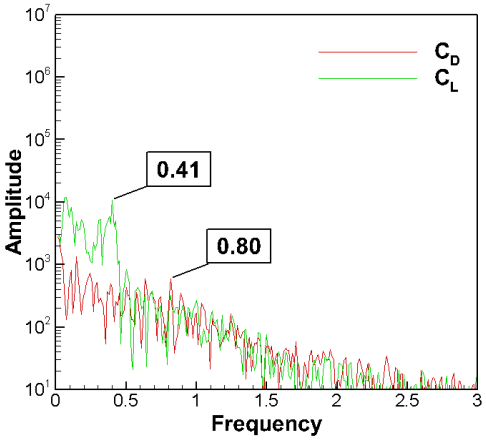

(d) Case 20 Super-critical ($Re=4.15x10^5$)

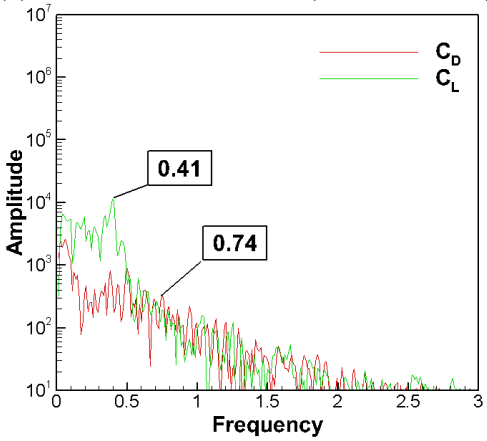

(e) Case 21 Super-critical ($Re=5.06x10^5$)

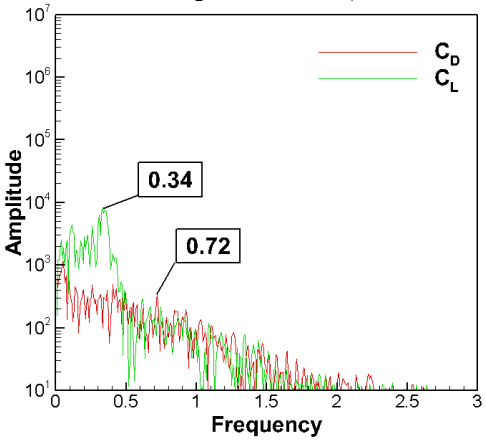

(f) Case 26 Super-critical ($Re=7.57x10^5$)

Figure 3.2 FFT analysis of 20 cycles of drag and lift coefficients

CHAPTER 4

VALIDATION

The cases selected for submission to the ITTC Workshop were used for validation, as highlighted in Table 2.1. For sub-critical Re, cases 5 and 12 are for $Re=6.31x10^4$ and for $Re=1.26x10^5$, respectively. For critical Re, case 18 is for $Re=2.52x10^5$. For super-critical Re, cases 20, 21 and 26 are for $Re=4.15x10^5$, $Re=5.06x10^5$ and $Re=7.57x10^5$, respectively. The most detailed analysis is done for sub-, critical and super-critical cases 12, 18 and 26, respectively. Assessment is made of the quality of the LES by analysis of the index of resolution quality IQ and balance of the momentum and TKE equations followed by validation using the benchmark experimental data in the same order as discussed in Chapter 1.

4.1 Assessment of LES Quality

Fig. 4.1 shows the IQ distribution for all six selected cases. Time average of turbulent eddy viscosity is used for the computation of the IQ; the data size cover about 10 time periods corresponding to the Karman shedding frequency. The contour levels are from 0.8-1; thus, the present LES meets the requirement that $IQ \geq 0.8$. Table 4.1 summarizes the average values for boundary layer, shear layer and wake regions, as shown in Fig. 4.1. Average values of IQ increase with Re and are largest for the boundary layer, followed by the shear layer and wake.

The momentum equations of Eq. (13)-(15) in the orthogonal curvilinear coordinate are used to validate the momentum equation solver. Interpolation is made of the pressures on the cell faces. Residual of each component is computed from the difference between the RHS and LHS of the equations. The instantaneous velocity components for the sub-critical Re($Re=1.26x10^5$) are shown in Fig. 4.2 (a), (c) and (e) and the residuals of the equations are shown in Fig. 4.2 (b), (d) and (f), respectively. The contravariant variables including velocity are transformed into the physical domain. The errors are small with largest values for the shear layer and some parts of vortex shedding regions. The magnitude of imbalanced region in the shear layer and shedding vortices is in the order of 10^{-6}, 10^{-3} and 5×10^{-4}, respectively, whereas instantaneous

solutions are in the order of 1. The linear interpolation produces considerable numerical error when sharp gradient is involved in the region. Main cause of the imbalance is due to the numerical error by interpolating the pressure at the cell surfaces in region of sharp gradient. Despite the numerical error, the residuals are negligible compared with the instantaneous solution, which implies the momentum equations are balanced.

The resolved-scale TKE budgets are computed from the LES solutions. Table 4.2 shows ratio of spatially averaged TKE budget values for each data size to that for 120 cycles in order to determine the statistically stationary solution condition for the super-critical Re ($Re=7.57x10^5$). Fig. 4.3 (a) shows the test region for the spatial average of TKE budgets. The region extends to 1D away from the cylinder center and includes both the shear layer and near wake. Time period corresponding to the Karman shedding frequency is considered as a unit data size; about 30 data are contained in a time period for the super-critical Re. All the TKE budget terms show rapidly converging trend with increasing number of data. The ratio shows significantly decreasing behavior and relatively small variation is observed after 10 cycles except for PT and D. 120 cycles could be considered as statistically stationary solution condition for the present study. Table 4.3 shows the spatially averaged TKE budget values for each data size. As expected, T_{SGS} term has very small value and little contribution to the TKE budgets. The viscous dissipation ε is under-estimated and not balanced with P due to numerical dissipation. The residual (sum of TKE budgets) over 10 cycles has the same order of magnitude as C and P. Hence the balance of TKE budget is not obtained. Fig. 4.4 shows the ratios of the residual to each terms in the TKE budget equations; the region with value below 10^{-7} of the absolute residual value is blanked since the value can be considered as balanced region according to Fig. 4.3 (b). Large ratio values for the C and P are shown around the shear layer. This distribution agrees with the results by Yue et al. (2008) and is due to the numerical error by applying linear interpolation to the regions of sharp gradient region. In spite of that, the maximum ratio value for the C and P is about 0.4 and four times larger than that by Yue et al. (2008). Since Re=670 by Yue et al. (2008) is much lower than $Re=7.57x10^5$, numerical error due to the linear interpolation is not the same. Apart from that,

numerical dissipation due to convection scheme is likely to affect the ratio values: CDS for Yue et al. (2008) and upwind scheme (WENO) for the present study. Nonetheless, a qualitative TKE analysis can be made considering that large ratios only occur in limited regions in the solution field.

Figs. 4.5 – 4.7 show the resolved-scale TKE budgets for sub-, critical and super-critical Re, respectively. The data size for the sub- and critical Re covers 10 cycles due to the limited computational resources and time. For the super-critical Re, 120 cycles are used. The P is the major term for the sub-, critical and super-critical Re. The maximum turbulent production occurs in the separated flow near the wall. The T_T and C are second major term followed by P_T. The C is negative in the shear layer indicating that the C advects energy from upstream to downstream. The T_T is negative where the P is large and positive where the P is small. It implies that the T_T removes energy from the shear layer region and delivers the energy to the regions near wall and away from the shear layer. The behavior of the T_T resembles that in the recirculation region of a backward-step flow (Le et al. 1997). The P_T is very small except in the region close to the wall. The D is negligible because flows are dominated by inertial forces at the very high Re.

Figs.4.8-4.10 show the TKE budget distributions along a line from the cylinder wall parallel to the Y axis. Fig. 4.8 shows the TKE budget distributions before LS. For all the cases, major terms are P_T and C. It implies that the P_T provides energy before the separation and the C advects the energy from upstream to downstream. The magnitude is relatively large close to the wall and exponentially decreases away from the wall. The magnitude of P is very small and concentrated in the thin region near the wall.

Fig. 4.9 shows the TKE budget distributions across shear layer for the sub- and critical Re. For the critical Re, the distribution is across the secondary vorticity region right after the separation. After separation, the P_T has little contribution to the TKE balance. Major terms are P, T_T and C. The P increases from the wall and reaches maximum in the shear layer. The T_T is negative below the shear layer and positive out of the shear layer and reaches minimum where P is maximum. The behavior of the T_T indicates that the TKE energy is distributed from the shear

layer to outside of the shear layer. The C shows different distributions inside of the shear layer for the sub- and critical Re. For the sub-critical Re, there are two regions by convective motion; energy loss near wall and energy gain near shear layer. For the critical Re, the C has little contribution to the TKE balance for the critical Re.

Fig. 4.10 shows the TKE budget distributions near key points (TT, TR and TS) for the super-critical Re. For TT as key point, major terms are P, T_T, C and P_T. The P_T is largest near the wall and rapidly decreases away from the wall. The P reaches maximum at the boundary of the separation bubble and the TKE energy is advected by the convective motion. On the contrary to the behavior in the shear layer, the T_T provides energy to the TKE instead of removing. For TR and TS as key points, the major terms are P and C and other terms have little contribution to the TKE balance. The P is maximum close to the wall and rapidly decays away from the wall. The C reaches minimum in the shear layer and advects energy.

4.2 Energy spectra and dissipation

Table 4.4 and 4.5 shows the grid cutoff wavenumbers calculated from the cell size in streamwise direction in the shear layer near the body and wake centerline 3D away from the cylinder center for the sub-, critical and super-critical Re. The wavenumbers are converted into corresponding frequency by using the local mean velocity as a convective velocity. Table 4.6 and 4.7 show the estimated Kolmogorov scales. The largest scales are estimated from FFT analysis of the local velocity fluctuation and the Kolmogorov scales are calculated by using Eq. (87) and (89). The estimated Kolmogorov wavenumbers are smaller than the grid cut-off wavenumbers in the shear layer close to the cylinder and much larger in the wake centerline. For the shear layer close to the cylinder, the grid has high resolution for the turbulent flow to be resolved, where the turbulence intensity is lower than that in the wake. For the wake centerline, the grid cutoff is much smaller, which indicates that the body fitted grid gets coarse in streamwise direction and does not have resolution to resolve as small flow structure as in the s shear layer close to the cylinder.

Fig. 4.11 shows the energy spectra of streamwise velocity with estimated grid cutoff and Kolmogorov scale. The inertial subrange and energy-containing range are determined by fitting the Kolmogorov's -5/3 slope to the energy spectra. For the shear layer close to the body, the energy spectra show the scaling exponents close to the Kolmogorov slope at low wavenumbers, which indicates that the present LES study properly modeled the turbulence and preserved the energy decay behavior although the ranges of wavenumbers following the Kolmogorov slope becomes narrower with increasing Re. The rapid energy decay is observed followed by the scaling exponents close to the Kolmogorov slope, which is due to the numerical dissipation of upwind scheme as shown in Fig 2.3. For the wake centerline, the range of the scaling exponents are much smaller, even in sub-critical Re since the grid resolution become coarse and small-scale structures are not resolved.

The flow in the shear layer near the body can be regarded as fully resolved with the present grid resolution since the grid cutoff covers the Kolmogorov scale. Due to numerical dissipation, the spectra cannot retain the Kolmogorov's energy decay rate up to grid cutoff but only the large, energy carrying scales are resolved. The grid resolution in the wake centerline is lower than that of shear layer near the body but the most important, energy carrying scales are captured. Because of the dissipative upwind convection schemes, it is necessary to have better grid resolution in the wake to resolve major energy carrying scales, such that the numerical dissipation in the higher wavenumbers doesn't affect the turbulence statistics (Mittal and Moin, 1997).

4.3 Validation of LES

Fig. 4.12 (a), (b) and (c) show comparisons of the LES C_D, θ_{LS}/θ_{TS} and $-C_{pb}$, respectively. The drag crisis is well predicted, although more cases in the critical and post-critical regime are desirable. The angle of separation is close to the experiments for sub- and critical Re, but substantially under predicted for super-critical Re. The base suction pressure shows good agreement with the experiments for sub- and super-critical Re, but is under predicted

for critical Re. Fig. 4.13 (a), (b) and (c) show comparisons for the LES C_L, C_L^{RMS} and St, respectively. The LES C_L shows nearly zero values similarly as the experiments, except those with asymmetric laminar separation bubbles near the boundary of critical Re. The LES C_L^{RMS} is close to the most reliable data for sub-, critical and super-critical Re. The LES St is close to the experiments for sub- and critical Re, but under-predicts for super-critical. In the quantitative verification and validation study, relatively large grid uncertainty, especially for C_L^{RMS} was observed. Since time history of lift coefficient is highly correlated to St, the under-estimation of St for the super-critical Re is likely due to grid coarseness. Tables 4.8 and 4.9 summarize the experimental D, simulation S, comparison error E and facility bias U_{FB} values for all six selected cases. For C_D the average E is 22%D, which is over twice as large as U_{FB} = 10%D. The largest E is for critical Re, where the drag drops sharply with small changes in Re resulting in large changes in C_D between facilities and likely simulations. The E for the other variables are also relatively large that is average E =6/38, 27, 7 and 7%D for θ_{LS}/θ_{TS}, $-C_{pb}$, C_L^{RMS} and St, respectively.

Fig. 4.14 compares the LES pressure, shear stress and angular pressure gradient distributions against the experimental data for all six selected cases. The key points are labeled on the figures. The LES shows fairly close agreement with the experiments in spite of the Re differences, including details such as the laminar separation bubble. Table 4.10 summarizes the angular average E for C_p, C_f and $dp/d\theta$ and the Re average values are 8, 24 and 14%D, respectively.

Fig. 4.15 shows the LES mean velocity and turbulence intensity near the separation bubble and key point values are shown in Table 4.11. Since the diameter is non-dimensionalized in the LES, the figure is dimensionalized with the diameter 300 mm as in the experiment (Pfeil and Orth, 1990). The separation bubble is distinguishable by the zero mean velocity level, which is tear drop shaped initiating at LS (94 deg), maximum at TT (102 deg), and terminating at TR (105 deg); the E for LS, TT and TR are -6, -7 and -8%D, respectively. The transition of the separated shear layer is indicated by the sudden increase in the turbulence intensity at around 102

deg. The LES mean velocity and turbulence intensity contours shows similar distribution to that of the experiment with early formation of the separation bubble. It should be noted that the flow condition including Re, roughness and freestream turbulence is not identical between the experimental and the present simulation. The discrepancy between the present LES study and experiment is attributed in part to the differences. The separation bubble reaches its maximum thickness at around 102 deg and the thickness is about 0.05. Even though the location of separation bubble is formed earlier in the present LES, the thickness and the level of turbulent intensity are almost identical to the experiment. The angle from LS to TT and to TR are 8 and 11, respectively and almost identical to experimental data; the E are -20 and -21%D, respectively, where small changes can result in relatively large E values due to small angle.

A close up view of the sub-critical LS, critical LS bubble, and super-critical LS, TT, TR, TS regions are shown along with turbulence intensity in Fig. 4.16 (a), (b) and (c), respectively. Following Pfeil and Orth (1990), the TT is determined by the turbulence intensity level and rate across the maximum boundary of the bubble. For sub-critical Re, the laminar flow is observed before LS and maintained for the beginning part of the separated flow. Turbulent transition occurs in the shear layer and the maximum value appears after the separation at around x=0.3. The boundary layer and some part of separated boundary layer are laminar. For critical Re, the laminar flow is observed right after LS followed by turbulent transition. A secondary vorticity is formed after the LS but reattachment is not observed. The turbulent transition occurs through the secondary vorticity and the turbulence intensity increases as flow goes downstream. For super-critical Re, the laminar flow is observed up to TT. A separation bubble is formed right after LS and TR is observed at the end of the bubble. The turbulent transition appears across the separation bubble followed by TR as shown by Pfeil and Orth (1990).

The key points and their E are summarized in Tables 4.12 and 4.13, respectively, and graphically displayed in Fig. 4.17. The trends qualitatively agree with the experiments. The LES E for LS is 6%D, but MP, TR, TS are mostly under-predicted with average E =17, 15 and 38%D, respectively. The large E for TS could be attributed to the turbulence intensity of the freestream

and the roughness of the cylinder in the experiments; however, LES numerical methods and grid refinement are also issues. Fig. 4.18 (a), (b) and (c) show the key points along with the mean and instantaneous streamlines for sub-, critical and super-critical Re, respectively. The mean streamlines show closed-separation for all Re with wide long bubble for sub, narrow shorter bubble for critical and narrow long bubble for super critical Re. The instantaneous streamlines are chaotic. Fig. 4.19 shows enlarged mean streamlines for critical and super-critical Re near the separated flow. For the critical Re, the separated flow beginning at LS forms a secondary vorticity close to the wall, which amalgamates into recirculation bubble without reattaching to the wall. For the super-critical Re, the separated flow forms a secondary vorticity, which reattaches to the wall forming a bubble referred to as the laminar separation bubble. The different behavior of the secondary vorticity for the critical and super-critical Re suggests that the kink in the mean pressure distribution as shown in Fig. 4.14 does not guarantee the existence of the laminar separation bubble. For the critical Re, shedding vortices along the wall are observed in the instantaneous flow field and these vortices form a secondary vorticity without reattachment in the mean flow field. For the super-critical Re, the stationary secondary vorticity is generated in the instantaneous flow field and these vortices form a separation bubble in the mean flow field; detailed flow structures for the secondary vorticity in boundary layer will be discussed in section 5.5.

Fig. 4.20 shows the comparison of the Reynolds stresses with the experiments for sub-critical Re along with LES results for sub-, critical and super-critical Re. The average E for u'v', u'u' and v'v' are 9, 12 and 30%D for sub-critical Re, which is partially due to Re differences, as listed in Table 4.14. In general the LES over-predicts the experimental data. The Reynolds stress magnitudes decrease with Re.

Table 4.15 and 4.16 shows the LES comparison for the effective shear layer length Ls and recirculation length Lr for sub-critical Re and comparison error E, respectively. For the Ls, since only DNS results are available and limited to lower Re ($< 10^4$), direct comparison is not possible. The DNS results show decreasing trend and the present LES follows the trend; the

decreasing trend is shown in the comparison error to $Re=1.0x10^4$ as well. For the Lr, experimental data is limited, especially for the sub-critical Re. the measurement by Cantwell and Coles (1983) can cover the sub-critical Re of the present LES. $Re=1.26x10^5$ is best-fitted for the comparison to the experiment. The Lr is 0.92 and the E is -2%D, which indicates accurate prediction of good turbulence in the wake centerline. Relatively large error for $Re=6.31x10^4$ is partially due to Re differences.

Fig. 4.21 (a) shows the comparison for the correlation coefficient with experiments for sub- and critical Re along with LES results for sub-, critical and super-critical Re. The LES are all for AR = 8, i.e., cases 5, 12, 18, and 29. For sub- and critical Re, the LES shows similar trends (increasing slope) as the data but with scatter. For critical and super-critical Re, the LES suggests that the slope continues to increase with Re, but here again the LES results show scatter. Fig 4.21 (b) shows the comparison for the correlation length with experiments for sub- and critical Re along with LES results for sub-, critical and super-critical Re. For sub- and super critical Re, the LES is close to the data and empirical formula, whereas it under-predicts the data/formula for critical Re. The D and S values and E for the correlation length are included in Tables 4.8 and 4.9, respectively. The E is largest for critical Re.

The shear-layer frequency was analyzed for sub-, critical and super-critical Re using both the FFT of the streamwise velocity time history and the shear layer wavelength λ_{SL} and velocity V_{SL} ($f_{SL}= V_{SL}/\lambda_{SL}$) with secondary vorticity contour. In the latter case, non-dimensional St_{SL} using V_{SL} and the momentum thickness at separation and normalized shear layer frequency f_{SL}/f_K are evaluated. Fig. 4.22 (a), (b) and (c) show the mean velocity vectors and secondary vorticity contours with mean centerline of shear layer for sub-, critical and super-critical Re. Apart from the shear layer shedding, the shear layer shows oscillating motion due to the alternating vortex shedding in the wake. The maximum and minimum location of the instantaneous shear layer are overlaid on the mean velocity vectors and denoted as upper and lower boundaries of shear layer. The mean centerline of shear layer moves to the cylinder wall as Re increases and the transition point of the shear layer, the point where first shedding was found, moves upstream up to the

separation point. For the super-critical Re, the boundary between shear layer and boundary layer is hard to distinguish and the layers are close enough to interact.

Fig. 4.23 shows the FFT analysis for the streamwise velocity at the three analysis points marked in Fig. 4.22 and the results are listed in Table 4.17 along with the variables used for the shear-layer frequency analysis. LES shear-layer frequencies f_{SL} are observed in much higher frequency than the Karman shedding frequency f_K. As illustrated in Fig. 4.22, the shear layer undergoes low frequency oscillation due to the Karman vortex shedding in the wake. As a result, the f_K is captured in the spectrum as shown in Fig. 4.23. Fig. 4.24 shows the comparison of f_{SL}/f_K with the experimental data. Table 4.17 summarizes the values for location (r,θ) and f_{SL} based on the FFT analysis and V_{SL} , λ_{SL}, $f_{SL,}$ $V_{o,}$ Θ, St_{SL}, and $f_{SL}/f_{K,}$ and its E based on the secondary vorticity and mean velocity. The St_{SL} values increase from 0.159 to 0.168 for the sub-, critical Re and reduce to 0.028 for the super-critical Re due to the significantly reduced momentum thickness Θ. Based on that the momentum thickness is used on account of boundary layer formation, the boundary layer has similarity up to the critical Re for the present setup. The considerably reduced momentum thickness for the super-critical Re is likely due to the proximity and interaction of the shear layer and boundary layer. The LES f_{SL}/f_K values are for greater Re than the experiments, but show similar trends for sub- and critical and lower value for super-critical.

4.4 Conclusions

The quality of the present LES study was assessed with a single grid estimator and satisfied the requirement that $IQ \geq 0.8$ all over the flow field. The subsequent balance check of the solutions for momentum equations generated small residual values, which indicates that the flow solver conserved momentum.

The resolved-scale TKE budgets were estimated with LES solutions. Statistically stationary solution condition was obtained with 120 cycles. The additional term due to subgrid-scale stress had little effect to the TKE budget. The viscous dissipation was smaller than the

production term. Relatively large residual ratios to C and P were observed around the shear layer and likely due to the numerical dissipation by convection scheme and numerical error by linear interpolation.

A qualitative TKE budget study was conducted around the cylinder and in the wake. The major term was turbulent production term, which had the maximum values in separated flow region. The turbulent transport term was removing the energy from where turbulent production term had large values and distributing the energy into the flow field. The convection term was advecting the energy from upstream to downstream. These behaviors were similar to that of a backward-step flow.

The contribution of each TKE budget varied at key points. The TKE near the wall was driven by the pressure transport and convection terms before the separation. After the separation, the pressure transport term had little contribution to the TKE. Across the separation bubble for the super-critical Re, the turbulent production term showed maximum values near transition point, which agreed with the behavior of the turbulence intensity from the experiment. The turbulent transport term was providing energy in the transition region instead of removing the energy.

Energy spectra were estimated in the shear layer near the body and the wake centerline with streamwise velocity. The energy decay rate showed that the turbulence were properly modeled in the present LES study. The grid had sufficient resolution to fully resolve the flow in the shear layer near the body. In the wake centerline, much lower resolution was observed and higher grid resolution was needed to resolve major energy carrying scales although most important scales were resolved.

Integral and local variables were studied for validation of the present LES study and the summary of comparison error E was summarized in Table 4.18. The $C_{D,} –C_{pb}$, $C_L{}^{RMS}$ and St were predicting the behavior of the drag crisis well although more cases in the critical and post-critical Re were needed. The average of E for the C_D was 16, -39 and 14 for the sub-, critical and super-critical Re, respectively. The largest E was observed in the critical Re because the drag

drops sharply with small changes in Re. The average of E for the U_{FB} was 8, 9 and 11 for the sub-, critical and super-critical Re, respectively. The U_{FB} was comparable to the E for C_D, which indicates that the drag prediction can be considerably affected by the flow and facility conditions. The average of E for the $-C_{pb}$ was 18, -56 and 24 for the sub-, critical and super-critical Re, respectively. The largest E was observed in the critical Re due to the sharp behavior of the variable. The average of E for the C_L^{RMS} was 9, -8 and 5 for the sub-, critical and super-critical Re, respectively and relatively small error was observed. The average of E for the St was 3, 0 and 17 for the sub-, critical and super-critical Re. Relatively large error was found for the super-critical Re, which was attributed to the large grid uncertainty for the C_L^{RMS} shown in chapter 3.

The key point values including LS for the sub- and critical Re and LS, TT and TR for the super-critical Re were close to the experiments based on Table 4.11 and 4.13. The TS for the super-critical Re was considerably under-predicted indicating early turbulent separation. The average of E for the LS was 5 and -8 for the sub- and critical Re and -6 for the super-critical Re. The average of E for the TS was 38 for the super-critical Re and relatively large compared to LS, which indicates the TS does not take place far downstream of the cylinder wall. Pressure and shear stress distributions showed close agreement with experiments, especially for the sub-critical Re. The average of E for the C_p was 4, 13 and 9, and 12, 40 and 26 for C_f, and 6, 17 and 19 for $dp/d\theta$ for the sub-, critical and super-critical Re, respectively. Due to the strong dependency on the facility and flow conditions, large error was observed for the critical Re. For the super-critical Re, the early prediction of turbulent separation resulted in relatively large error.

The turbulence transition was studied with the turbulence intensity, especially near the separation bubble for the super-critical Re. For the sub- and critical Re, laminar separation was observed and turbulence transition occurred in the separated flows. For the super-critical Re, the bubble thickness and the distribution of turbulence intensity near the bubble were almost identical to the experiments. The E for the LS, TT and TR were -6, -7, -8, respectively and made a good agreement despite early prediction. The E for the TS was about 38 and relatively large,

which implies that the turbulent separation does not occur far downstream as in the experimental data.

The Reynolds stresses in wake were studied for the sub-critical Re. The E for the shear and streamwise component was 9 and 12 and agreed well with the experiment. The E for the transverse component was 30 and over-predicted. In general, the LES simulation tends to over-predict the Reynolds stresses, especially in transverse component.

The effective shear layer length and recirculation length for the sub-critical Re were studied for the validation. Even though direct comparison could not be made and resulted in large E of 27 due to the difference of Re, the effective shear layer length followed the decreasing behavior of the DNS results with increasing Re. The E for the recirculation length was 6 and showed accurate prediction with the experimental data.

The correlation coefficient and length were studied for the sub-, critical and super-critical Re. The slope of the correlation coefficients along the spanwise direction showed increasing behavior as Re increased. The correlation length decreased with increasing Re, which indicates that large AR for the sub-critical and small AR for the super-critical Re were needed in order to minimize the three-dimensional effect. The E was 5, -67 and 18 for the sub-, critical and super-critical Re. Fairly good agreement was made for the sub- and super-critical Re but large error was found due to the sharp behavior for the critical Re.

The shear layer frequency was analyzed with FFT and wavelength of secondary vorticity. The shear layer frequency was found in the higher range than the Karman shedding frequency and followed a power law up to the critical Re but dropped significantly for the super-critical Re; the E for the normalized frequency showed 11, 21 and 78 for the sub-, critical and super-critical Re. The momentum thickness showed that the similarity of the boundary layer formation was retained up to the critical Re and lost for the super-critical Re due to the interaction of boundary layer and shear layer. As a result, the E for the super-critical showed large deviation.

For the clear analysis of the TKE budgets, a careful examination is needed in terms of numerical scheme and data size since very expensive computational cost is expected to resolve

the thin boundary layer and get the statistically stationary solution. It will be much severe condition if CDS scheme is used as an energy-conserving and non-dissipative scheme since CDS scheme is very sensitive to the grid quality. Overall integral variables showed fairly good agreement for the sub- and super-critical Re even though some facility biases were found. The largest error was observed in the critical Re because of its sharp behavior. Local variables were limited and showed close agreement for the sub-critical Re but relatively large errors were found for the critical and super-critical Re. Especially, good agreement of turbulence intensity and mean velocity contour was observed despite an early turbulent separation were predicted. The discrepancy is likely due to the turbulence intensity in the freestream since the experimental setup has turbulence intensity in the freestream however small it is. Thus, the effect of turbulence intensity in the freestream should be studied to be clear. Additionally, many validation data did not provide the details of experimental setup including uncertainty factors, turbulence intensity in freestream and surface roughness. Most of the validation data were outdated and focused on integral variables. It makes new comprehensive studies desirable, especially for local flow.

4.5 References

1. Le, Hung, Parviz Moin, and John Kim. (1997), Direct numerical simulation of turbulent flow over a backward-facing step. Journal of Fluid Mechanics 330:349-374.

2. Mittal, Rajat and Moin, Parviz. (1997), Suitability of Upwind-Biased Finite Difference Schemes for Large-Eddy Simulation of Turbulent Flows, AIAA, 35:1415-1417

3. Pfeil H. and Orth U. (1990), Boundary-layer transition on a cylinder with and without separation bubbles. Experiments in Fluids, **10**:23-32

4. Yue, Wusi, Charles Meneveau, Marc B. Parlange, Weihong Zhu, Hyung Suk Kang, and Joseph Katz. (2008), Turbulent kinetic energy budgets in a model canopy: comparisons between LES and wind-tunnel experiments. Environmental Fluid Mechanics **8**: 73-95.

Table 4.1 Summary of mean IQ and range of boundary layer, shear layer and wake

	Re	Region	r/D		θ (deg)		Mean
			Min.	Max.	Min.	Max.	IQ
Sub-critical	$6.31x10^4$	BL	0.5	0.52	62	85	0.952
		SL	0.5	0.80	106	140	0.902
		Wake	0.5	3.00	-160	160	0.879
		Average					0.911
	$1.26x10^5$	BL	0.5	0.52	62	85	0.952
		SL	0.5	0.80	106	140	0.896
		Wake	0.5	3.00	-160	160	0.878
		Average					0.909
Critical	$2.52x10^5$	BL	0.5	0.52	75	110	0.947
		SL	0.5	0.65	106	132	0.898
		Wake	0.5	3.00	-160	160	0.880
		Average					0.908
Super-critical	$4.15x10^5$	BL	0.5	0.52	75	110	0.939
		SL	0.5	0.60	116	142	0.931
		Wake	1.0	3.00	-165	165	0.918
		Average					0.929
	$5.06x10^5$	BL	0.5	0.52	75	110	0.952
		SL	0.5	0.60	116	142	0.927
		Wake	1.0	3.00	-165	165	0.898
		Average					0.926
	$7.57x10^5$	BL	0.5	0.52	75	110	0.952
		SL	0.5	0.60	116	142	0.926
		Wake	1.0	3.00	-165	165	0.903
		Average					0.927

Table 4.2 Convergence ratio to 120 cycles of TKE budgets for $Re=7.57x10^5$

Cycles	residual $E\%S_{120}$	C $E\%S_{120}$	P $E\%S_{60}$	P_T $E\%S_{120}$	T_T $E\%S_{120}$	D $E\%S_{120}$	ε $E\%S_{120}$	T_{SGS} $E\%S_{120}$
4	-95	-11	-15	150	-58	305	-5	-99
8	-23	31	-7	92	40	128	-5	5
10	-9	-3	12	25	-2	-31	2	12
60	1	0	2	2	6	7	1	2
120	-	-	-	-	-	-	-	-

Table 4.3 Spatial average of TKE budgets for $Re=7.57x10^5$

Cycles	residual	C	P	P_T	T_T	D	ε	T_{SGS}
4	$6.71x10^{-4}$	$5.95x10^{-2}$	$6.77x10^{-2}$	$9.47x10^{-3}$	$5.67x10^{-4}$	$5.68x10^{-6}$	$6.90x10^{-3}$	$2.31x10^{-5}$
8	$9.57x10^{-3}$	$8.80x10^{-2}$	$7.45x10^{-2}$	$7.26x10^{-3}$	$1.89x10^{-3}$	$3.20x10^{-6}$	$6.89x10^{-3}$	$1.37x10^{-5}$
10	$1.13x10^{-2}$	$6.51x10^{-2}$	$8.94x10^{-2}$	$4.75x10^{-3}$	$1.33x10^{-3}$	$9.70x10^{-7}$	$7.40x10^{-3}$	$1.46x10^{-5}$
60	$1.26x10^{-2}$	$6.72x10^{-2}$	$8.19x10^{-2}$	$3.85x10^{-3}$	$1.44x10^{-3}$	$1.50x10^{-6}$	$7.38x10^{-3}$	$1.34x10^{-5}$
120	$1.25x10^{-2}$	$6.70x10^{-2}$	$8.00x10^{-2}$	$3.79x10^{-3}$	$1.36x10^{-3}$	$1.40x10^{-6}$	$7.28x10^{-3}$	$1.31x10^{-5}$

Table 4.4 Cell size in streamwise direction of the grid points and grid cutoff estimation of shear layer

	Re	z/D	r/D	θ (deg)	$\overline{\Delta}$	v	k_c	ω_c	ω_c/ω_{St}
Sub-critical	1.26 x10^5	-4 (midspan)	0.63	121	0.001265	1.06	2484	2633	2095
Critical	2.52 x10^5	-4 (midspan)	0.53	118	0.001099	1.20	2859	3431	2730
Super-critical	7.57 x10^5	-1 (midspan)	0.50	127	0.001112	1.27	2826	3589	2856

Table 4.5 Cell size in streamwise direction of the grid points and grid cutoff estimation of wake centerline

	Re	z/D	r/D	θ (deg)	$\overline{\Delta}$	v	k_c	ω_c	ω_c/ω_{St}
Sub-critical	1.26 x10^5	-4 (midspan)	3.00	0	0.03532	0.63	89	56	45
Critical	2.52 x10^5	-4 (midspan)	3.00	0	0.03532	0.72	89	64	51
Super-critical	7.57 x10^5	-1 (midspan)	3.00	0	0.03532	0.79	89	70	33

Table 4.6 Estimation of Kolmogorov scale of shear layer

Re	u_0	f_0 (τ_0)	u_η	τ_η	ε	η	ω_η/ω_{St}
1.26x10^5	0.05	0.26 (3.85)	2.65x10^{-3}	1.08x10^{-2}	6.50x10^{-4}	9.36x10^{-4}	486
2.52x10^5	0.01	0.28 (3.57)	4.46x10^{-4}	7.11x10^{-3}	2.80x10^{-5}	1.22x10^{-4}	740
7.57x10^5	0.04	0.48 (2.08)	1.36x10^{-4}	2.39x10^{-3}	7.74x10^{-6}	7.39x10^{-5}	1228

Table 4.7 Estimation of Kolmogorov scale of wake centerline

Re	u_0	f_0 (τ_0)	u_η	τ_η	ε	η	ω_η/ω_{St}
$1.26x10^5$	0.05	0.06 (15.74)	$2.93x10^{-3}$	$4.43x10^{-2}$	$6.50x10^{-4}$	$1.27x10^{-3}$	113
$2.52x10^5$	0.04	0.20 (5.00)	$1.13x10^{-3}$	$9.97x10^{-3}$	$2.80x10^{-5}$	$8.30x10^{-4}$	502
$7.57x10^5$	0.03	0.35 (2.82)	$7.50x10^{-4}$	$3.24x10^{-3}$	$7.74x10^{-6}$	$3.40x10^{-4}$	907

Table 4.8 Summary of integral and local variables with experimental data

	Re		C_D	θ_{LS}	θ_{TS}	$-C_{pb}$	C_L^{RMS}	St	f_K	Λ/D
Sub-critical	$6.31x10^4$	D	1.20	81	-	1.30	0.55	0.20	-	3.5
		S	1.37	82	-	1.46	0.60	0.19	0.19	3.3
	$1.26x10^5$	D	1.16	75	-	1.32	0.56	0.20	-	3.0
		S	1.37	81	-	1.64	0.62	0.20	0.20	2.9
Critical	$2.52x10^5$	D	0.92	94	-	1.00	0.17	0.19	-	2.4
		S	0.56	89	-	0.44	0.12	0.19	0.19	0.8
Super-critical	$4.15x10^5$	D	0.36	-	136	0.24	0.021	0.47	-	1.2
		S	0.27	95	113	0.30	0.064	0.41	0.41	-
	$5.06x10^5$	D	0.29	-	139	0.24	0.023	0.47	-	1.1
		S	0.25	96	113	0.25	0.061	0.41	0.41	-
	$7.57x10^5$	D	0.23	-	135	0.24	0.027	0.46	-	1.1
		S	0.21	94	112	0.34	0.042	0.34	0.34	1.3

Table 4.9 Errors of integral and local variables

	Re	C_D		θ_{LS}	θ_{TS}	$-C_{pb}$	C_L^{RMS}	St	Λ/D
		E%D	U_{FB}%D	E%D	E%D	E%D	E%D	E%D	E%D
Sub-critical	$6.31x10^4$	14	9	2	-	12	8	-5	-6
	$1.26x10^5$	18	7	9	-	24	10	0	-3
	Average	16	8	5		18	9	3	5
Critical	$2.52x10^5$	-39	9	-8	-	-56	-8	0	-67
Super-critical	$4.15x10^5$	-25	21	-	-36	25	7	-13	-
	$5.06x10^5$	-14	6	-	-41	4	6	-13	-
	$7.57x10^5$	-4	5	-	-36	42	3	-26	18
	Average	14	11	-	38	24	5	17	18
Total average		23	10	6	38	33	7	7	30

Table 4.10 Mean errors of local variables

	Re	C_p E%D	C_f E%D	$dp/d\theta$ E%D
Sub-critical	$6.31x10^4$	4	10	5
	$1.26x10^5$	4	13	7
	Average	4	12	6
Critical	$2.52x10^5$	13	40	17
Super-critical	$4.15x10^5$	9	28	16
	$5.06x10^5$	9	27	18
	$7.57x10^5$	9	23	22
	Average	9	26	19
Total average		9	26	14

Table 4.11 Comparison of keypoints and thickness of separation bubble

	Re	θ_{LS} (deg)	θ_{TT} (deg)	$\delta(\theta_{TT}-\theta_{LS})$ (deg)	θ_{TR} (deg)	$\delta(\theta_{TR}-\theta_{LS})$ (deg)	θ_{TS} (deg)	$\delta(\theta_{TS}-\theta_{TR})$ (deg)	Thickness (mm)
Experiment (Pfeil et al., 1997)	$6.00x10^5$	100	110	10	114	14	-	-	0.05
Present LES	$7.57x10^5$	94	102	8	105	11	110	5	0.05
E%D		-6	-7	-20	-8	-21	-	-	-

Table 4.12 Key points of the present LES study

	Re	θ_{MP} (deg)	θ_{LS} (deg)	$\delta(\theta_{LS}-\theta_{MP})$ (deg)	θ_{TT} (deg)	$\delta(\theta_{TT}-\theta_{LS})$ (deg)	θ_{TR} (deg)	$\delta(\theta_{TR}-\theta_{LS})$ (deg)	θ_{TS} (deg)	$\delta(\theta_{TS}-\theta_{TR})$ (deg)
Sub-critical	$6.31x10^4$	69	82	13						
	$1.26x10^5$	69	81	12						
Critical	$2.52x10^5$	77	89	8						
Super-critical	$4.15x10^5$	82	95	13	102	7	104	9	111	7
	$5.06x10^6$	83	96	13	102	6	104	8	111	7
	$7.57x10^6$	82	94	12	102	8	105	11	110	5

Table 4.13 Errors for key points of the present LES study

	Re	θ_{MP} E%D	θ_{LS} E%D	$\delta(\theta_{LS}-\theta_{MP})$ E%D	θ_{TT} E%D	$\delta(\theta_{TT}-\theta_{LS})$ E%D	θ_{TR} E%D	$\delta(\theta_{TR}-\theta_{LS})$ E%D	θ_{TS} E%D	$\delta(\theta_{TS}-\theta_{TR})$ E%D
Sub-critical	$6.31x10^4$	-8	2	53						
	$1.26x10^5$	-12	9	20						
	Average	10	5	37						
Critical	$2.52x10^5$	4	-8	-80						
Super-critical	$4.15x10^5$	-25	-	87	-	-	-15	-30	-36	-61
	$5.06x10^6$	-25	-	87	-	-	-15	-40	-41	-61
	$7.57x10^6$	-25	-	80	-	-	-15	-10	-36	-68
	Average	25		85	-	-	15	27	38	63
Total average		17	6	68	-	-	15	27	38	63

Table 4.14 Mean errors of Reynolds stresses for sub-critical Re

	Re	u'v' E%D	u'u' E%D	v'v' E%D
Sub-critical	$1.26x10^5$	9	12	30

Table 4.15 Effective shear layer length Ls and recirculation length Lr

	Re	L_s/D	L_r/D
Experiment(Cantwell and Coles 1983)	$1.41x10^5$	-	0.94
DNS(Dong et al. 2006)	$3.90x10^3$	1.59	-
	$1.00x10^4$	1.03	-
Sub-critical (Present LES)	$6.31x10^4$	0.80	0.85
	$1.26x10^5$	0.70	0.92

Table 4.16 Error of effective shear layer length Ls and recirculation length Lr

	Re	L_s/D E%D	L_r/D E%D
Sub-critical (Present LES)	$6.31x10^4$	-22	-10
	$1.26x10^5$	-32	-2

Table 4.17 Estimation of frequency of shear layer vortices

	Re	z/D	r/D	θ (deg)	f_{SL} (FFT)	V_{SL}	λ_{SL}	f_{SL}	V_o	Θ	St_{SL}	f_{SL}/f_K	f_{SL}/f_K E%D
Sub-critical	1.26 x10^5	-4 (midspan)	0.63	121	11.8	1.06	0.0825	12.9	1.388	0.0171	0.159	68	11
Critical	2.52 x10^5	-4 (midspan)	0.53	118	20.7	1.20	0.0530	22.6	1.668	0.0124	0.168	119	21
Super-critical	7.57 x10^5	-1 (midspan)	0.55	121	15.1	1.27	0.0823	15.4	1.781	0.00275	0.028	45	-78

Table 4.18 Summary of comparison errors

Re	C_D E%D	C_D U_{FB}%D	θ_{LS} E%D	θ_{TS} E%D	$-C_{pb}$ E%D	C_L^{RMS} E%D	St E%D	Λ/D E%D	C_p E%D	C_f E%D	dp/dθ E%D	u'v' E%D	u'u' E%D	v'v' E%D	Ls/D E%D	Lr/D E%D	f_{SL}/f_K E%D	$\overline{E}$
Sub-critical	16	8	5	-	18	9	3	5	4	12	6	9	12	30	27	6	11	11
Critical	-39	9	-8	-	-56	-8	0	-67	13	40	17	-	-	-	-	-	21	25
Super-critical	14	11	-	38	24	5	17	18	9	26	19	-	-	-	-	-	78	24
Average	23	10	6	38	33	7	7	30	9	26	14	9	12	30	27	6	37	20

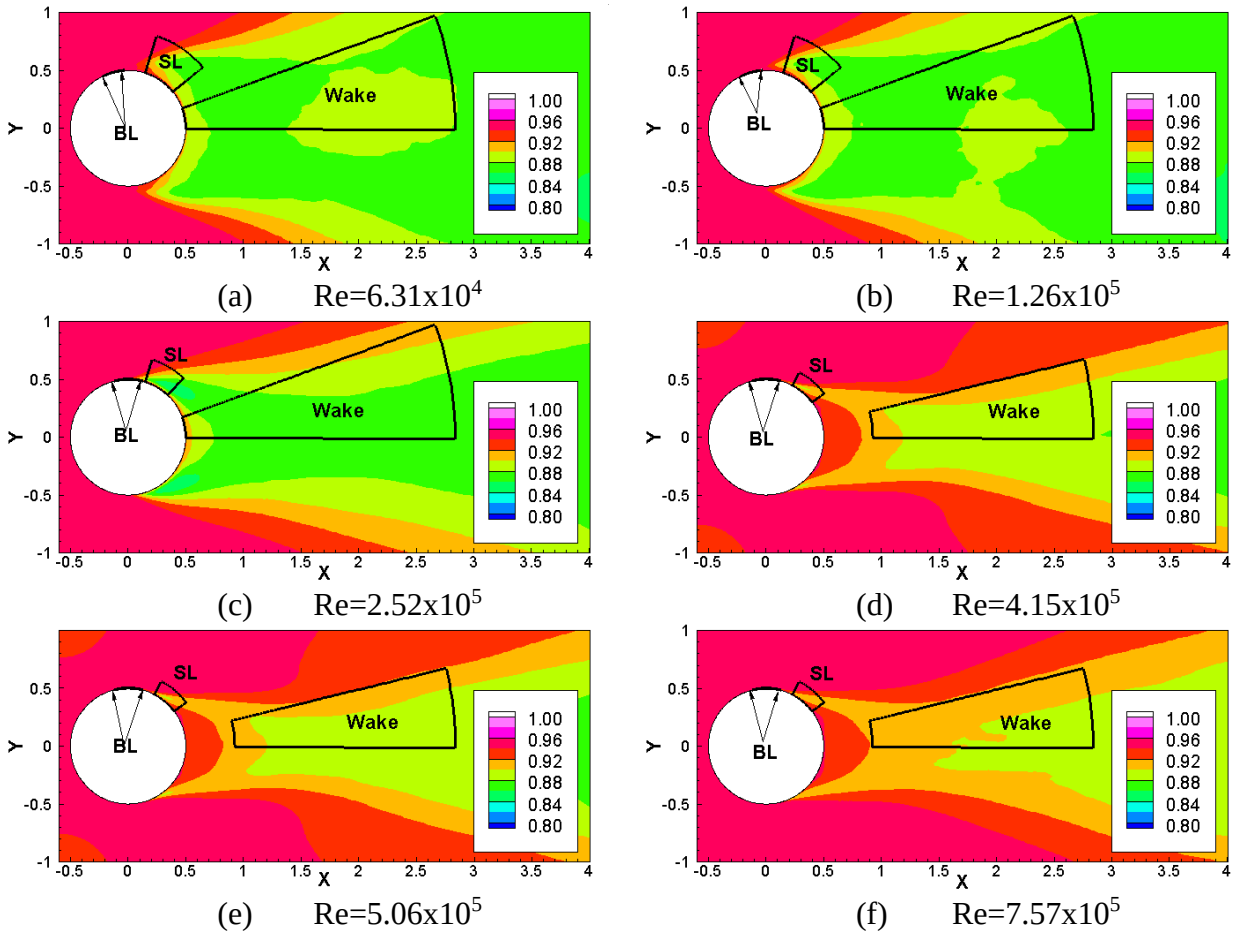

Figure 4.1 IQ distribution with averaging regions; half region is indicated for the wake.

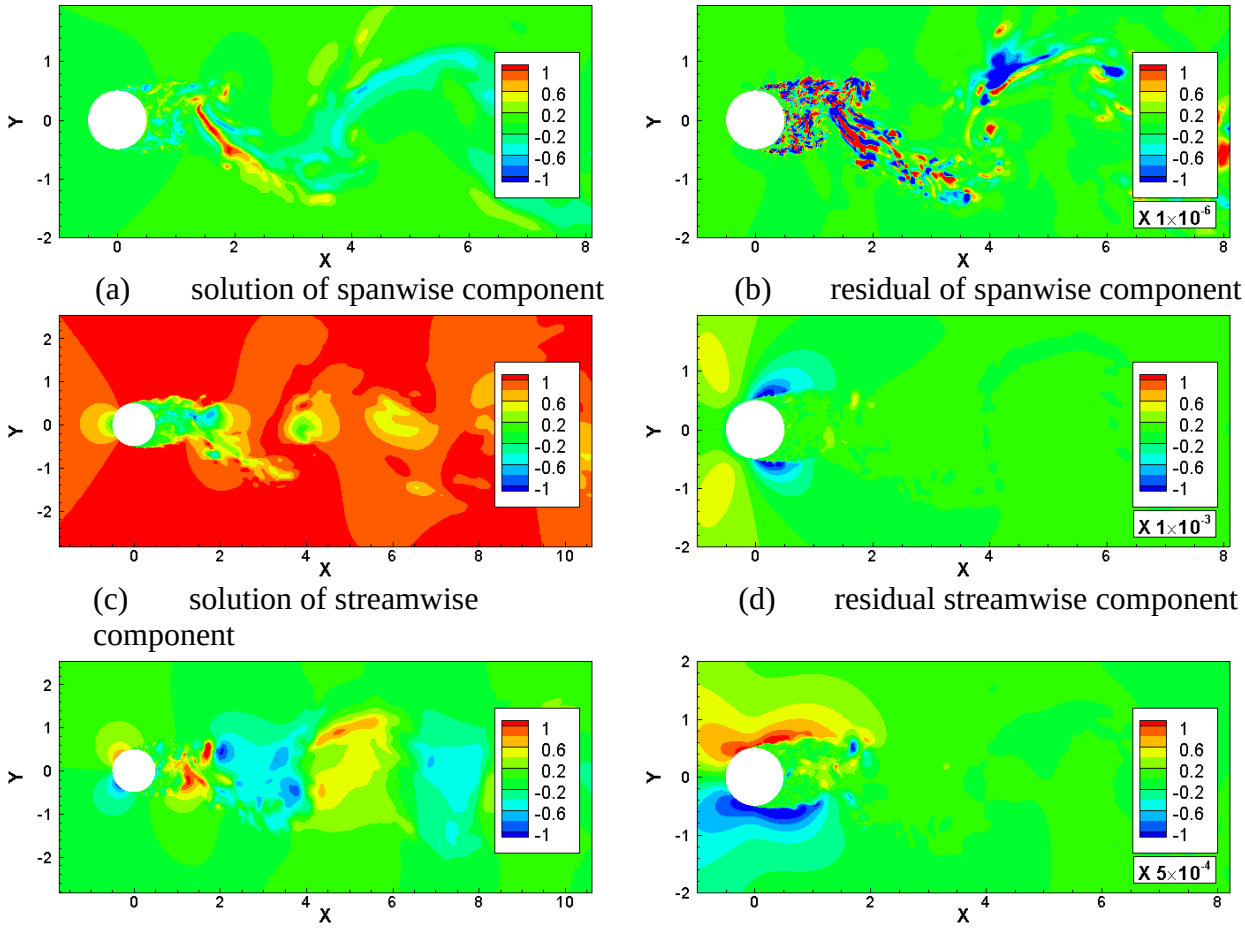

(a) solution of spanwise component

(b) residual of spanwise component

(c) solution of streamwise component

(d) residual streamwise component

(e) solution of transverse component

(f) residual of transverse component

Figure 4.2 Balance of momentum equations at Re=1.26x10^5

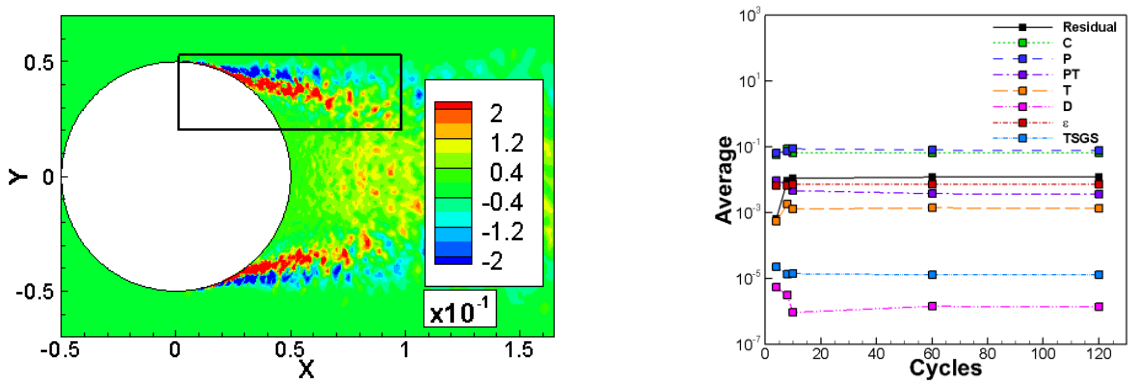

(a) (b)

Figure 4.3 Averaged TKE budgets: (a) contour of residual with test region and (b) variation with cycles for super-critical Re (Re=7.57x10^5)

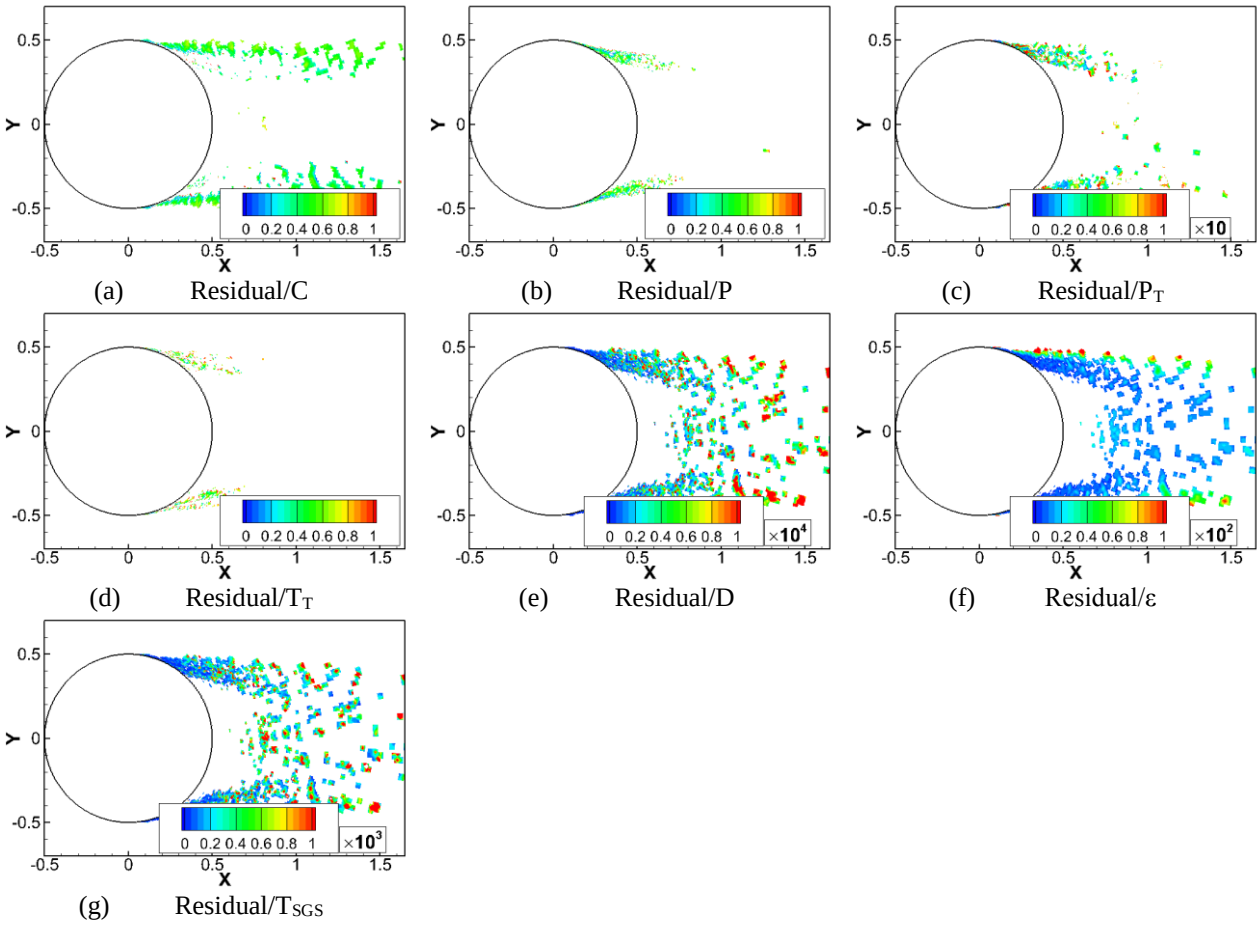

(a) Residual/C (b) Residual/P (c) Residual/P_T

(d) Residual/T_T (e) Residual/D (f) Residual/ε

(g) Residual/T_{SGS}

Figure 4.4 Ratio of residual to : (a) convection, (b) production, (c) pressure transport, (d) turbulent transport, (e) viscous diffusion, (f) viscous dissipation and (g) SGS transport

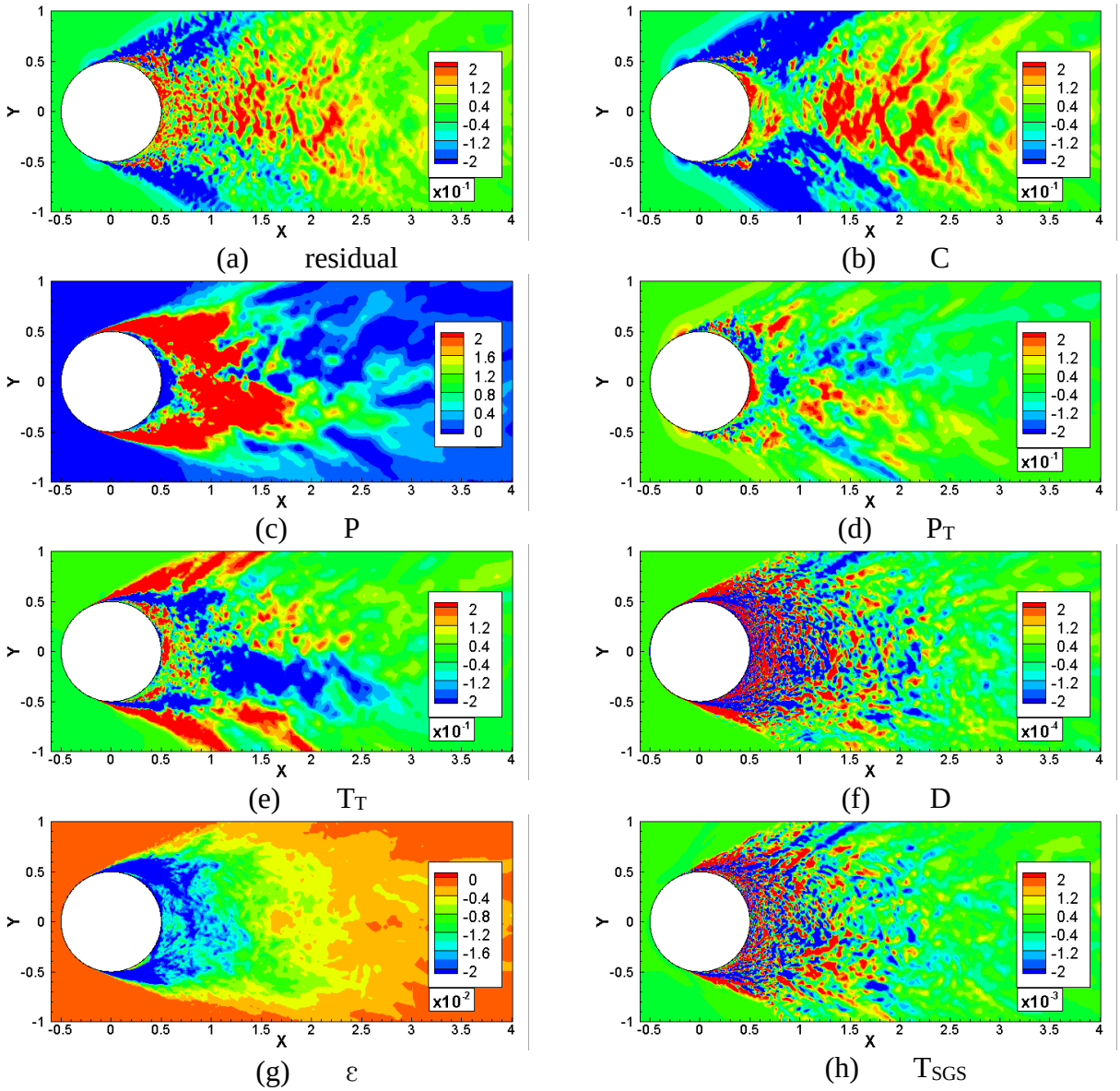

Figure 4.5 TKE budget at Re=1.26x10^5 with 10 cycles

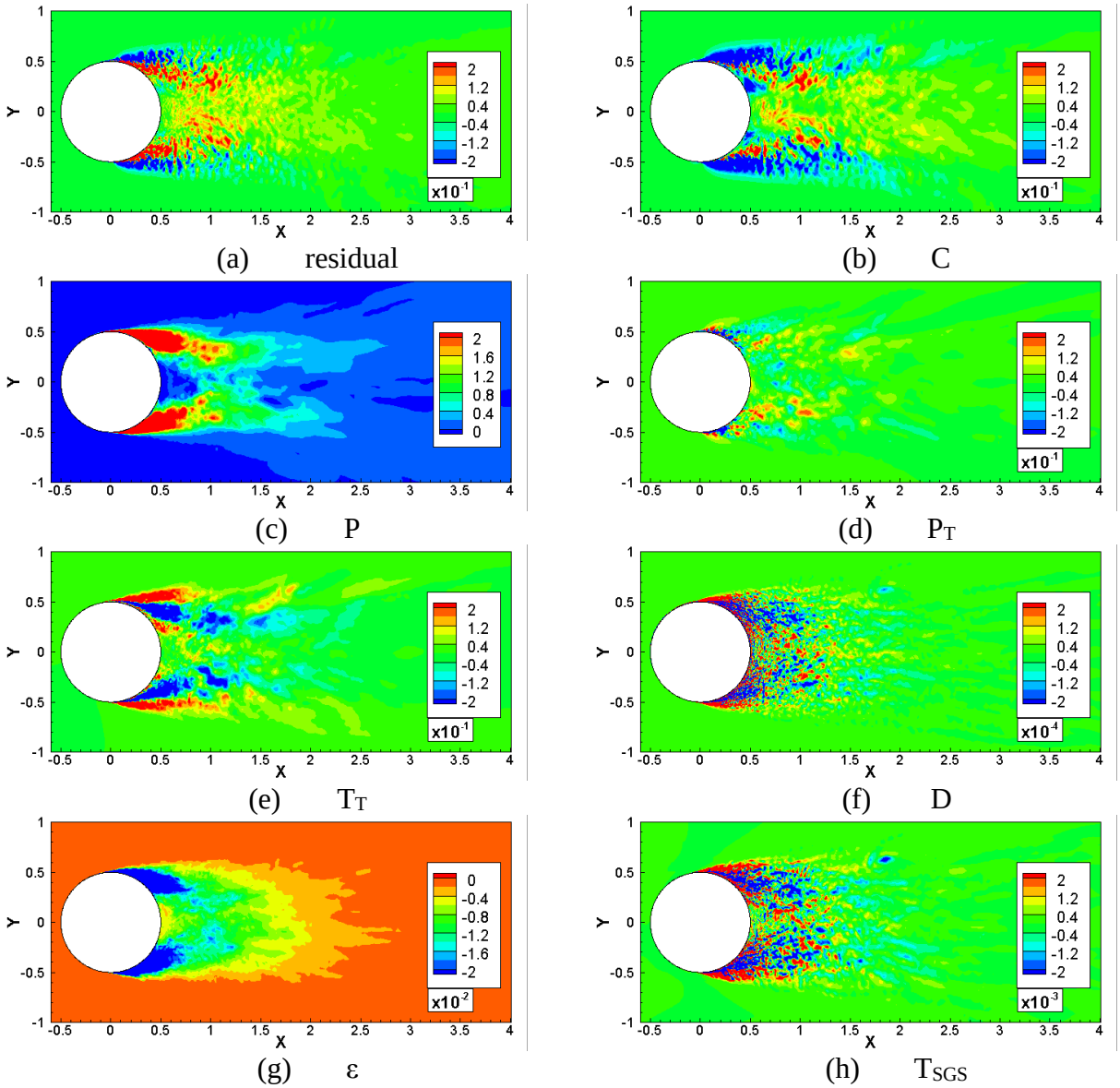

Figure 4.6 TKE budget at Re=2.52x10^5 with 10 cycles

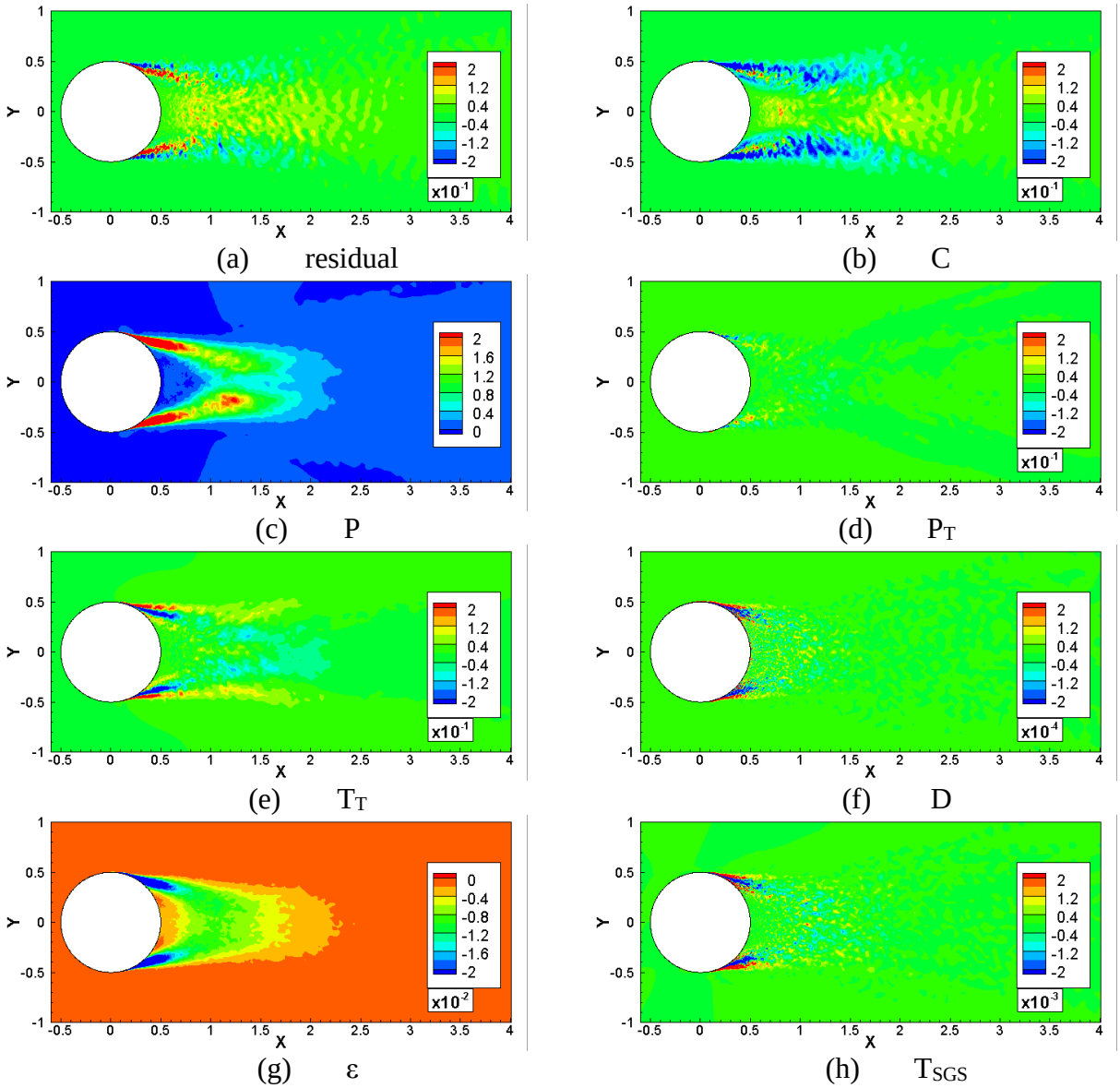

Figure 4.7 TKE budget at Re=7.57x10^5 with 120 cycles

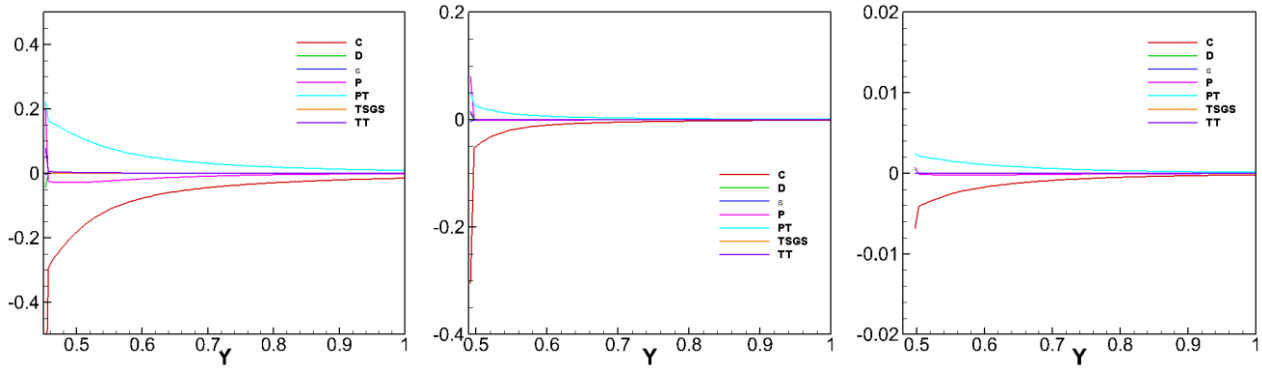

(a) Re=1.26x10^5 (b) Re=2.52x10^5 (c) Re=7.57x10^5

Figure 4.8 TKE budget distribution before LS

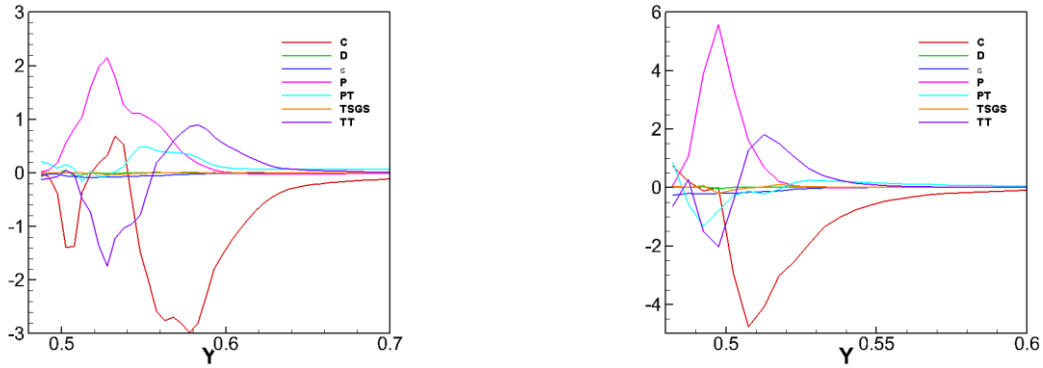

(a) Re=1.26x10^5 (b) Re=2.52x10^5

Figure 4.9 TKE budget distribution across shear layer for sub-, and critical Re

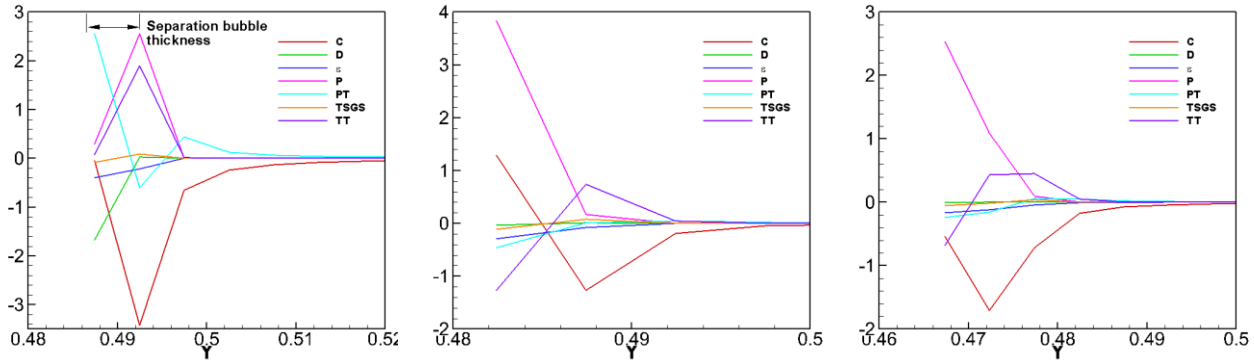

(a) TT (b) TR (c) TS

Figure 4.10 TKE budget distribution at key points for Re=7.57x10^5

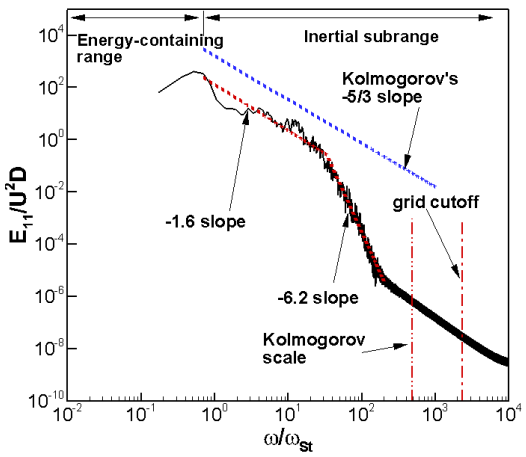

(a) Re=1.26x10^5

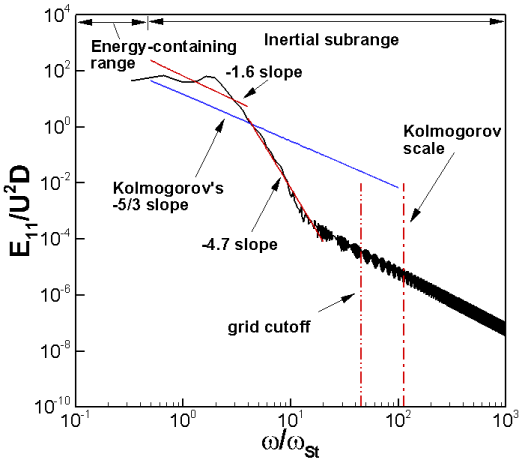

(b) Re=1.26x10^5

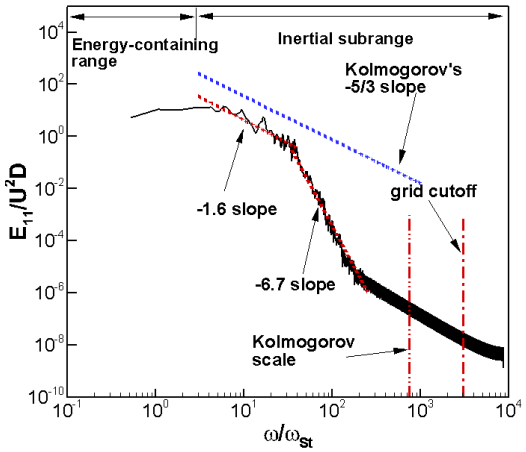

(c) Re=2.52x10^5

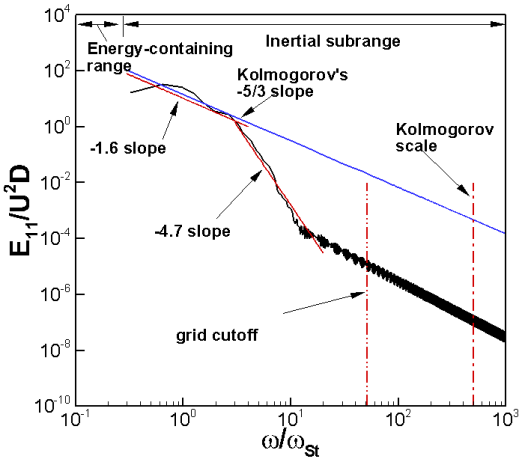

(d) Re=2.52x10^5

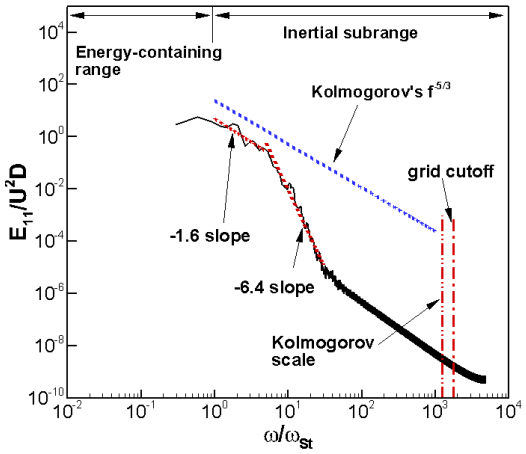

(e) Re=7.57x10^5

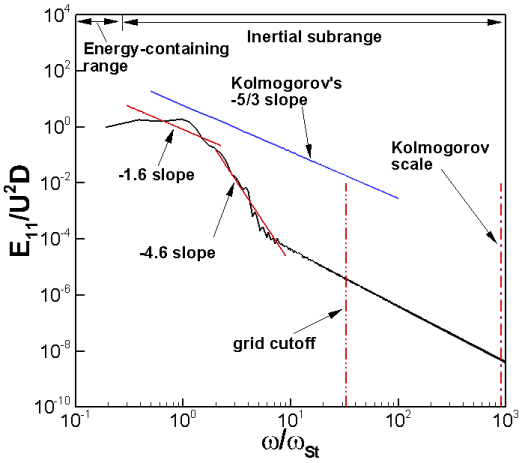

(f) Re=7.57x10^5

Figure 4.11 Energy spectra in the shear layer near the body (left) and 3D away from the cylinder center of the wake centerline (right)

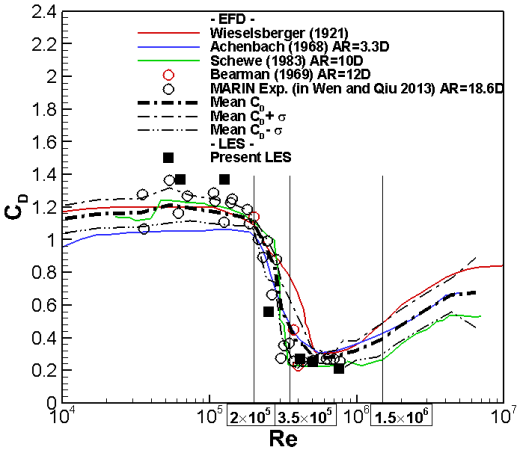

(a) C_D

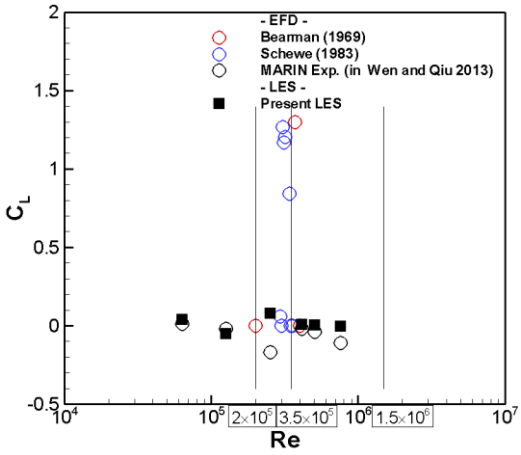

(a) Mean C_L

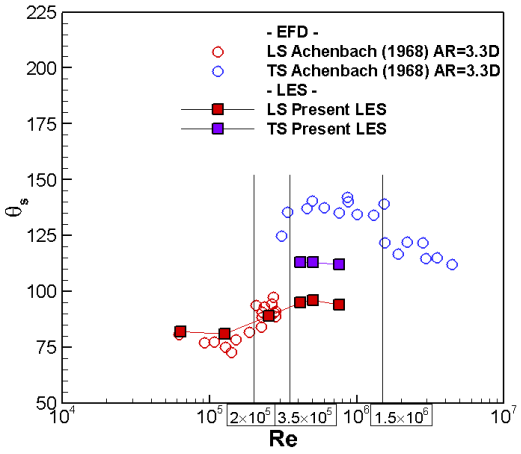

(b) θ_s

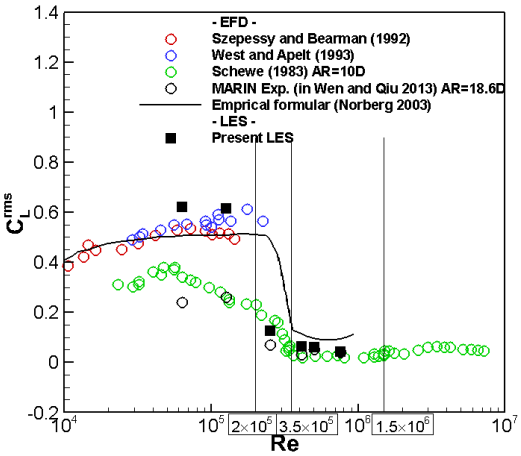

(b) C_L^{rms}

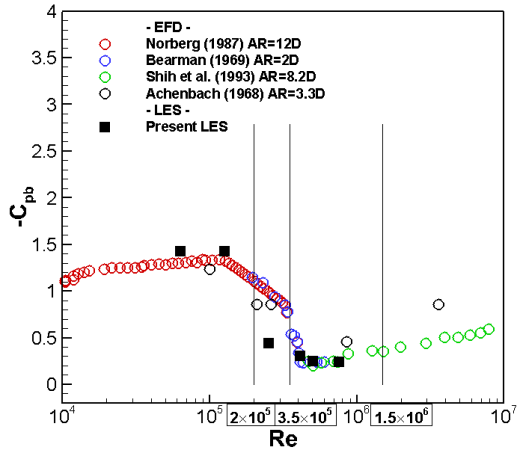

(c) $-C_{pb}$

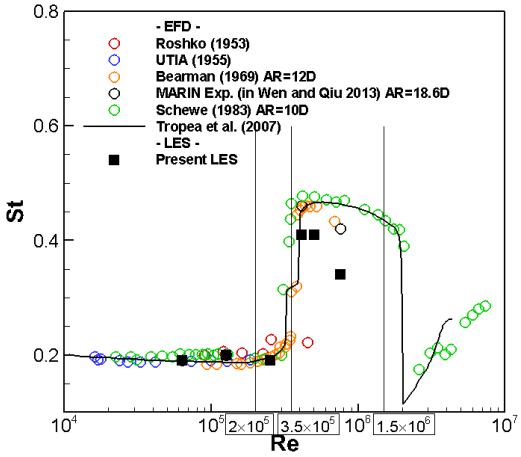

(c) St

Figure 4.12 Drag, separation angle and base pressure vs. Re

Figure 4.13 RMS lift coefficient and Strouhal number vs. Re

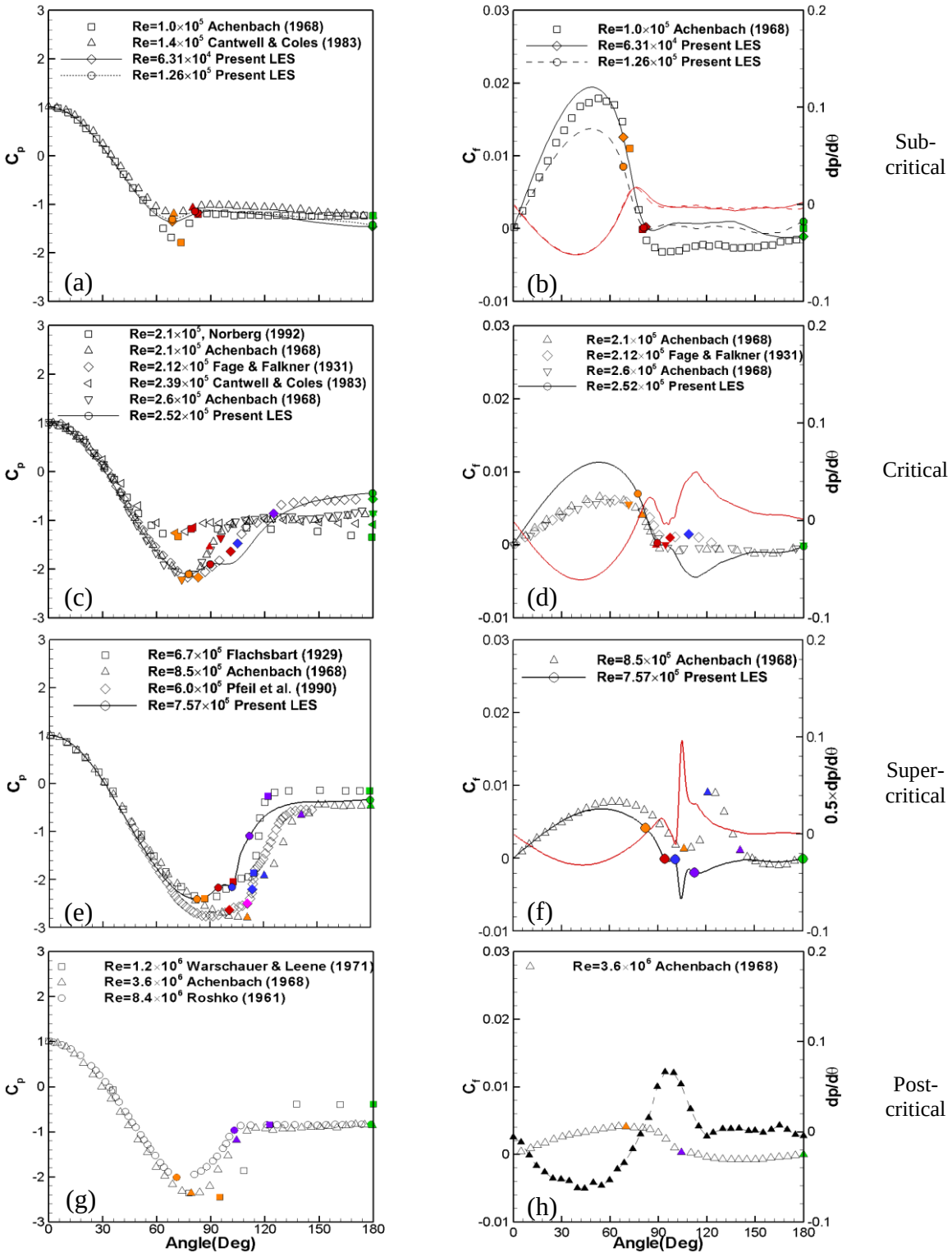

Figure 4.14 Pressure (left) and skin-friction with pressure gradient in red (right); orange=MP, red=LS, blue=TR, purple=TS and green=BP. The TR is corresponding to the end of the laminar separation bubble.

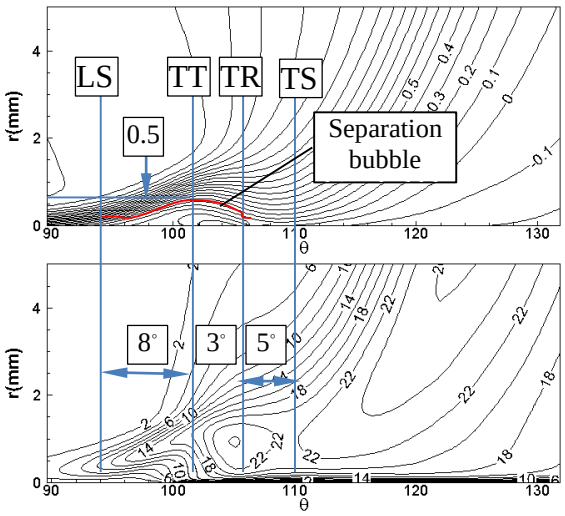

Figure 4.15 Mean velocity (top) and turbulence intensity (bottom) for Re=7.57x10^5

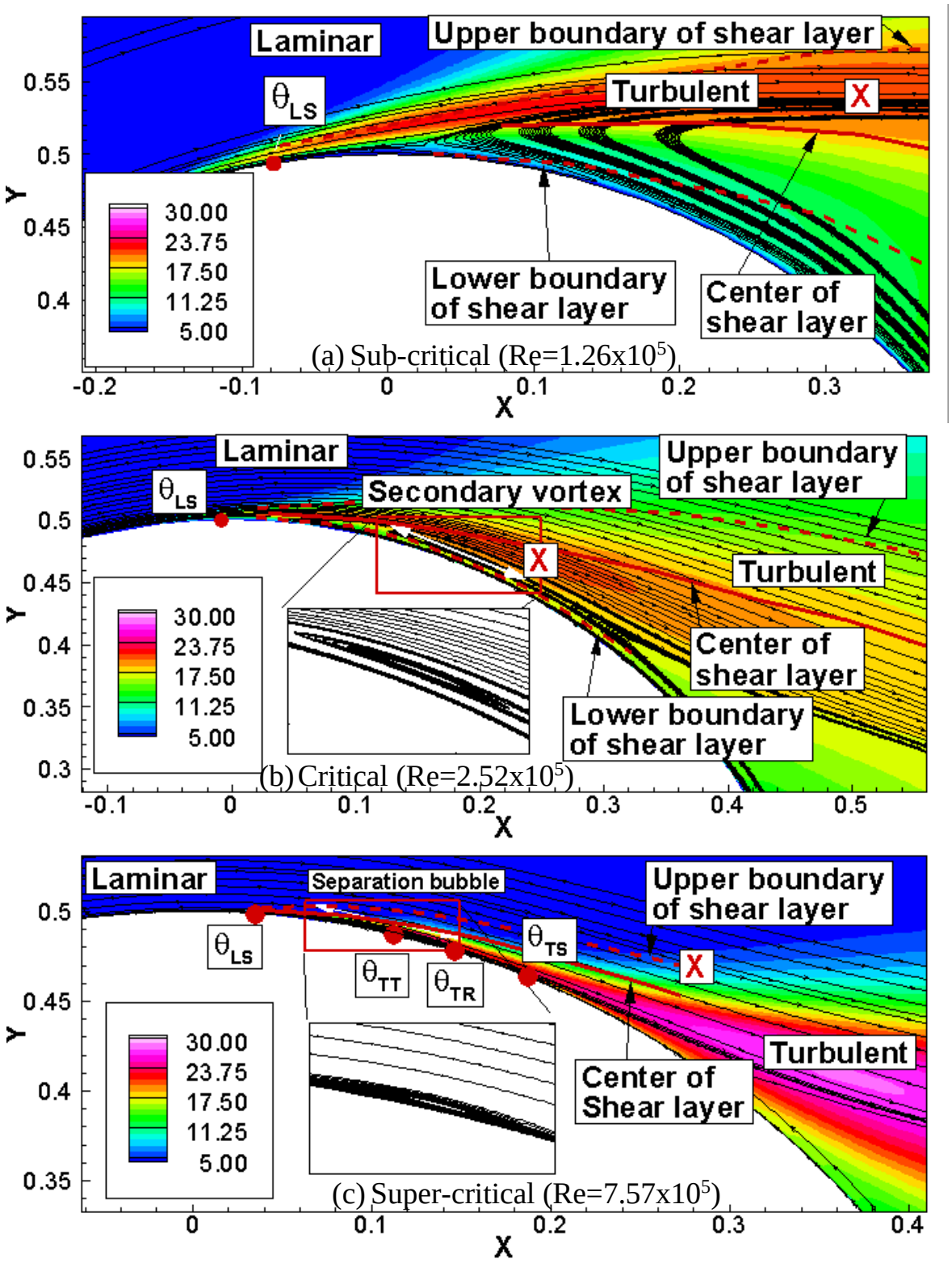

Figure 4.16 Turbulent intensity contour with stream line near separated flow

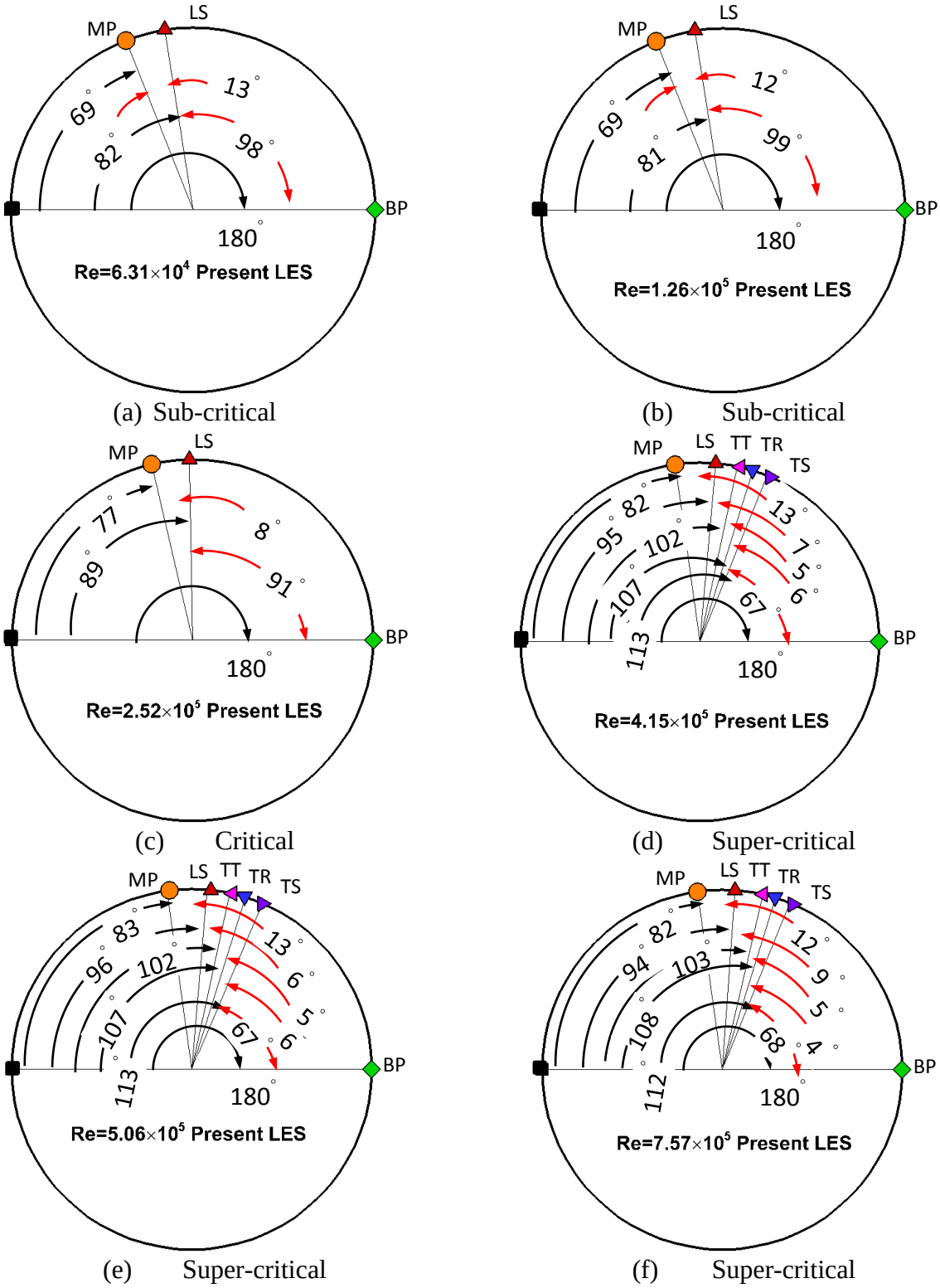

Figure 4.17 Present LES results of MP, LS, TR, TS and BP points on the cylinder; ●=MP, ▲=LS, ◀=TT, ▼=TR, ▶=TS and ◆=BP.

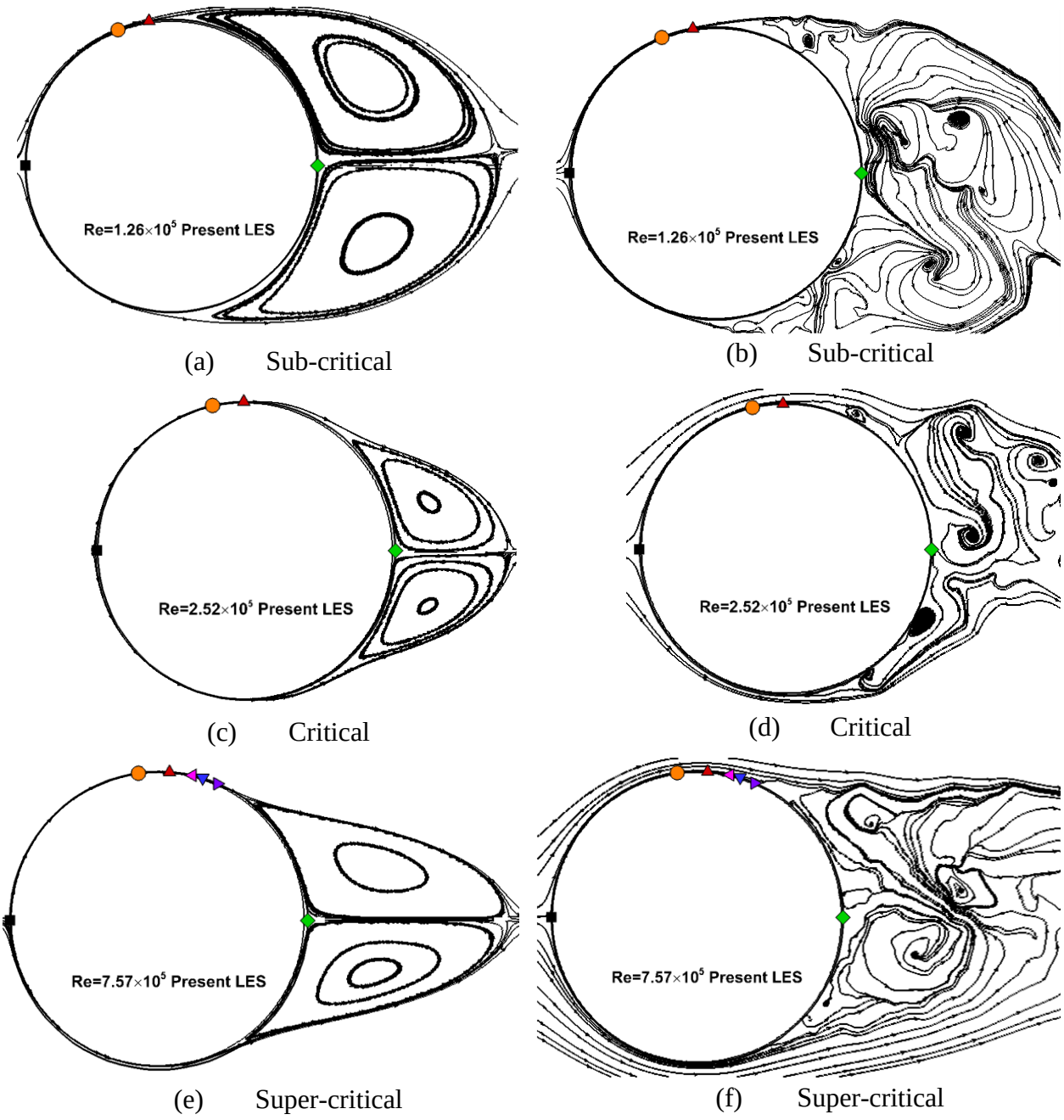

(a) Sub-critical (b) Sub-critical

(c) Critical (d) Critical

(e) Super-critical (f) Super-critical

Figure 4.18 Mean streamline (left) and instantaneous streamline (right); ●=MP, ▲=LS, ◀=TT, ▼=TR, ▶=TS and ◆=BP.

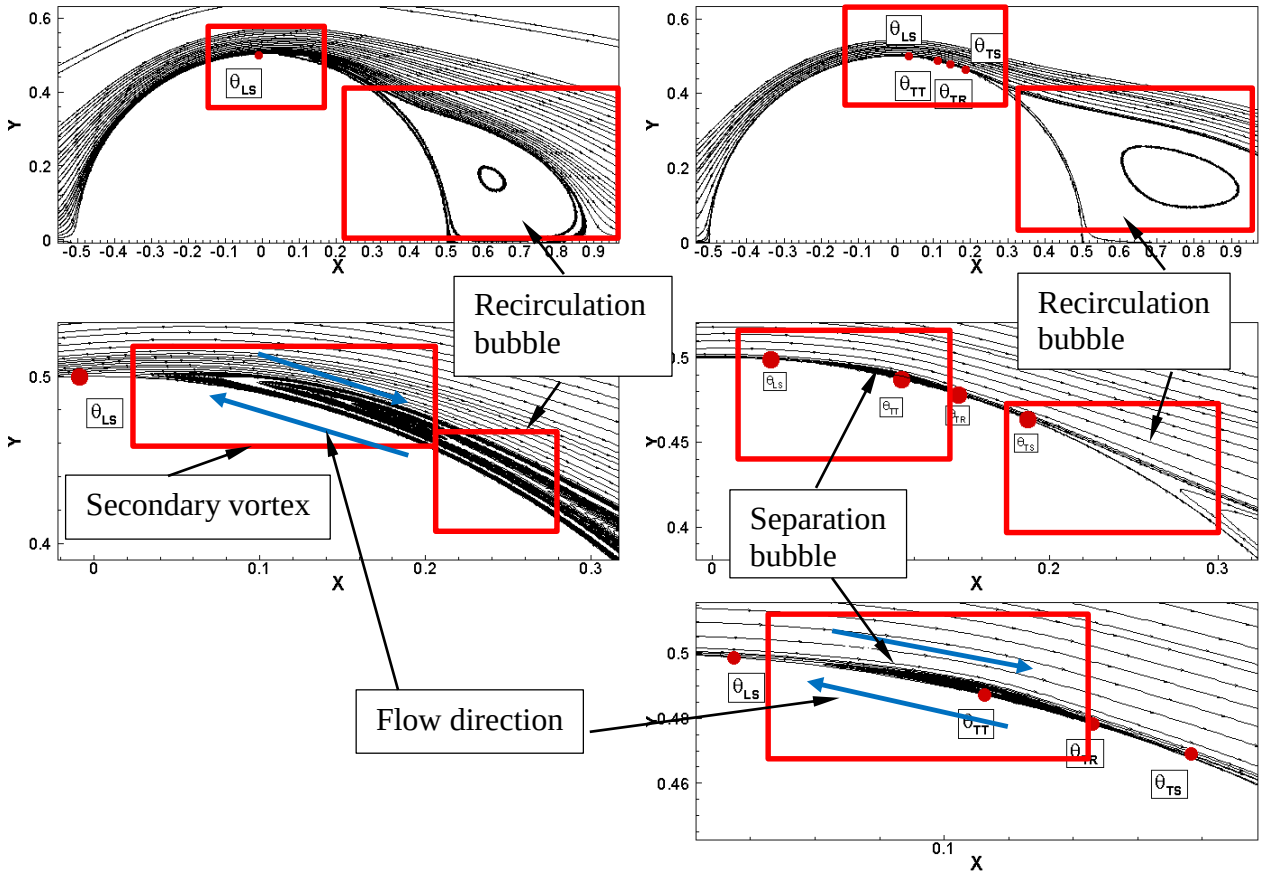

Figure 4.19 Mean streamline for critical (left) and super-critical (right) Re with key points

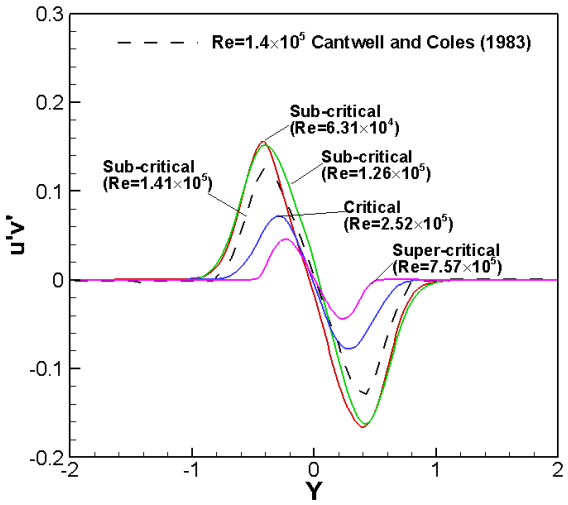

(a) Shear component along x=1

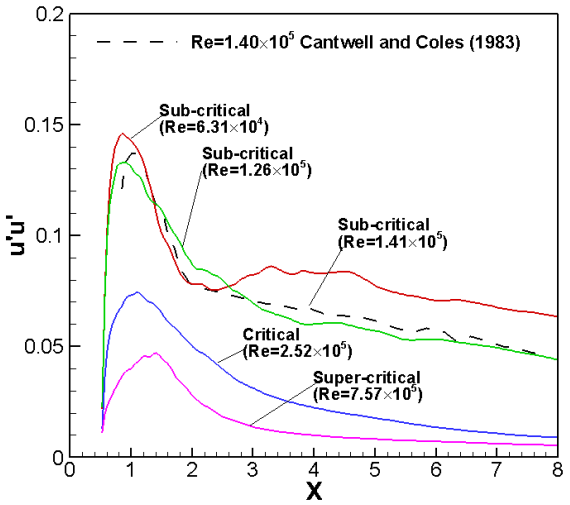

(b) Streamwise component along y=0

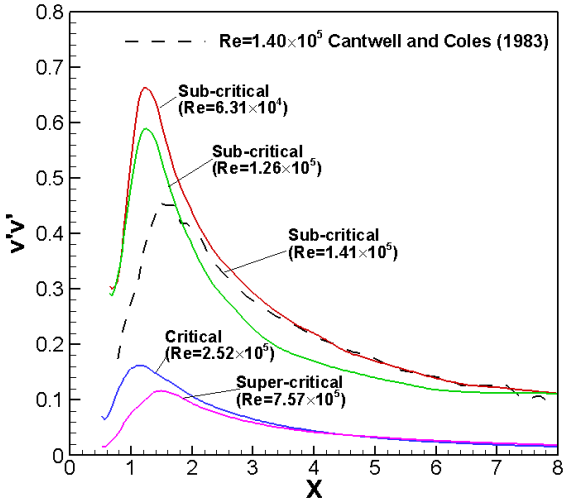

(c) Transverse component along y=0

Figure 4.20 Variation of Reynolds stresses with Re

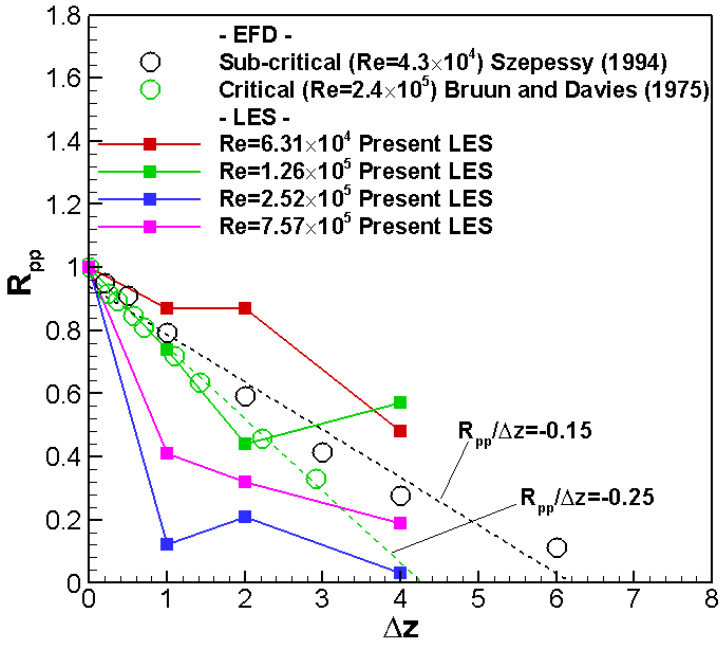

(a) Spanwise cross correlation of pressure against separation from midspan

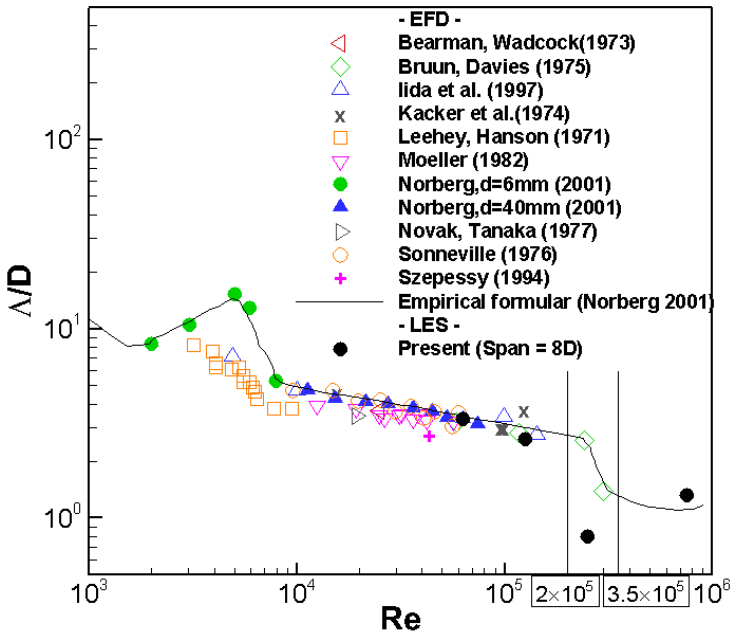

(b) Spanwise correlation length against Re

Figure 4.21 Comparison of correlation coefficient (a) and correlation length (b)

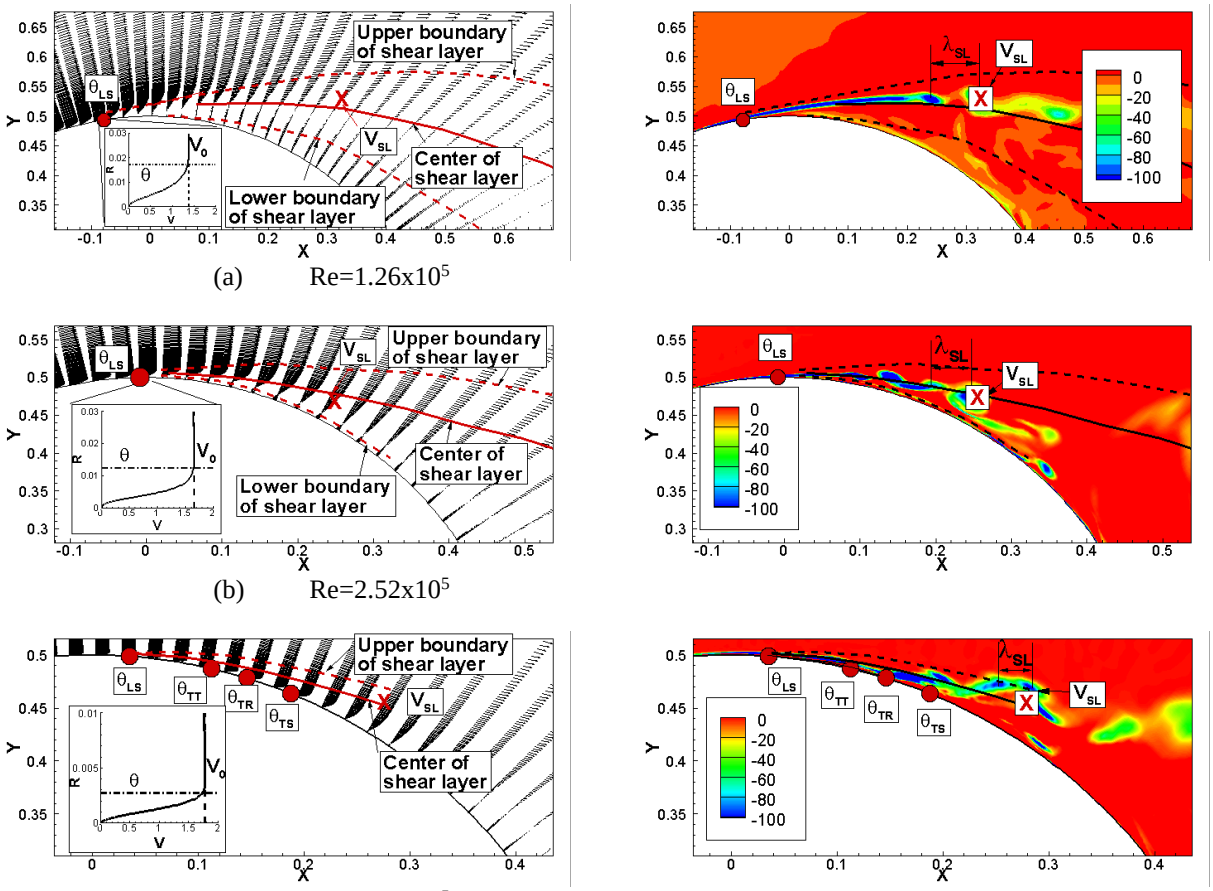

Figure 4.22 Mean velocity vector (left) and secondary vorticity contour (right). FFT analysis for shear layer and boundary layer is done at X mark

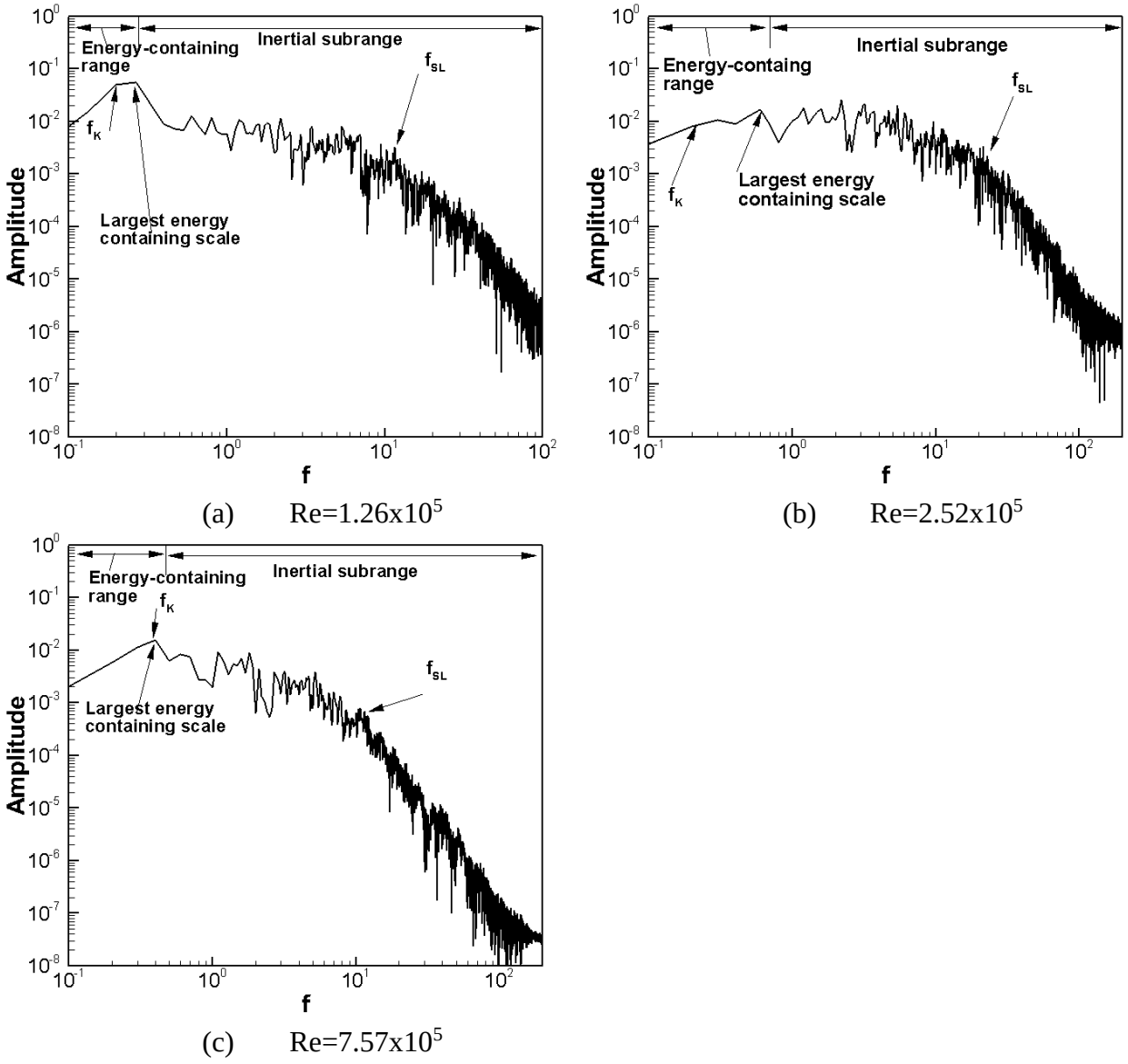

Figure 4.23 FFT analysis of streamwise velocity in shear layer

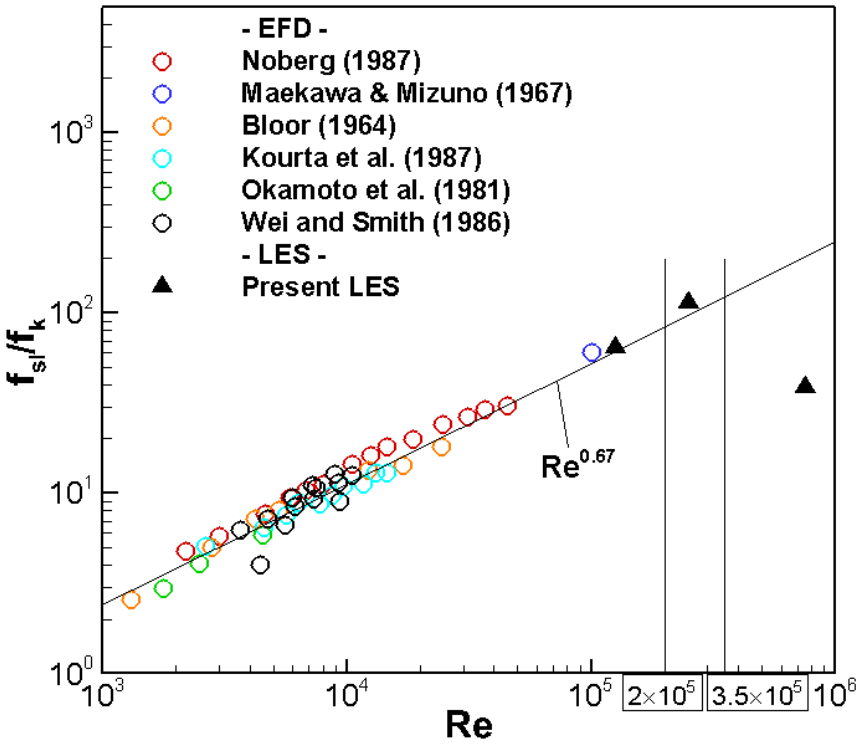

Figure 4.24 Normalized shear layer frequency

CHAPTER 5 ADDITIONAL DIAGNOSTICS

5.1 Basic flow features

Fig. 5.1 (a) and (b) show the mean streamwise and transverse velocity components for the sub-, critical and super-critical Re. The wake width is larger than the diameter of the cylinder and the flow separation is on the front of the cylinder for the sub-critical Re. The wake width is smaller than the diameter of the cylinder and the flow separation is much delayed on the back of the cylinder for the critical and super-critical Re. The wake length extends to about 1.5D for the super-critical Re and becomes shorter about 1.0D for the critical Re. The wake length is elongated to about 1.5D again for the super-critical Re. The main cause of the drag reduction is attributed to the delayed separation and reduced wake region.

Fig. 5.1 (c) shows the mean pressure for the sub-, critical and super-critical Re. Large pressure differences are observed between at the front stagnation and base points due to the wide wake width at the sub-critical Re. The pressure difference is small for the critical and super-critical Re due to the narrow wake width. Eventually, the small pressure difference leads to drag reduction.

Fig. 5.1 (d) shows the mean spanwise vorticity for the sub-, critical and super-critical Re. The shear layer amalgamates into the shedding vortices shortly after flow separation for the sub-critical Re. The shear layer becomes short and slightly develops along the cylinder wall for the critical Re. The shear layer elongates and retains its intensity farther downstream for the super-critical Re. The vorticity intensity indicates that the Karman shedding vortices are formed close to the cylinder for the sub-critical Re and farther downstream for the super-critical Re.

5.2 Reynolds Stresses and TKE in Wake

Fig 5.2 (a), (b) and (c) show the distribution of the Reynolds stresses for the sub-, critical and super-critical Re. The intensity of shear component in the shear layer is less than in wake for the sub-critical Re. As Re increases, the intensity increases and comparable to that in the wake. The intensity in the wake is very strong for the sub- and super-critical Re but very weak for the

critical Re. It implies that large shear motions of flows are focused in the wake for the sub-critical Re and both in the shear layer and wake for the super-critical Re. The strong intensity of streamwise component is observed in the shear layer for the sub-critical Re. As Re increases, the region of strong intensity extends to downstream. It implies that the main contribution to the shear layer is made by the streamwise component. The strong intensity of transverse component is observed in the wake 1D away from the cylinder for the sub- and super-critical Re. For the critical Re, the wake region loses its intensity and the shear layer has more intensity.

Fig 5.2 (d) shows the distribution of the TKE for the sub-, critical and super-critical Re. The TKE distribution has a large area with strong intensity in the wake 1D away from the cylinder for the sub-critical Re but the region moves to the shear layer for the critical Re. For the super-critical Re, the region returns to the wake but with narrow and lengthy shape.

5.3 Instantaneous flow features

Fig. 5.3 (a) and (b) shows the instantaneous velocity components for the sub-, critical and super-critical Re. The amplitude and size of the flow structure is large for the sub-critical Re and small for the critical and super-critical Re.

Fig. 5.3 (c) shows the instantaneous vorticity for the sub-, critical and super-critical Re. The shedding vortices are apparent and large structures are observed downstream for the sub-critical Re. The shedding is observed from x=1D due to the short recirculation region. The shedding vortices are observed farther downstream from x=1.5D for the critical and super-critical Re due to the elongated wake region.

Fig. 5.4 shows coherent flow structures visualized with iso-surface of Q criterion (Hunt 1988). The level of the non-dimensionalized eddy viscosity ν_t/ν is overlaid on the flow structures to show turbulent level. Large-scale, anisotropic flow structures are observed in the wake for the sub-critical Re. The amplitude of the shedding is large for the sub-critical Re and become smaller as Re increases. The level of the non-dimensionalized eddy viscosity shows that the flows

remain laminar before the separation and the transition occurs in the free shear layer. The separation points move downstream as Re increases.

5.4 Instabilities in Separation Bubbles

Fig. 5.5 shows the instantaneous velocity profile and secondary vorticity near the body for the critical and super-critical Re along with analysis points along the wall. An X mark downstream indicates the analysis point for the shear layer near the body and show how far the point is from the key points. The sub-critical Re is not considered because no secondary vortex or separation bubble near the body are observed in the mean streamline as shown in Fig. 4.16. Since it is not clear to locate specific analysis points for the separation bubble as in chapter 4, LES solution files are used instead of time history at an analysis point. As a result, the spectral analysis is rough and the frequency range does not cover the wide range of inertial subrange as in the FFT analysis for the shear layer. The solution files are written every 200 time steps with a constant time step $\Delta t=1x10^{-4}$ so the time interval between files is $2x10^{-2}$. About 780 files are used for the analysis, which cover 5 Karman vortex shedding cycles. The FFT analysis is applied to 243 locations; 9 locations along the circumferential direction denoted by x marks and 27 points in radial direction as shown in Table 5.1 and the bottom of Fig 5.5. In radial direction, the points are picked up to the maximum thickness of separation bubble r_{SB}.

The instantaneous velocity profiles have inflection points in the separation bubble for the critical and super-critical Re, which implies the formation of secondary vortex between the body and shear layer. The transition point of the shear layer, the first occurrence of shedding, moves upstream as Re increases. The mean center of shear layer becomes close to the cylinder wall as Re increases. Fig. 5.6 shows enlarged view around the secondary vortex and separation bubble regions, respectively. Streamlines show the formation of the secondary vortex near the body for the critical and super-critical Re. For the critical Re, the secondary vortex is moving along the cylinder and joins to the wake. A distance to the mean center of shear layer is measured from the first occurrence of secondary vortex; 0.01D for the critical Re and 0.003D for the super-critical

Re. As Re increases, the mean center of shear layer becomes close to the separation bubble. The movement of the shear layer to the wall increases chance to interact with boundary layer. As a result, the boundary layer is mixed with the shear layer for the super-critical Re. This mixing of two layers results in the reattachment of the separated flow and forms the separation bubble as Re increases.

Fig. 5.7 shows the energy spectra of streamwise velocity before the separation bubble and across separation bubble. The highest frequency range is about 25 due to the coarse time interval. The grid cutoff near the separation bubble is way beyond the frequency range and not shown in the figures. Frequency range is used in order to make the comparison with f_K and f_{SL} easy instead of wavenumber. The spectra show similar distribution in radial direction and just have increasing amplitude range. Significant differences are found along the cylinder wall, especially before and across the separation bubble region. Thus, spectra before and across the separation bubble are discussed. Due to the low frequency resolution, the dissipation in the inertial subrange by the upwind scheme is not observed in the spectra. For the spectra before the separation bubble, the scaling exponent is close to the Kolmogorov's slope and only a frequency peak close to f_K is found. For the spectra across the separation bubble, the scaling exponent is following the Kolmogorov's slope as well. In addition to the frequency peak close to f_K, distinct frequencies are observed at about 18 and 15 that are close to f_{SL} captured by FFT for the critical and super-critical Re, respectively. The frequencies are observed in any region including TR and TS. Both the similarity of frequencies in the separation bubble to f_{SL} and the proximity between the shear layer and boundary layer indicate that the interaction of separation bubble and shear layer instabilities.

5.5 Flow Structure Analysis with POD Method

In order to compute fluctuating velocity components, 500 solution files for the sub- and critical Re and 300 files for the super-critical Re are used. The files cover about 10 Karman vortex shedding cycles. Fig. 5.8 shows the analysis regions of POD in the flow field. The regions

consist of three parts, boundary layer, shear layer and wake regions. Flow structures associated with the instabilities including the boundary layer, shear layer and the Karman shedding vortices are extracted by the snapshot POD method.

Figure 5.9 shows the relative kinetic energy distribution computed by the POD eigenvalues. Large eigenvalue represents large coherent flow structures. Fig. 5.9 (a) is for the boundary layer for the sub-, critical and super-critical Re. As mentioned before, two distinct POD modes should appear and form a pair if coherent flows exist, e.g. Karman shedding vortices. In this regard, the first mode for the sub-critical Re is not related to coherent flow structures despite high magnitude. For the critical Re, first 4 modes have similar magnitude but overall uniform distribution is observed. The uniform distribution with small magnitude indicates that flow structures with small-scale are mixed in the field and hard to separate them. For the super-critical Re, first two modes are relatively dominant, which implies the existence of distinguishable coherent flow structures. Fig. 5.9 (b) is for the shear layer for the sub-, critical and super-critical Re. For the sub-critical Re, first two modes are distinctive and might be related to coherent flow structures. For the critical and super-critical Re, the modes are evenly distributed indicating hard to distinguish any coherent flow structures. The main cause of the uniform distribution is weak turbulent kinetic energy distributions in the regions. Fig. 5.9 (c) is for the wake for the sub-, critical and super-critical Re. For the sub- and super-critical Re, first two dominant modes are definitely distinctive and take a large fraction of the total kinetic energy. Thus, these two mode are likely to be correlated with large coherent flow structures. For the critical Re, there are no dominant modes indicating no large distinguishable flow structures. This distributions are consistent with the TKE distribution in the wake as shown in Fig. 5.2 (d).

Figs 5.10 and 5.11 show the flow structures in the boundary layer of POD modes. Fig. 5.10 is for the streamlines at midspan for sub-, critical and super-critical Re. As expected, no flow structures including vortical structures are observed for the sub-critical Re and the streamlines resemble mean flow. For critical Re, the small vortices are formed near the body and shedding along the cylinder wall. For super-critical Re, a single vortex is observed and the

location is almost fixed in one location. Fig. 5.11 shows three-dimensional flow structures by iso-surface of the Q criterion; the red color code means counter clockwise spanwise vorticity and the blue color code means clockwise spanwise vortices. For sub-critical Re, no three-dimensional flow structures are observed. For critical Re, the shedding of the small-scale vortices along the cylinder wall is shown and alternatively rotating flow structures appear in spanwise direction. Similar flow patterns are observed in higher modes. Main cause is due to the weak kinetic energy distribution. Thus, it is not easy to extract clearer flow structures. For super-critical Re, two dimensional flow structures are clearly observed and indicates that the laminar separation bubbles are spread in almost same location in spanwise direction.

Figs 5.12 and 5.13 show the flow structures in the shear layer. Fig. 5.12 is for streamlines at midspan for sub-, critical and super-critical Re. For sub-critical Re, the first two modes contain some part of flow structures in wake. Since the TKE in the shear layer is smaller than in the wake, the first two modes represent the flow structures in the wake instead of the shear layer although small-scale flow structures are observed in the shear layer. In higher modes, only small-scale flow structures are observed. For the critical Re and super-critical Re, small-scale flow structures are observed through all the POD mode and hard to recognize any coherent flow structures due to the small TKE distribution. Fig. 5.13 shows three-dimensional flow structures by iso-surface of the Q criterion. As shown in the streamlines, the flow patterns are chaotic and hard to recognize any coherent flow structures.

Figs 5.14 and 5.15 show the flow structures in the wake. Fig. 5.14 is for streamlines at midspan for sub-, critical and super-critical Re. For sub-critical Re, large vortical structures are observed and the topologies of the first two modes are in agreement with other studies in the wake of a circular cylinder (Deane et al., 1991; Ma et al., 2000; Perrin et al., 2007). The two modes form pairs with a shift in the streamwise direction and the length of the shift is a quarter of the wavelength λ. A quarter of λ corresponds to the phase shift angle of 90 degree. The frequency of the flow structures is estimated with the use of the wavelength λ and incoming velocity U_∞. The estimated frequency is about 0.19 and corresponds to the Karman shedding

frequency, f_K as shown in Table 5.2. Therefore, the first two modes represent the alternating vortex shedding in the wake. For critical Re, the Karman shedding like flow patterns are observed in some POD modes. The two modes forming pairs with a shift in the streamwise direction show shedding frequency close to f_K of 0.19. For super-critical Re, the first two modes clearly form pairs with a shift in the streamwise direction. The estimated frequency is about 0.374 and corresponds to the f_K. Fig. 5.15 shows three-dimensional flow structures by iso-surface of Q criterion. For sub-critical Re, two-dimensional alternating flow structure is observed. For critical Re, the flow pattern is chaotic and no three-dimensional coherent flow structures are observed. It implies that the flow structures with wide range of scales are mixed in the wake for the critical Re. The result is consistent with broadband of frequency of FFT of lift coefficient for the critical Re. For super-critical Re, the two-dimensional coherent flow structures are observed and form alternating vortex shedding patterns.

5.6 Conclusions

The mean velocity and vorticity distributions showed the change of wake region. Wake width became narrow as Re increased due to the delayed separation. The wake length for the critical Re became slightly shorter than that for the sub-critical and recovered for the super-critical Re. The mean pressure distribution showed that small pressure differences for the critical and super-critical regime led to drag reduction.

The Reynolds stresses and TKE distributions showed different behavior with flow regimes. Overall distributions were similar for the sub- and super-critical Re but became narrow and lengthy with increasing Re. For the critical Re, most of the distributions were concentrated around shear layer. It implies that flow structures for the sub- and super-critical have similarity, e.g., Karman shedding vortices.

Instantaneous flow features including velocity and three-dimensional flow structures showed the development of flow structures in wake. The flow structures for the sub-critical Re were anisotropic and the vortices were shedding with large amplitude. The flow structures for the

critical and super-critical Re were small and chaotic. The vortices were shedding with small amplitude.

The formation of the separation bubbles was studied with streamlines and secondary vortices. The close distance between boundary layer and shear layer generated the secondary vortex moving along the cylinder wall for the critical Re. Due to the upstream movement of transition point of the shear layer and the energetic mixing as Re increases, the secondary vortex were confined in a limited region and form the separation bubble for the super-critical Re. The influence of the shear layer to the boundary layer was studied by the spectra of streamwise velocity with crude data samples. Significant different behavior and a sharp frequency peak except for the Karman shedding frequency were only found across the separation bubble regardless of locations in radial direction. The similarities of the frequencies to the shear layer instabilities indicated that the proximity between the shear layer and boundary layer induced the secondary vortex and mixing between shear layer and boundary layer for the critical and super-critical Re.

The snapshot POD method was employed to recognize coherent flow structures in the boundary layer, shear layer and wake. Due to the weak TKE distribution, it was hard to extract clear coherent flow structures in the boundary layer, especially for the sub-critical and critical Re. Secondary vortices shedding along the wall were observed with relatively large flow structures alternatively appearing in spanwise direction for the critical Re. A secondary vortex formed a bubble instead of shedding along the wall for the super-critical Re. The flow patterns associated with the bubble formed a two dimensional flow structure in spanwise direction. Due to the weak TKE distribution, clear flow structures were not extracted and hard to recognize specific coherent flow structures for the shear layer region. Two dimensional vortical structures were found in the wake and associated with alternating shedding vortices for the sub- and super-critical Re. The estimated frequency from the topologies agreed with the Karman shedding frequency. No coherent flow structures were found for the critical Re, which was consistent with the absence of the large TKE structure in the wake.

Spectral analysis and snapshot POD method were applied to the present LES study. Due to the wide range containing separation bubble, the coarse data samples was used and spectral analysis just covered the shear layer instability. The snapshot POD method successfully captured flow patterns in the boundary layer and wake. Due to the narrow boundary layer, weak TKE distribution, ambiguity of the physical boundary of the regions including boundary layer, shear layer and wake, it was hard to separate and study solely the specific regions, especially boundary layer and shear layer and only small-scale and chaotic flow structures were obtained.

5.7 References

1. Deane, A. E., I. G. Kevrekidis, G. E. Karniadakis and S. A. Orszag (1991). Low-dimensional models for complex geometry flows: Application to grooved channels and circular cylinders. Physics of Fluids A: Fluid Dynamics, AIP Publishing. **3:** 2337-2354

2. Hunt, J., A. A. Wray and P. Moin (1988). Eddies, streams, and convergence zones in turbulent flows. Studying Turbulence Using Numerical Simulation Databases, 2. **1:** 193-208

3. Ma, X., G. S. Karamanos and G. E. Karniadakis (2000). Dynamics and low-dimensionality of a turbulent near wake. Journal of Fluid Mechanics, Cambridge University Press. **410:** 29-65

4. Perrin, R., M. Braza, E. Cid, S. Cazin, A. Barthet, A. Sevrain, C. Mockett and F. Thiele (2007). Obtaining phase averaged turbulence properties in the near wake of a circular cylinder at high Reynolds number using POD. Exp Fluids. **43:** 341-355

Table 5.1 Analysis points (circumferential and radial direction) across the separation bubble for FFT analysis.

Re	θ (deg)	r/r_{SB}	f_{SB}
$2.52x10^5$	88-110 (9 points)	1-108% (27 points)	18.1
$7.57x10^5$	95-117 (9 points)	1-103% (27 points)	15.7

Table 5.2 Karman vortex shedding frequency from POD results

	Re ($x10^5$)	f_K (FFT)	f_K (POD)	U_∞	λ
Sub-critical	1.26	0.19	0.19	1.0	5.079
Critical	2.52	0.19	0.19	1.0	4.051
Super-critical	7.57	0.34	0.34	1.0	2.671

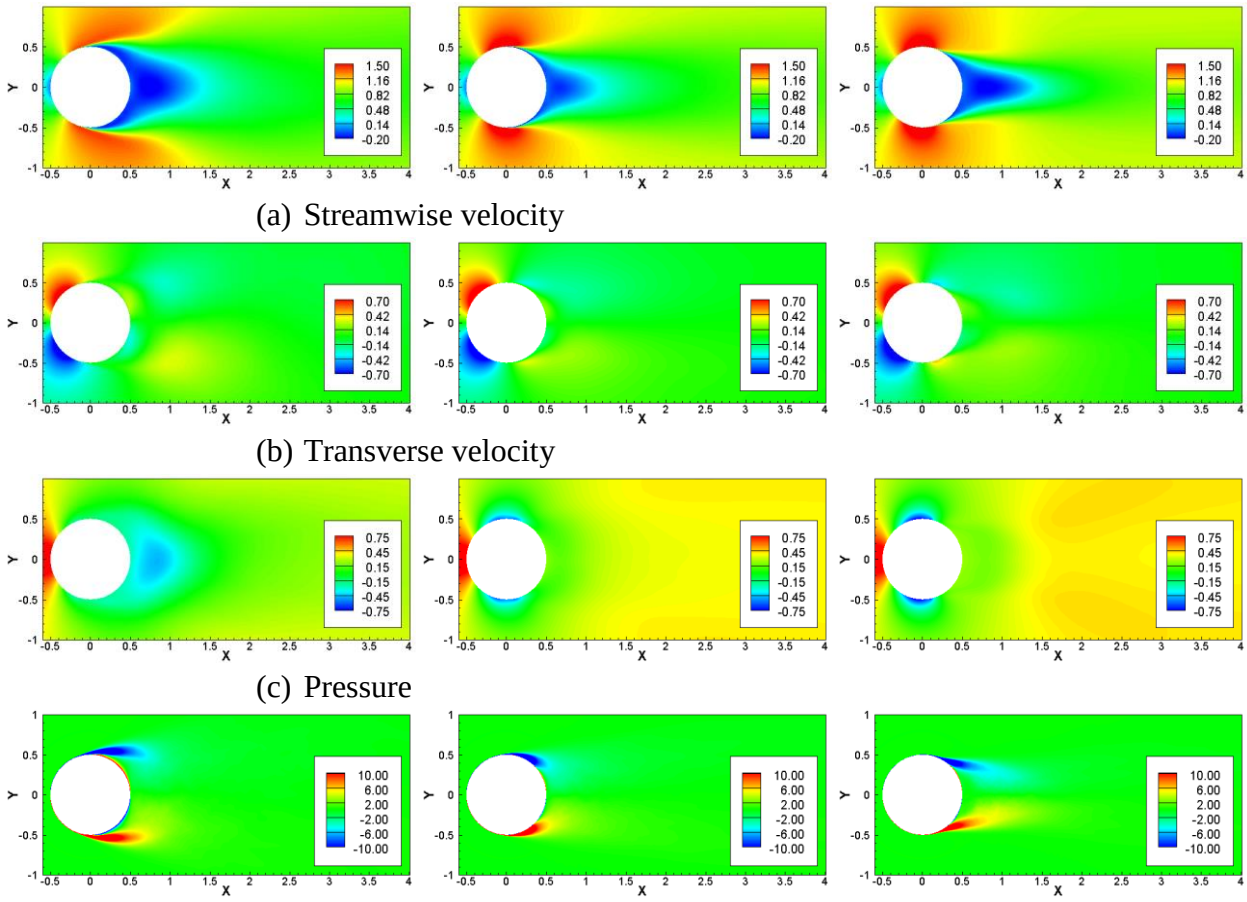

(a) Streamwise velocity

(b) Transverse velocity

(c) Pressure

(d) Spanwise vorticity

Figure 5.1 Mean flow features: sub-critical ($Re=1.26x10^5$) (left), critical ($Re=2.52x10^5$) (middle) and super-critical ($Re=7.57x10^5$) (right)

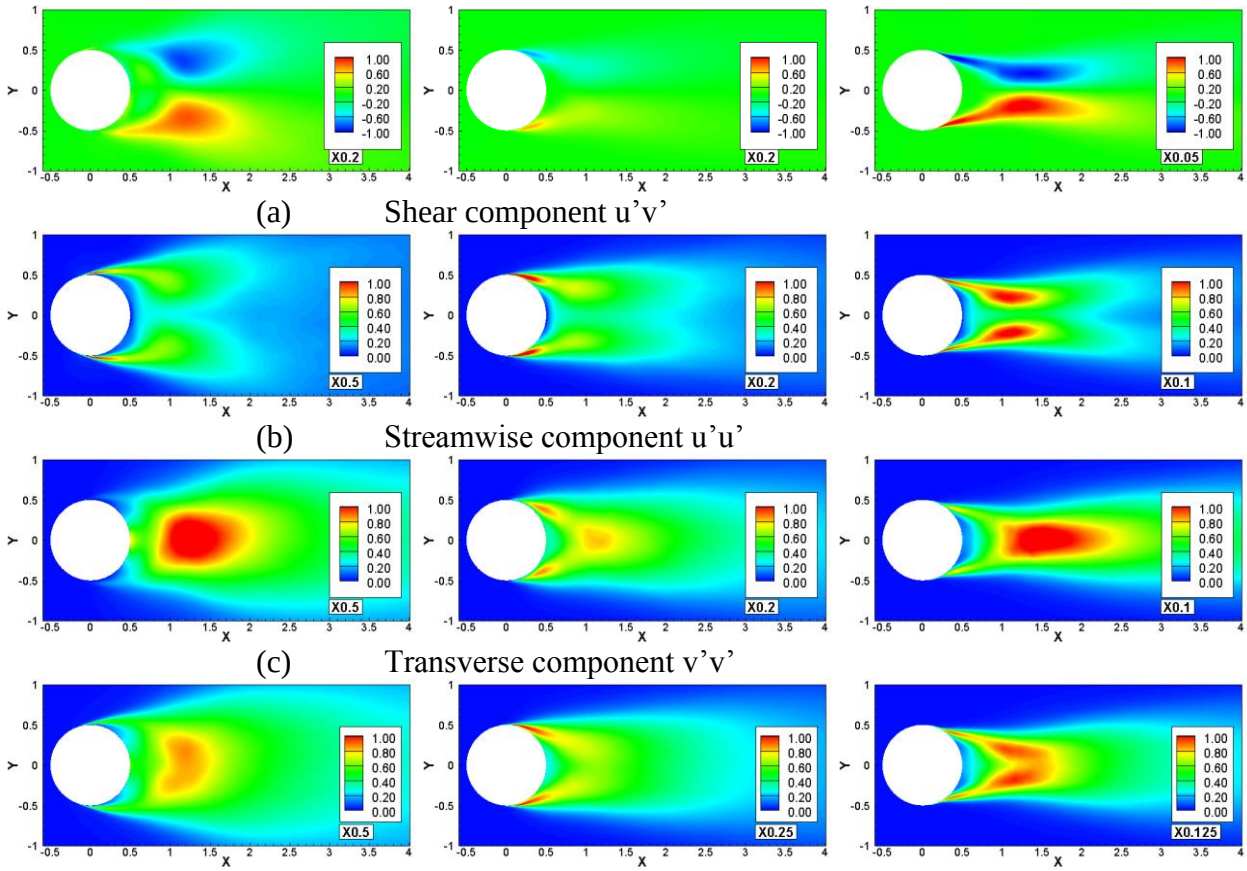

Figure 5.2 Reynolds stresses and resolved turbulent kinetic energy: sub-critical ($Re=1.26x10^5$) (left), critical ($Re=2.52x10^5$) (middle) and super-critical ($Re=7.57x10^5$) (right)

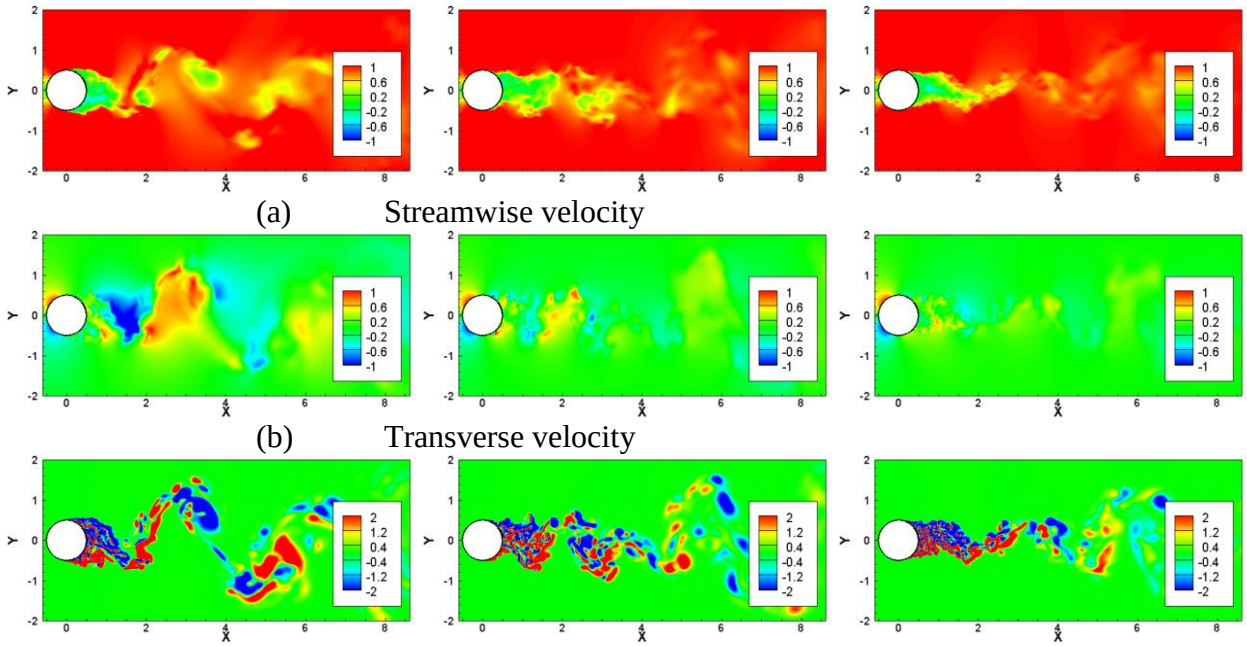

Figure 5.3 Instantaneous flow features: sub-critical ($Re=1.26x10^5$) (left), critical ($Re=2.52x10^5$) (middle) and super-critical ($Re=7.57x10^5$) (right)

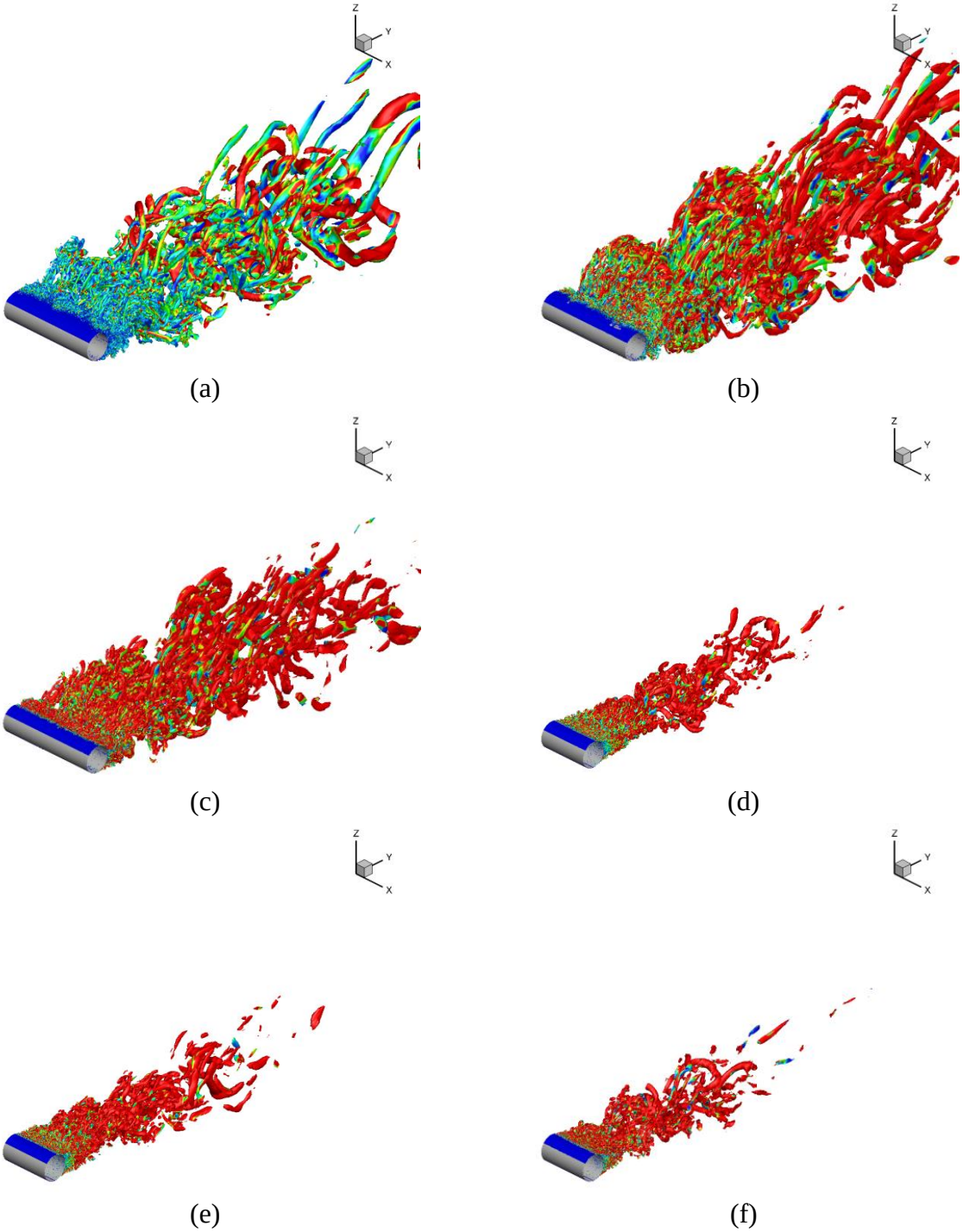

Figure 5.4 Vortex structure with Q-criterion: (a) sub-critical ($Re=6.31x10^4$) (b) sub-critical ($Re=1.26x10^5$), (c) critical ($Re=2.52x10^5$) (d) super-critical ($Re=4.15x10^5$), (e) super-critical ($Re=5.06x10^5$) and (f) super-critical ($Re=7.57x10^5$)

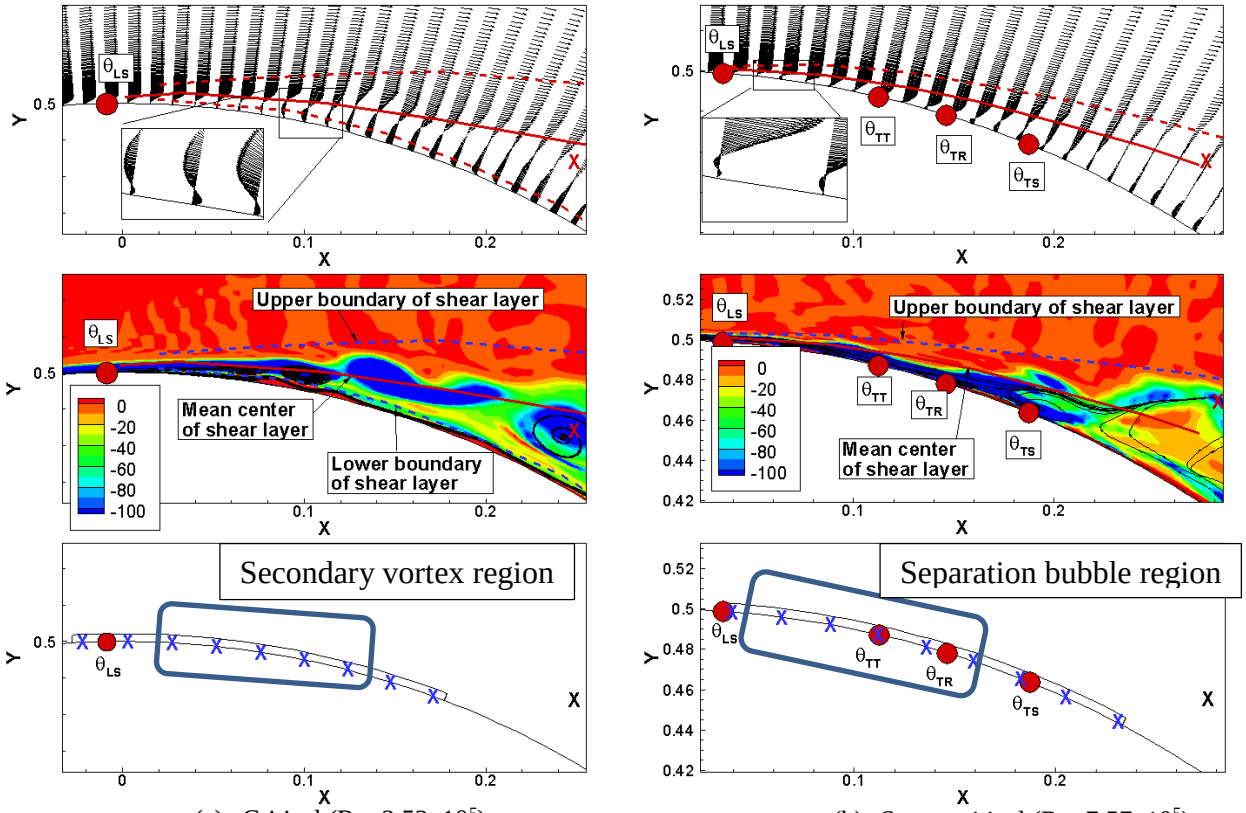

(a) Critical ($Re=2.52x10^5$) (b) Super-critical ($Re=7.57x10^5$)

Figure 5.5 Instantaneous velocity vector (top) and secondary vorticity with streamlines (middle) with the region for FFT analysis (bottom)

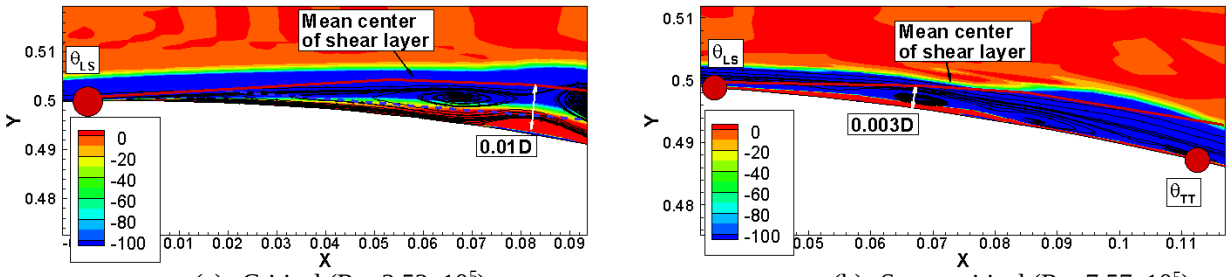

(a) Critical ($Re=2.52x10^5$) (b) Super-critical ($Re=7.57x10^5$)

Figure 5.6 Enlarged secondary vorticity with mean center of shear layer

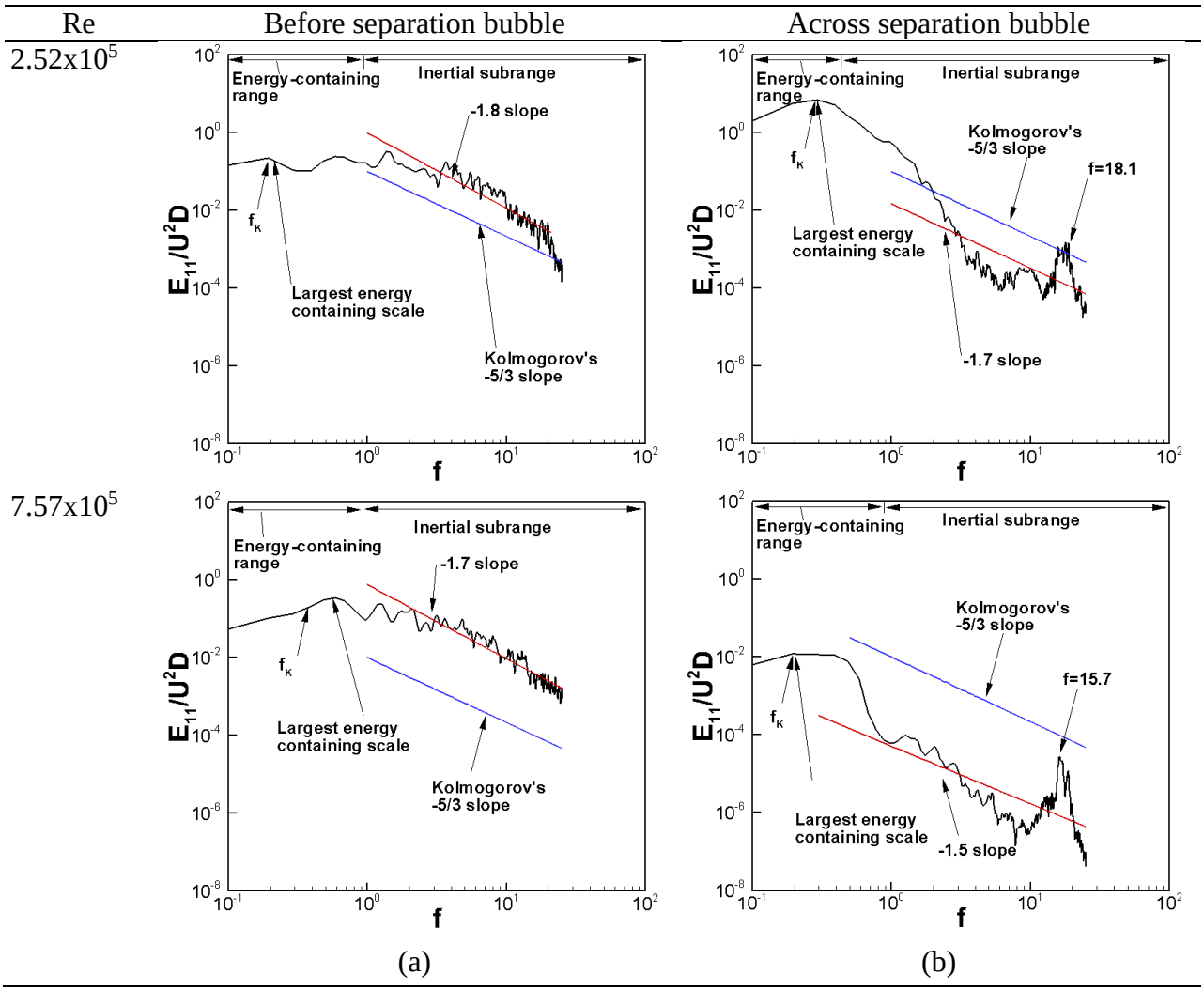

Figure 5.7 Energy spectra near separation bubble: (a) critical Re (Re=2.52x10^5) and (b) super-critical Re (7.57x10^5)

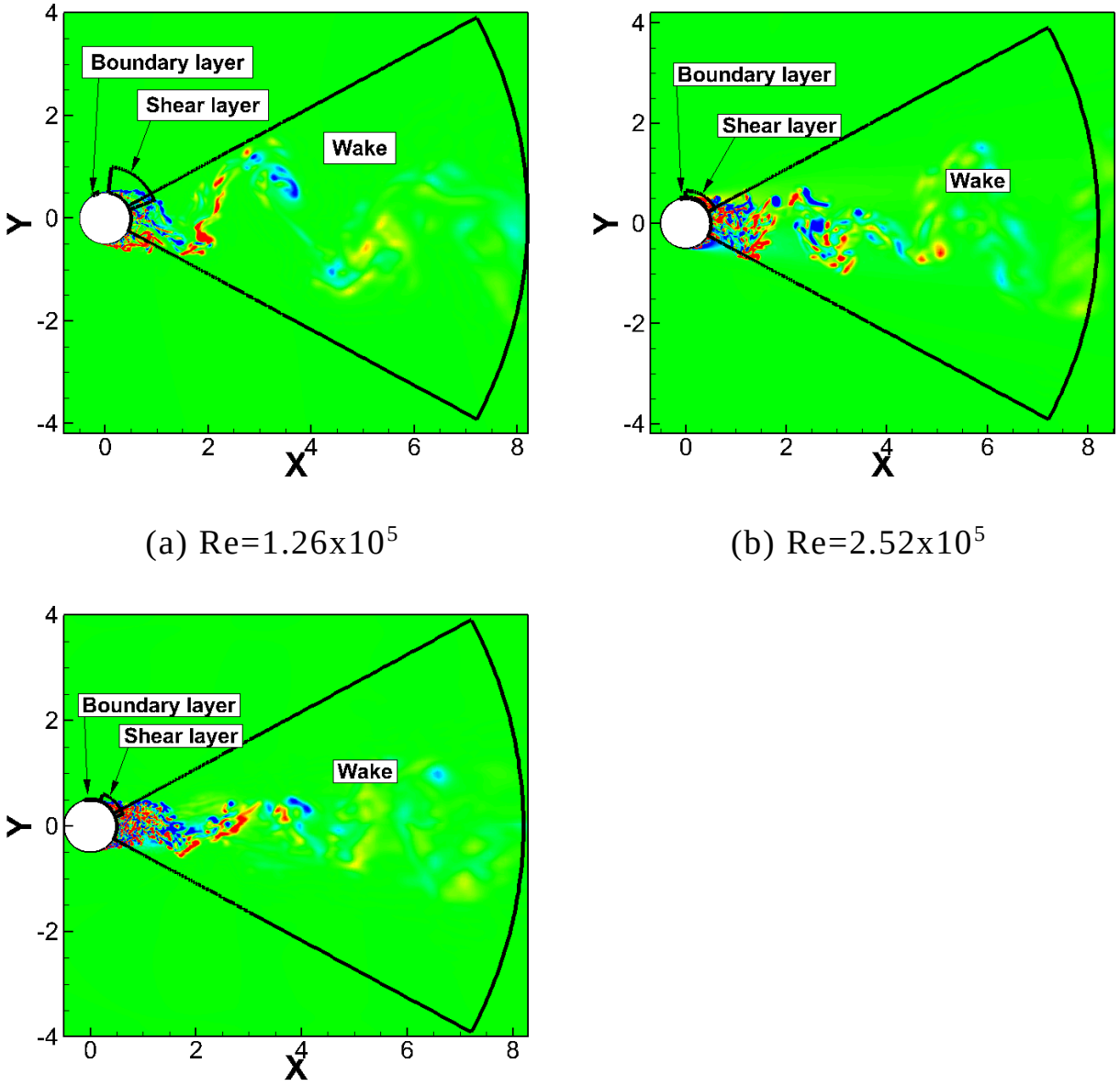

(a) Re=1.26x10^5

(b) Re=2.52x10^5

(c) Re=7.57x10^5

Figure 5.8 Analysis region of POD in flow field

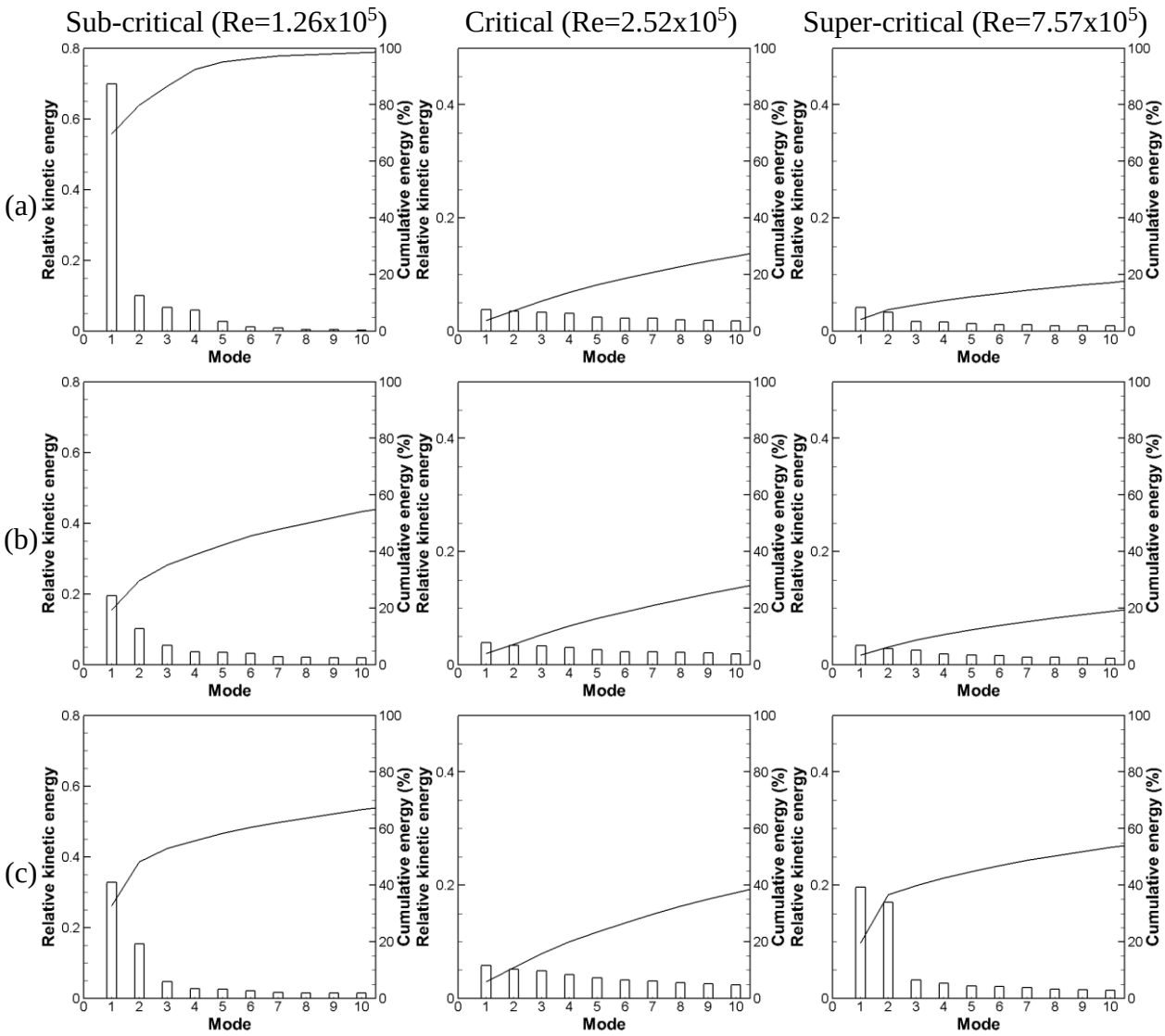

Figure 5.9 Relative kinetic energy distribution in POD regions up to first 10 modes: (a) boundary layer, (b) shear layer and (c) wake

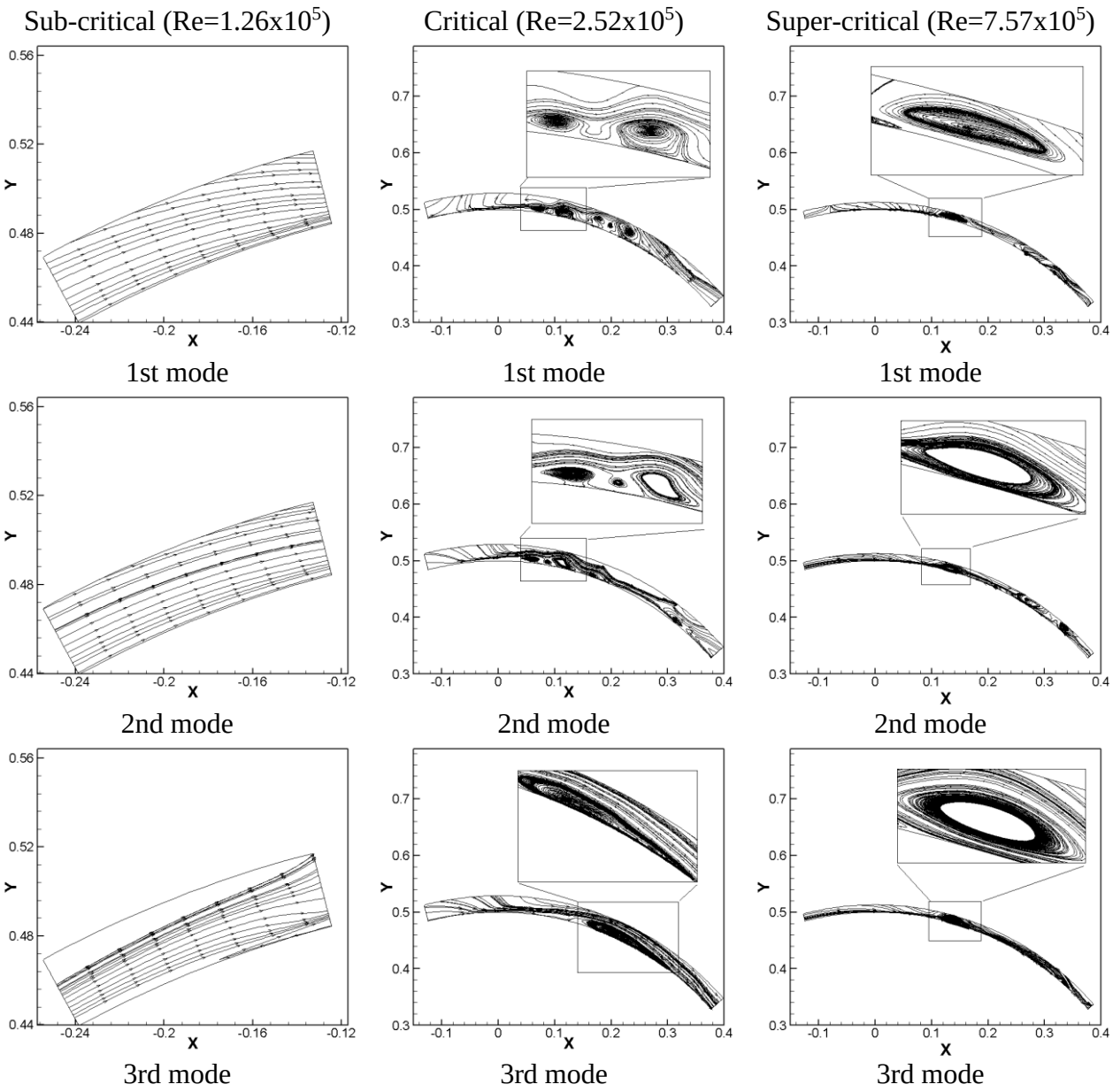

Figure 5.10 Streamlines in boundary layer at midspan

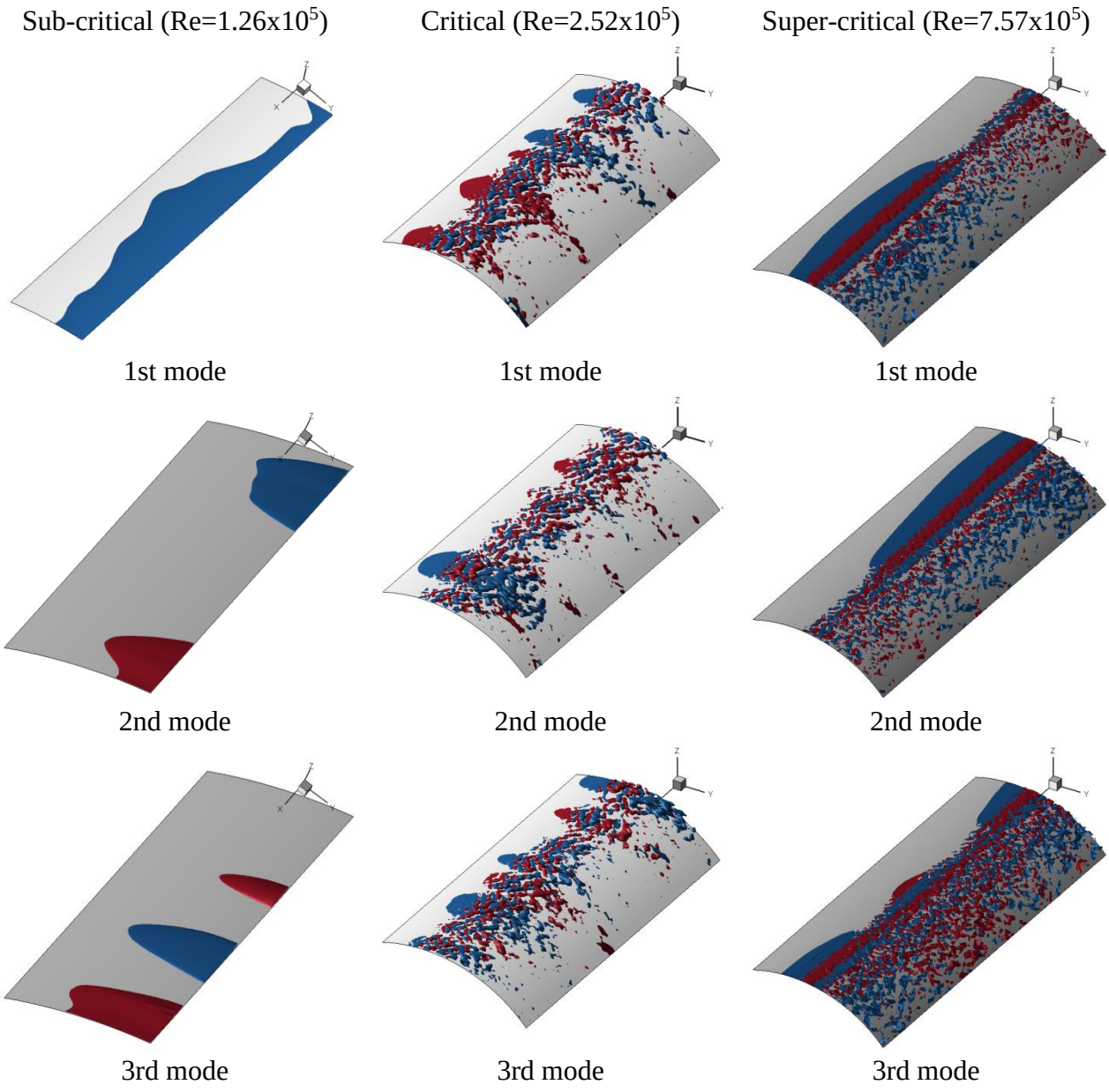

Figure 5.11 Spanwise vortex structure with Q-criterion in boundary layer

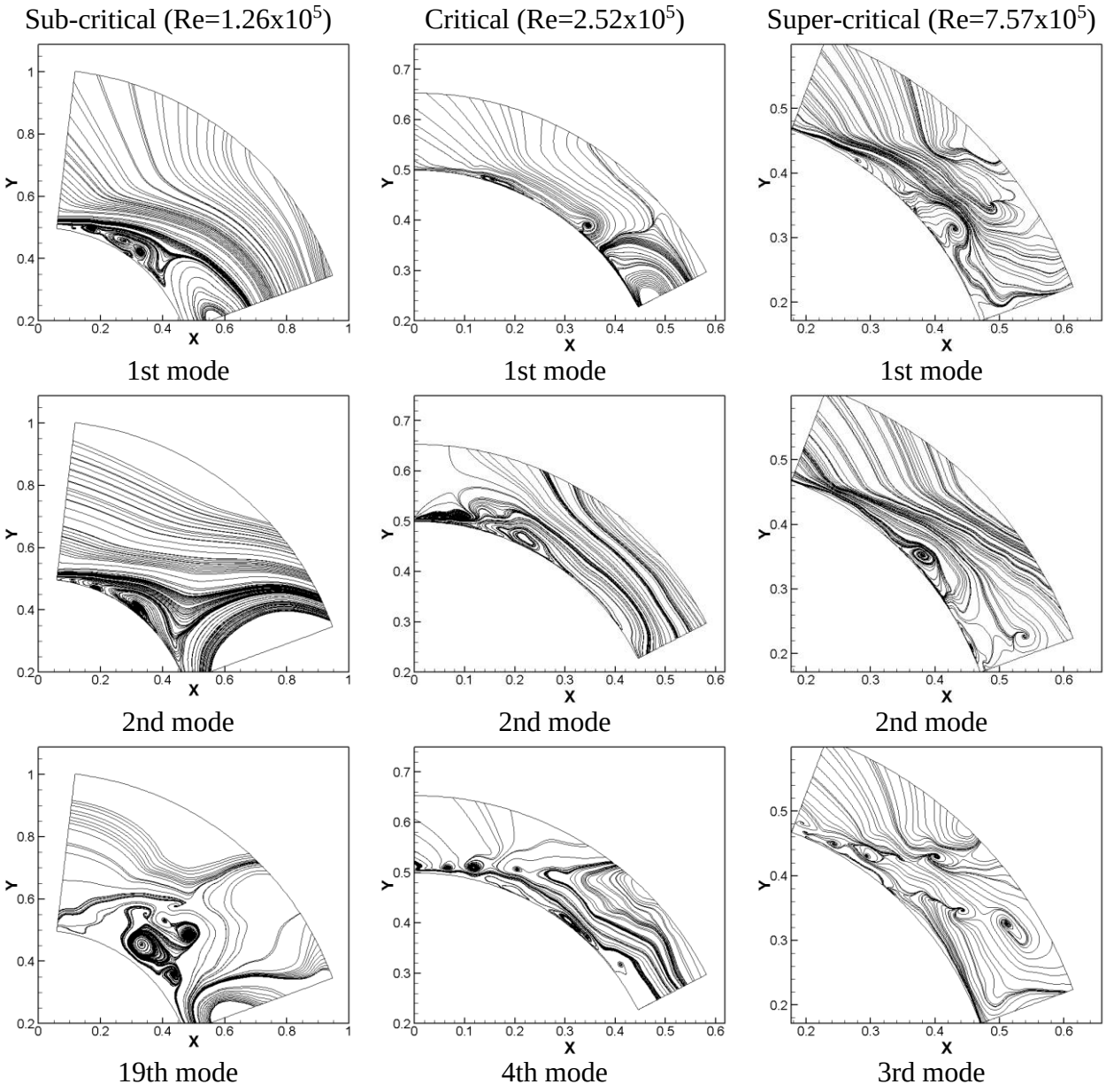

Figure 5.12 Streamlines in shear layer at midspan

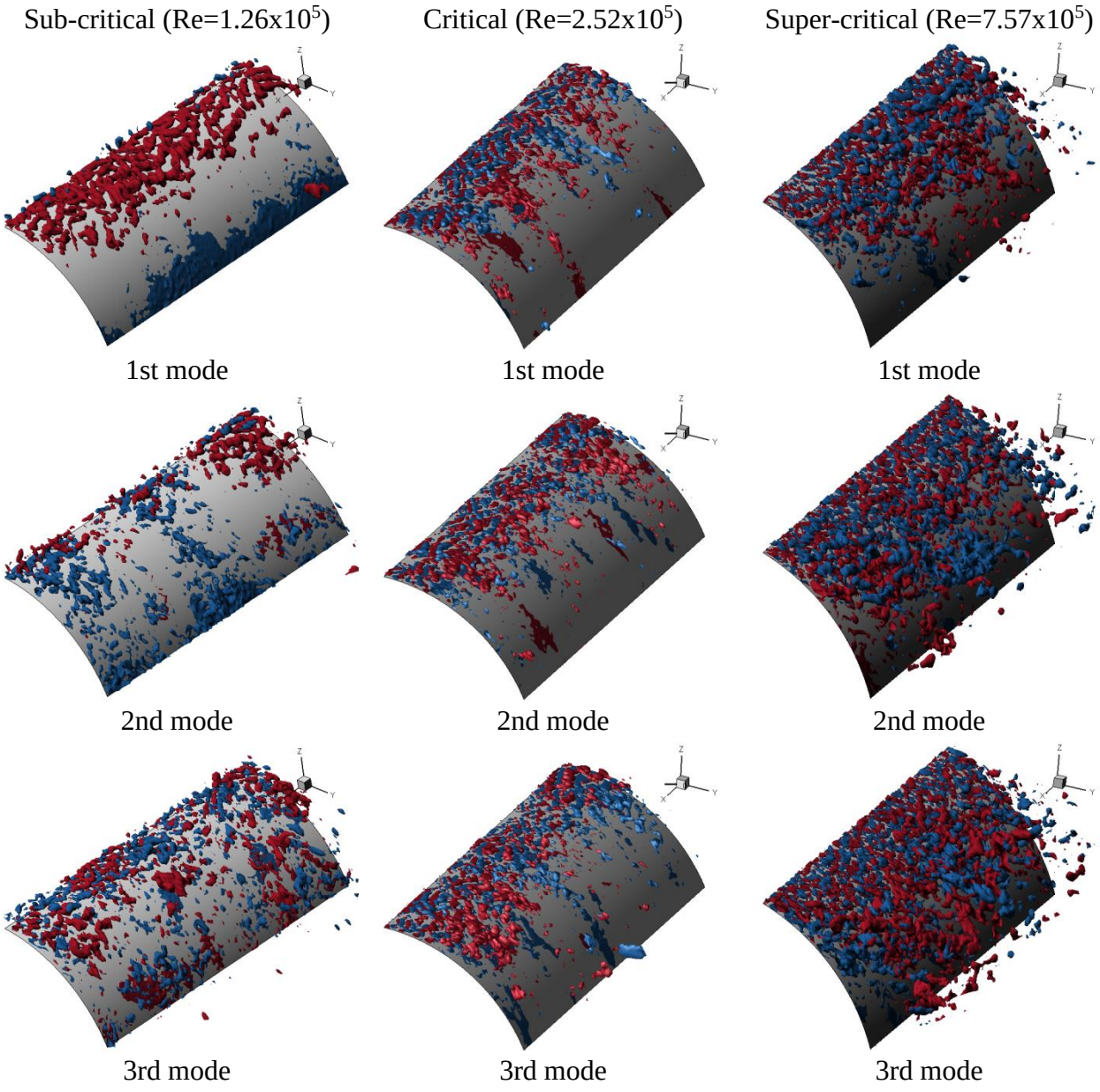

Figure 5.13 Spanwise vortex structure with Q-criterion in shear layer

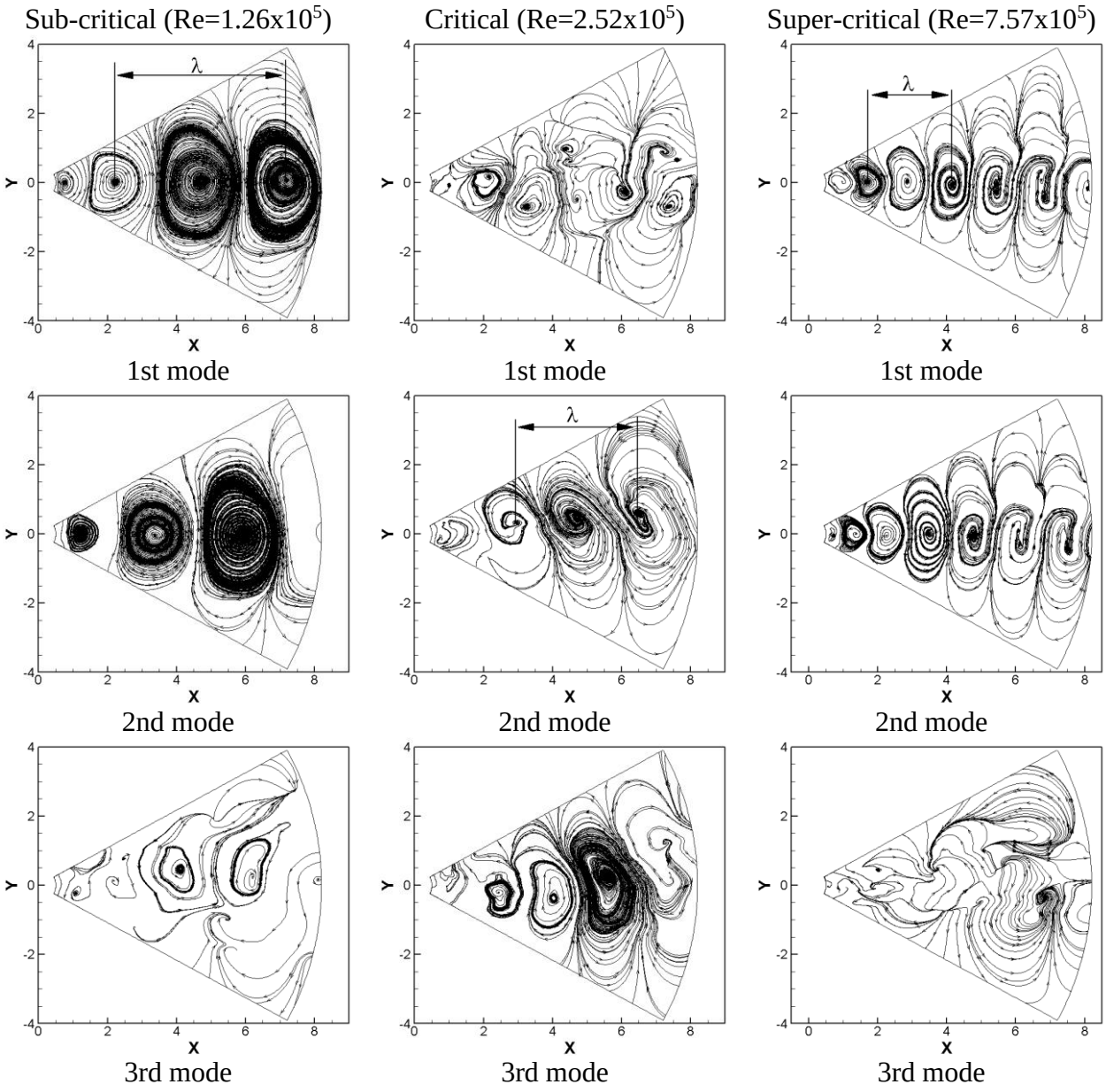

Figure 5.14 Streamlines in wake at midspan

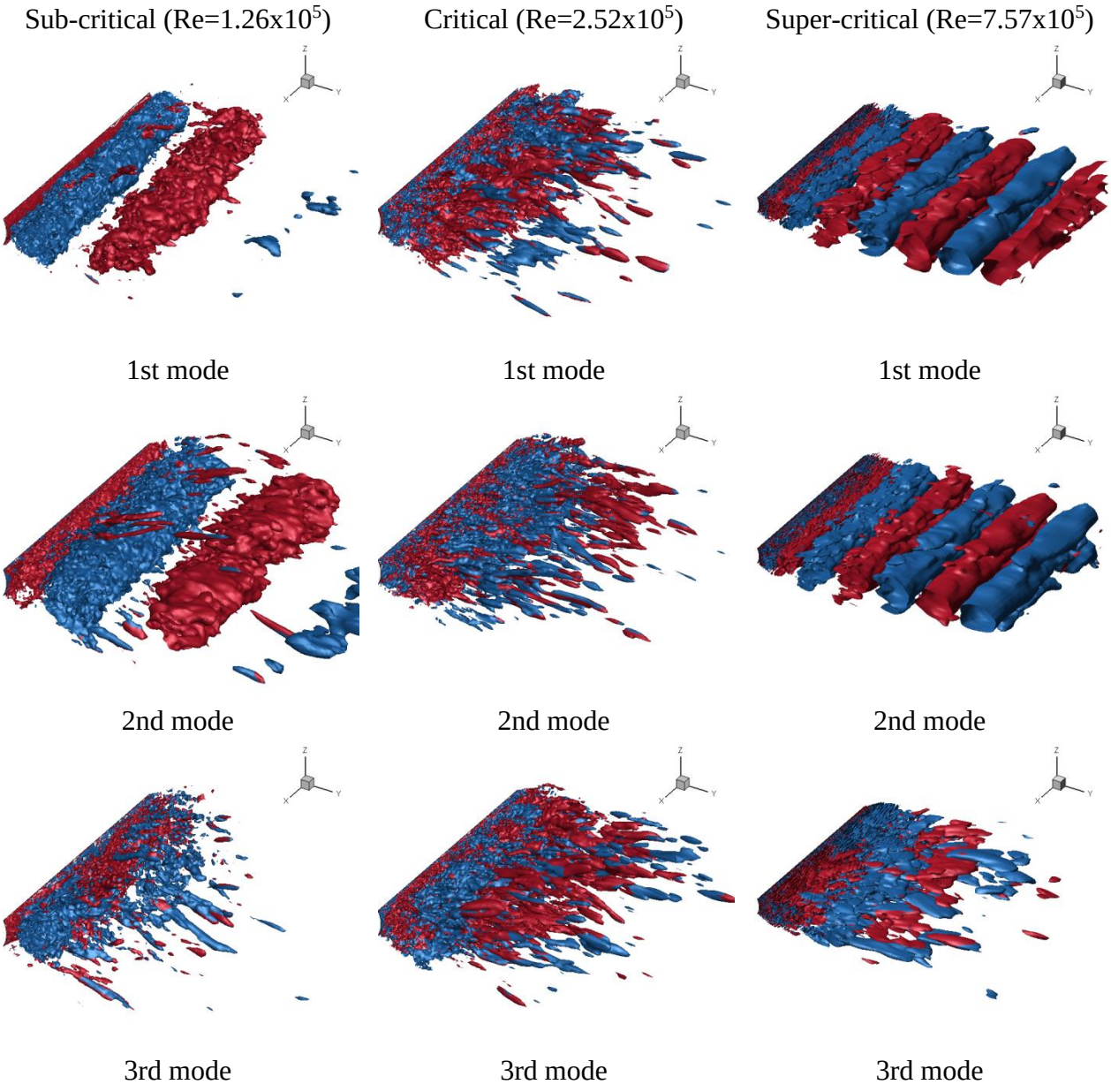

Figure 5.15 Spanwise vortex structure with Q-criterion in wake

CHAPTER 6 CONCLUSIONS AND FUTURE RESEARCH

The single-phase turbulent flows past a circular cylinder have been numerically investigated using the LES methodology in order to study flow structures at different flow regimes and resolve the issue in deep water solutions for the two-phase flow simulation by using CFDship-Iowa version 6.2, orthogonal curvilinear grid solver.

The quantitative verification and validation study has been carried out for $Re=7.57x10^5$. In verification study, large grid uncertainty for the drag and RMS of lift was found, which indicates finer grid is needed. The solutions were validated but with very large validation uncertainty due to large numerical grid uncertainty. A sensitivity study was conducted for aspect ratio, grid resolution and convection scheme. Definitely, large aspect ratio (AR=8) produced best results for the sub-critical Re. Small dependency on both aspect ratio and grid resolution was observed for the critical Re. Small aspect ratio (AR=2) and conservative scheme produced best results for the super-critical Re. However, the verification and validation study was not sufficient and systematic. Thus, more comprehensive and systematic studies are needed, especially for the sub-critical Re using large AR.

Validation study has been conducted in order to prove the validity of the numerical models. A single-grid estimator was used to assess the quality of the LES results and satisfied the minimum criteria all over the flow field. The resolved-scale TKE budgets required very long time scale (120 cycles) to be statistically stationary. In statistically stationary condition, relatively large imbalance was found around shear layer, which is likely due to numerical error and numerical dissipation. Nonetheless, qualitative TKE budget study was conducted in the shear layer and wake and obtained similar behavior to that of the backward-step flow. Flows were driven by pressure transport and convection before the laminar separation but pressure transport lost its contribution to the TKE after the separation. Across the separation bubble, the turbulent transport was providing energy to the transition region instead of removing the energy. Energy spectra validated the LES turbulence model but showed significant dissipation in higher

wavenumber range. In the wake, higher grid resolution was needed in order to resolve major energy carrying scales. Since there were limited data available in the literature for the validation of the LES study, especially for the critical and super-critical Re, a lot of experimental and numerical studies of flow past a circular cylinder were collected and used for the validation of the comprehensive but sparse LES study. Most of the data did not provide details of experimental setup including turbulence intensity and experimental uncertainty. Additionally, available data was mostly about integral variable and little for the local flow. For the sub-critical Re, the LES solutions showed fairly good agreement. For the critical Re, largest error was observed due to the sharp behavior of the variable including drag. For the super-critical Re, good agreement was made with local flow structures but some discrepancy including early prediction of turbulent separation was observed due to the grid uncertainty and numerical setup different from experimental setup. Since the validation data are outdated and sparse, new comprehensive experimental studies are needed, especially for local flow.

Further analysis has been conducted with the validated flow solutions. Basic flow features including mean velocity and vorticity showed the change of wake length due to the delayed separation with increasing Re. The main cause of the drag change was attributed to the mean pressure differences between the stagnation and base point. The Reynolds stresses and TKE distributions showed different distributions with flow regimes. For the sub- and super-critical Re, the distributions were similar but became narrow and lengthy as Re increased. For the critical Re, distribution was concentrated in the shear layer and no TKE distributions with strong intensity were found in the wake. It implies that there is some similarities between the sub- and super-critical Re. Instantaneous flow features including velocity, vorticity and three-dimensional flow structures showed large amplitude and anisotropic flow structures for the sub-critical Re and small amplitude and chaotic flow structures for the critical and super-critical Re. The wake region became narrow and chaotic even downstream for the super-critical Re so that large scale vortex shedding was not observed. The formation of secondary vortex and development into the separation bubble were observed with streamlines near the body and

secondary vorticity contour. Rough spectral analysis showed that the secondary vortex and separation bubble had instabilities close to the shear layer frequency. These results imply that the upstream movement of transition point of the shear layer and energetic mixing due to the proximity of the shear layer to the body induce reattachment and form the separation bubble. The flow structures in the boundary layer, shear layer and wake has been studied with the snapshot POD method. In the boundary layer, the shedding of the secondary vortex along the body was observed in several POD modes for the critical Re. A two-dimensional vortical structure representing the formation of the separation bubble was captured for the super-critical Re. Due to the weak TKE distribution in the shear layer, specific flow structures were not extracted and small-scale flow structures were observed in all the POD modes. Due to the strong TKE distribution in the wake, large two-dimensional flow structures were extracted for the sub- and super-critical Re and represented the Karman shedding vortices. No coherent flow structures were found for the critical Re, which was consistent with the absence of TKE structures in the wake.

For future work, a systematic sensitivity study, especially for the sub-critical Re will be conducted to support the present LES study. More comprehensive study up to post-critical Re will be performed, which should be conducted in conjunction with newly designed experimental studies to supplement the sparseness and lack of validation data. Based on the present LES study for the super-critical Re, further investigations will be performed to study the flow structures for the two-phase flow past a truncated surface-piercing circular cylinder and interaction with the interface.